Characterization of hybrid piezoelectric nanogenerators through asymptotic homogenization

Original
Characterization of hybrid piezoelectric nanogenerators through asymptotic homogenization / De Bellis, M.L., Bacigalupo, A., Zavarise, G.. - In: COMPUTER METHODS IN APPLIED MECHANICS AND ENGINEERING. - ISSN 0045-7825. - STAMPA. - 355:(2019), pp. 1148-1186. [10.1016/j.cma.2019.06.040]

Publisher:
Elsevier B.V.

Published
DOI:10.1016/j.cma.2019.06.040

Characterization of hybrid piezoelectric nanogenerators through asymptotic homogenization

Maria Laura De Bellis[1], Andrea Bacigalupo[2], Giorgio Zavarise[3]

[1] University of Chieti-Pescara, Department INGEO, Viale Pindaro 42, Pescara, Italy
[2] IMT School for Advanced Studies, Piazza S. Francesco 19, Lucca, Italy
[3] Polytechnic University of Turin, Department DISEG, Corso Duca degli Abruzzi 24, Torino, Italy

Abstract. In the framework of energy scavenging for applications in flexible/stretchable electronics, hybrid piezoelectric nanogenerators are investigated. They are made up with Zinc oxyde (ZnO) nanorods, embedded in a polymeric matrix, and grown on a flexible polymeric support. The ZnO nanorods are arranged in clusters, forming nearly regular distributions, so that periodic topologies can be realistically assumed. Focus is on a dynamic multi-field asymptotic homogenization approach, proposed to grasp the overall constitutive behaviour of such complex microstrutcures. A set of applications, both in static and dynamic regime, is proposed to explore different design paradigms, related to nanogenerators based on three working principles. Both extension and bending nanogenerators are, indeed, analysed, considering either extension along the nanorods axis, or orthogonally to it. The study of the wave propagation is, also, exploited to comprehend the main features of such piezoelectric devices in the dynamic regime.

Keywords: Energy scavenging, hybrid piezoelectric nanodevices, ZnO nanorods, periodic microstructure, multi-field homogenization, Bloch wave propagation.

1 Introduction

In the last decades energy harvesting is increasingly becoming a topic of great interest in different engineering fields. The key idea is that the energy, naturally available in the environment (for instance in the form of heat or kinetic energy) is captured and converted into electrical energy. This technology can be used to power small devices, such as wireless sensors and micro electronics, no longer requiring electrochemical batteries. Among others, piezoelectric generators, exploiting their intrinsic electro-mechanical coupling, are competitive solutions in energy harvesting, as witnessed by the growing number of applications, ranging from structural monitoring, to automotive industry, up to Internet of Things.
More recently particular attention has been drawn to emerging applications, such as biomedical monitoring, wearable technology, pervasive computing, micro and nano robotics, tire condition monitoring and extreme technology. To this aim, cutting-edge research has been devoted to design piezoelectric devices characterized by smaller and smaller size and high performances. Starting from the pioneering work by Wang and Song (2006), piezoelectric nanogenerators have been successfully proposed, based on different electro-active materials and working principles (Wang et al., 2008; Briscoe and Dunn, 2015; McCarthy et al., 2016; Jin et al., 2016; Zhang et al., 2016; Ahmed et al., 2017; Li et al., 2017a,b; Saadatnia et al.,

2017; Wang et al., 2017a; Liu et al., 2018; Askari et al., 2019). Relevant examples concern either the use of piezoelectric zinc oxide (ZnO) nanowire arrays grown on conductive rigid supports (Yi et al., 2005; Wang and Song, 2006), or the adoption of lead zirconate titanate (PZT), polyvinylidene fluoride (PVDF) and barium titanate (BT).

An important improvement in the design of ZnO nanorods-based piezoelectric generators has been achieved by adopting flexible substrates made of electro-active polymeric materials. The main advantage is, indeed, the possibility of exploiting relevant flexural mechanisms, besides the standard direct compression of the device. In Fan et al. (2016) different typologies of flexible nanogenerators are presented and critically commented. Also patterned growth of ZnO nanowires can be exploited to enhance the performances of flexible nanogenerators, as discussed in Yang et al. (2017).

Further benefits can be obtained by resorting to so-called hybrid nanogenerators, made up by embedding the ZnO nanorods within a polymeric matrix. More specifically, Stassi et al. (2015) propose highly oriented ZnO nanotubes in a porous polycarbonate (PC) matrix. The result is an efficient nanogenerator based on such a highly flexible ZnOPC composite. Moreover, in Choi et al. (2017) a hybrid piezoelectric structure made of ZnO nanowires and a matrix of PVDF polymer is investigated, in order to obtain a power enhancement. The authors, indeed, find that the ZnO nanowires are able to deliver internal strain to the PVDF, which increase the electrical power output of the hybrid nanogenerator.

Based on the aforementioned considerations, with the aim of energy harvesting from green and sustainable energy resources, our focus is on hybrid flexible nanogenerators, made up with clusters of ZnO nanorods embedded into a polymeric matrix and growth on a flexible support. The choice of ZnO nanorods, is motivated by their relatively simple forming processes using low temperature. In particular, by exploiting innovative growth techniques, it is possible to synthesize ZnO nanorods clamped on top of a flexible support, which is typically realized by sandwiching a polymer base and a layer of conductive fluorine-doped tin oxide (FTO). Concerning the zinc oxyde, the most stable crystalline structure is the Wurtzite (Wz), characterized by an hexagonal structure and a stacking sequence such that the nanorod axis coincides with the [0001] crystalline direction (see Wang (2004) for details). It follows that the resulting nanorods have hexagonal cross section and principal axis nearly orthogonal to the base support. The overall material is, thus, characterized by a pronounced uni-axial anisotropy and the spontaneous polarization direction coincides with the axis of the nanorods. The ZnO nanorods, having roughly constant section sizes and heights, arrange themselves in clusters characterized in general by nearly regular distributions. It is important to emphasize that, during the synthesis process of such material it is possible to tune both the density and the heights of the nanorods. The electro-active polymeric matrix is subsequently added, filling the gaps between the nanorods. Moreover, different clusters can be stacked together along the nanorods axis direction, in order to enhance their piezoelectric performances. The device is complemented by the presence of two electrodes located at the opposite external top and bottom faces. Due to the nearly regular distribution of the nanorods, for the sake of simplicity, it is possible to consider periodic topologies, in which the nanorods are equally spaced. The resulting material is a microstructured piezoelectric composite, whose global response is strongly influenced by its microstructure, i.e. by the geometry and materials properties of each constituents and by their collaborative behaviour.

With a view to investigating such kind of materials, a possibility is resorting to micromechanical approaches, in which the material is described in detail, but generally they result in cumbersome analyses. In order to overcome these drawbacks, multiscale techniques, based on homogenization approaches, constitute a very valuable tool to gather both a synthetic and thorough description of the complex material behaviour. The investigation of the overall static and dynamic behaviour of periodic elastic composite materials has been performed resorting either to asymptotic approaches (Bakhvalov and Panasenko, 1984; Gambin and Kröner, 1989; Allaire, 1992; Boutin, 1996; Fish and Chen, 2001; Andrianov et al., 2008; Bacigalupo, 2014), or to variational-asymptotic approaches (Smyshlyaev and Cherednichenko, 2000; Peerlings and Fleck, 2004; Bacigalupo and Gambarotta, 2012, 2014; Cherednichenko and Evans, 2019; Kamotski and Smyshlyaev, 2019), or also to identification techniques. Among them we cite the computational approaches (Kouznetsova et al., 2004; Scarpa et al., 2009; Bacigalupo and Gambarotta, 2010; Scarpa et al., 2010; De Bellis and Addessi, 2011; Li et al., 2011; Addessi et al., 2013; Chen et al., 2013; Dirrenberger et al., 2013; Lesičar et al., 2014; Trovalusci et al., 2015; Addessi et al., 2016; Sepe et al., 2016; Biswas and Poh, 2017; Wang et al., 2017b; Reccia et al., 2018; Trovalusci et al., 2017; Bansal et al., 2019; Biswas et al., 2019; Zhang et al., 2019) and the analytical approaches of (Bigoni and Drugan, 2007; Cecchi and Tralli, 2012; Mühlich et al., 2012; Bacca et al., 2013a,b; Bacigalupo and Gambarotta, 2013; Baraldi et al., 2015; Bacigalupo et al., 2017; Hütter, 2017).

Generalized homogenization approaches have been proposed to date, to handle multi-field problems, ranging from thermo-elastic and thermo-diffusive, to piezoelectric and thermo-piezoelectric problems (Gałka et al., 1996; Pettermann and Suresh, 2000; Aboudi et al., 2001; Berger et al., 2005; Kanouté et al., 2009; Zhang et al., 2007; Deraemaeker and Nasser, 2010; Zah and Miehe, 2013; Salvadori et al., 2014; Bacigalupo et al., 2016; Fantoni et al., 2017; De Bellis and Bacigalupo, 2017; Fantoni et al., 2018).

In this context, we propose a dynamic multi-field asymptotic homogenization approach for the analysis of hybrid piezoelectric nanogenerators with periodic microstructure. The key point of such approach is that the microscopic displacement and the electric potential fields are asymptotically expanded and plugged into the microscopic governing equations. It follows that a series of recursive differential problems are defined, in terms of the sensitivities of the microscopic fields. Such problems give rise to down-scaling relations, hierarchical cell problems, in terms of perturbation functions, and so-called average field equations of infinite order. The overall constitutive tensors and the overall inertial terms are, thus, rigorously derived from the generalized macro-homogeneity condition, properly relating the macroscopic Lagrangian and the microscopic mean Lagrangian, referred to a representative portion of the material either at the macroscopic or at the microscopic scale. By truncating the asymptotic expansion of the microscopic mean Lagrangian at different orders, either first order or higher order equivalent homogeneous continua can be identified. As an alternative, first and higher order approximations can be also obtained by solving, via perturbative approaches, the average field equations of infinite order.

The dispersive wave propagation in the hybrid piezoelectric nanogenerators has been, then, investigated and the frequency band structure has been determined consistently with the Floquet-Bloch theory (Floquet, 1883; Bloch, 1928). Moreover, the dispersion functions in equivalent homogeneous materials are derived, able to accurately approximate the acoustic branches of the Floquet-Bloch spectrum in the long wavelength regime.

Applications has been devoted both to the static and dynamic analysis of periodic hybrid piezoelectric nanogenerators. In the framework of a first order homogenization approach, the equivalent constitutive properties are determined as a function of the heights and the density of the nanorods. This can be done since such geometric parameters can be easily controlled, in the synthesis of the material, in order to tune the overall piezoelectric response. Considering a benchmark test of an extensional microstrutcured nanogenerator, the reliability of the proposed homogenization model has been proved by comparing the analytical homogenized solutions with the corresponding solutions of the heterogeneous model.

In addition, three piezoelectric microstructured nanogenerators, based on different working principles, are investigated as a set of geometrical parameters changes. More specifically, microstructured extension nanogenerators, bending nanogenerators and transversal extension nanogenerators are taken into account and their static behaviour is critically discussed, in order to provide broad guidelines to maximize their efficiency.

Finally, a dynamic characterization of the piezoelectric periodic nanostructured material is performed for the purpose of analysing Bloch waves propagations. Focus is on detecting possible partial or total band gaps, strongly characterizing the dynamic response of the composite material. A good agreement has been found between the dispersion functions analytically obtained by the homogenized model, and the acoustic branches of the Floquet-Bloch spectrum of the heterogeneous material.

2 Piezoelectric material modelled at two-scales

Let us consider a heterogeneous piezoelectric material, with periodic microstructure, which phases are described as a first order continuum in the framework of the linear theory of piezoelectricity. Each material point is identified by its position vector $\mathbf{x} = x_1\mathbf{e}_1 + x_2\mathbf{e}_2 + x_3\mathbf{e}_3$, referred to a coordinate system with origin at point O and orthogonal base with the fixed set of basis vectors $\mathbf{e}_1, \mathbf{e}_2, \mathbf{e}_3$, see Figure 1. Under the action of external sources, i.e. body forces $\mathbf{b}(\mathbf{x}, t) = b_i(\mathbf{x}, t)\mathbf{e}_i$ and free charge densities $\rho_e(\mathbf{x}, t)$, the microscopic displacement field $\mathbf{u}(\mathbf{x}, t) = u_i(\mathbf{x}, t)\mathbf{e}_i$ and the microscopic electric potential field $\phi(\mathbf{x}, t)$ are induced. The fields depends both on point $\mathbf{x}$ and on time t.

By exploiting the periodicity of the medium, a Periodic Cell $\mathfrak{A} = [-d/2, d/2]\times[-d/2, d/2]\times[-h/2, h/2]$ is identified. It is denoted by the three orthogonal periodicity vectors $\mathbf{v}_1 = d\mathbf{e}_1 = \varepsilon\mathbf{e}_1$, $\mathbf{v}_2 = d\mathbf{e}_2 = \varepsilon\mathbf{e}_2$ and

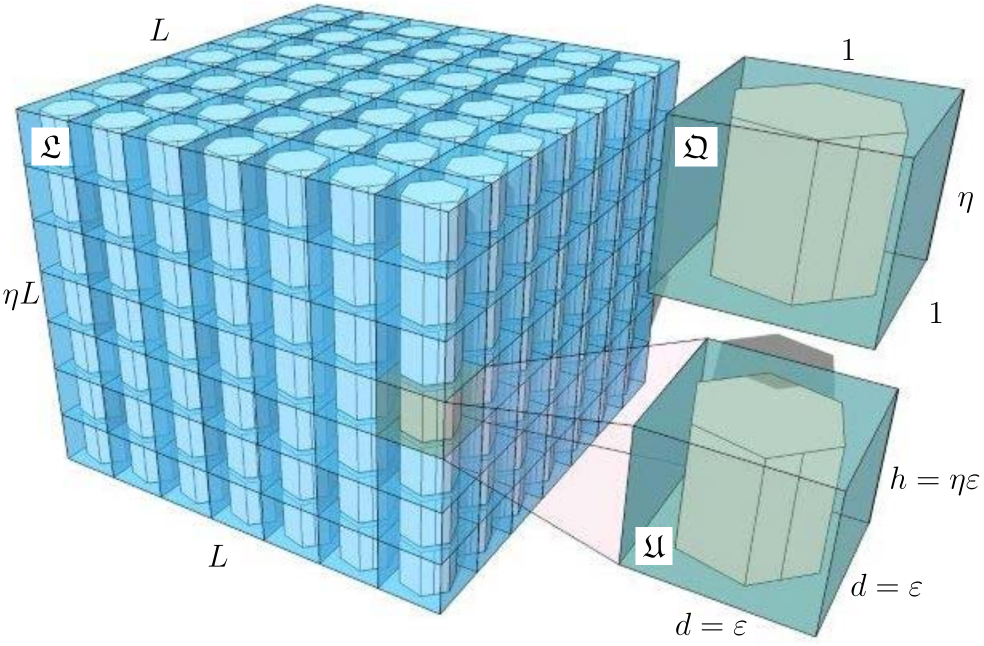

Fig. 1: Representative portion of the heterogeneous material: $\mathfrak{L}$ Cluster of Periodic Cells, $\mathfrak{A}$ Periodic Cell, and $\mathfrak{Q}$ Unit Cell.

$\mathbf{v}_3 = h\mathbf{e}_3 = \eta\varepsilon\mathbf{e}_3$, being ε the characteristic size of the cell $\mathfrak{A}$, see Fig. 1(b). Consistently with standard asymptotic homogenization approaches, the Unit Cell $\mathfrak{Q} = [-1/2, 1/2] \times [-1/2, 1/2] \times [-\eta/2, \eta/2]$ is obtained by applying the rescaling factor of ε to the Periodic Cell $\mathfrak{A}$. In agreement with (Mindlin, 1974), the partial differential equations governing the piezoelectric problem, in component form, are

$$
\begin{aligned}
&\frac{D}{Dx_j}\left(C_{ijkl}^{(m,\varepsilon)}\frac{Du_k}{Dx_l}\right) + \frac{D}{Dx_j}\left(e_{ijk}^{(m,\varepsilon)}\frac{D\phi}{Dx_k}\right) + b_i = \rho^{(m,\varepsilon)}\frac{D^2u_i}{Dt^2},\\
&\frac{D}{Dx_i}\left(\widetilde{e}_{ikl}^{(m,\varepsilon)}\frac{Du_k}{Dx_l}\right) - \frac{D}{Dx_i}\left(\beta_{il}^{(m,\varepsilon)}\frac{D\phi}{Dx_l}\right) = \rho_e,
\end{aligned}
\tag{1}
$$

where $C_{ijkl}^{(m,\varepsilon)}$ are the components of the fourth order micro elasticity tensor, $e_{ijk}^{(m,\varepsilon)}$ are the components of the third order piezoelectric stress-charge coupling tensor, $\beta_{il}^{(m,\varepsilon)}$ are the components of the second order dielectric permittivity tensor, and $\rho^{(m,\varepsilon)}$ is the mass density. Moreover, the following relation holds between the components $\widetilde{e}_{ijk}^{(m,\varepsilon)} = e_{jki}^{(m,\varepsilon)}$. In Equations (1) the superscripts m and ε refer to microscopic fields, and to the characteristic size of the Periodic Cell, respectively. Note that generalized derivatives are taken into account.

The constitutive tensors and the mass density are characterized by $\mathfrak{A}$-periodicity, i.e.

$$
\begin{aligned}
C_{ijkl}^{(m,\varepsilon)}\left(\mathbf{x} + \mathbf{v}_\alpha\right) &= C_{ijkl}^{(m,\varepsilon)}\left(\mathbf{x}\right),\\
e_{ijk}^{(m,\varepsilon)}\left(\mathbf{x} + \mathbf{v}_\alpha\right) &= e_{ijk}^{(m,\varepsilon)}\left(\mathbf{x}\right),
\end{aligned}
$$

$$\begin{aligned}
&\beta_{il}^{(m,\varepsilon)}\left(\mathbf{x}+\mathbf{v}_\alpha\right)=\beta_{il}^{(m,\varepsilon)}\left(\mathbf{x}\right),\\
&\rho^{(m,\varepsilon)}\left(\mathbf{x}+\mathbf{v}_\alpha\right)=\rho^{(m,\varepsilon)}\left(\mathbf{x}\right),\quad \alpha=1,2,3,\quad \forall\mathbf{x}\in\mathfrak{A},
\end{aligned}\tag{2}$$

therefore, they only depend on the variable $\boldsymbol{\xi}=\mathbf{x}/\varepsilon$, so that the Q-periodicity holds, as

$$\begin{aligned}
&C_{ijkl}^{(m,\varepsilon)}\left(\mathbf{x}\right)=C_{ijkl}^{(m,\varepsilon)}\left(\boldsymbol{\xi}=\frac{\mathbf{x}}{\varepsilon}\right),\\
&e_{ijk}^{(m,\varepsilon)}\left(\mathbf{x}\right)=e_{ijk}^{(m,\varepsilon)}\left(\boldsymbol{\xi}=\frac{\mathbf{x}}{\varepsilon}\right),\\
&\beta_{il}^{(m,\varepsilon)}\left(\mathbf{x}\right)=\beta_{il}^{(m,\varepsilon)}\left(\boldsymbol{\xi}=\frac{\mathbf{x}}{\varepsilon}\right),\\
&\rho^{(m,\varepsilon)}\left(\mathbf{x}\right)=\rho^{(m,\varepsilon)}\left(\boldsymbol{\xi}=\frac{\mathbf{x}}{\varepsilon}\right),\quad \forall\boldsymbol{\xi}\in\mathfrak{Q}.
\end{aligned}\tag{3}$$

It is assumed that the body forces are $\mathfrak{L}$-periodic with period $\mathfrak{L}=[-L/2,L/2]\times[-L/2,L/2]\times[-\eta L/2,\eta L/2]$, and have zero mean values on $\mathfrak{L}$. Moreover, $\mathfrak{L}$ can be considered as a representative portion of the whole body, under the assumption that the structural length L is much greater than the microstructural size ε ($L>>\varepsilon$), consistently with the scale separation principle. As a consequence, the microscopic fields can be expressed in the form $u_i\left(\mathbf{x},\boldsymbol{\xi}=\mathbf{x}/\varepsilon,t\right)$ and $\phi\left(\mathbf{x},\boldsymbol{\xi}=\mathbf{x}/\varepsilon,t\right)$, where $\mathbf{x}$ and $\boldsymbol{\xi}=\mathbf{x}/\varepsilon$ play the roles of macroscopic variable ($slow$ variable), and microscopic variable ($fast$ variable), respectively.

Due to this double $\mathfrak{Q}$- and $\mathfrak{L}$-periodicity, finding the solution of partial differential equations (1) is, in general, very burdensome adopting numerical approaches and very difficult via analytic approaches. This implies that valuable alternative approaches have to be found. In particular, homogenization techniques, allowing to replace the periodic medium with an equivalent homogeneous one, provide an efficient tool to accurately describe the overall behaviour of the microstructured piezoelectric material, with low computational costs. We here derive a macroscopic equivalent piezoeletric continuum, which overall constitutive tensors are analytically obtained in terms of the actual geometric and physical properties of the microsctructure. In particular, at the macroscopic scale the variables $\mathbf{U}\left(\mathbf{x},t\right)=U_i\left(\mathbf{x},t\right)\mathbf{e}_i$ and $\varPhi\left(\mathbf{x},t\right)$ are consistently defined, depending both on the macroscopic point $\mathbf{x}$ and on time t.

3 Asymptotic expansion of microscopic field equations

The microscopic fields, involved in the governing equations, can be expressed through an asymptotic expansion in terms of the microscopic characteristic size ε, (Bakhvalov and Panasenko, 1984) . Consistently with the principle of scale separation, the $slow$ and $fast$ variables are kept separate, and the following expressions hold

$$\begin{aligned}
u_k\left(\mathbf{x},\frac{\mathbf{x}}{\varepsilon},t\right) &= \sum_{l=0}^{+\infty}\varepsilon^l u_k^{(l)}\left(\mathbf{x},\frac{\mathbf{x}}{\varepsilon},t\right) = u_k^{(0)}\left(\mathbf{x},\frac{\mathbf{x}}{\varepsilon},t\right) + \varepsilon u_k^{(1)}\left(\mathbf{x},\frac{\mathbf{x}}{\varepsilon},t\right) + \varepsilon^2 u_k^{(2)}\left(\mathbf{x},\frac{\mathbf{x}}{\varepsilon},t\right) + \mathcal{O}\left(\varepsilon^{\mathbf{3}}\right),\\
\phi\left(\mathbf{x},\frac{\mathbf{x}}{\varepsilon},t\right) &= \sum_{l=0}^{+\infty}\varepsilon^l \phi^{(l)}\left(\mathbf{x},\frac{\mathbf{x}}{\varepsilon},t\right) = \phi^{(0)}\left(\mathbf{x},\frac{\mathbf{x}}{\varepsilon},t\right) + \varepsilon \phi^{(1)}\left(\mathbf{x},\frac{\mathbf{x}}{\varepsilon},t\right) + \varepsilon^2 \phi^{(2)}\left(\mathbf{x},\frac{\mathbf{x}}{\varepsilon},t\right) + \mathcal{O}\left(\varepsilon^{\mathbf{3}}\right).
\end{aligned} \tag{4}$$

Moreover, recalling the derivation rule valid for the function $f\left(\mathbf{x},\boldsymbol{\xi}=\frac{\mathbf{x}}{\varepsilon}\right)$, that is

$$\frac{D}{Dx_j}f\left(\mathbf{x},\boldsymbol{\xi}=\frac{\mathbf{x}}{\varepsilon}\right) = \left.\left(\frac{\partial f}{\partial x_j}+\frac{1}{\varepsilon}\frac{\partial f}{\partial \xi_j}\right)\right|_{\boldsymbol{\xi}=\frac{\mathbf{x}}{\varepsilon}} = \left.\left(\frac{\partial f}{\partial x_j}+\frac{1}{\varepsilon}f_{,j}\right)\right|_{\boldsymbol{\xi}=\frac{\mathbf{x}}{\varepsilon}}, \tag{5}$$

and plugging the asymptotic expansions (4), into the governing equations (1), the asymptotic expansion of miscroscopic field equations is obtained as

$$\begin{aligned}
&\Bigg\{\varepsilon^{-2}\left(\left(C^m_{ijkl}u^{(0)}_{k,l}\right)_{,j}+\left(e^m_{ijk}\phi^{(0)}_{,k}\right)_{,j}\right)+\varepsilon^{-1}\Bigg[\left(C^m_{ijkl}\left(\frac{\partial u^{(0)}_k}{\partial x_l}+u^{(1)}_{k,l}\right)\right)_{,j}+\frac{\partial}{\partial x_j}\left(C^m_{ijkl}u^{(0)}_{k,l}\right)+\\
&+\left(e^m_{ijk}\left(\frac{\partial \phi^{(0)}}{\partial x_l}+\phi^{(1)}_{,k}\right)\right)_{,j}+\frac{\partial}{\partial x_j}\left(e^m_{ijk}\phi^{(0)}_{,k}\right)\Bigg]+\Bigg[\left(C^m_{ijkl}\left(\frac{\partial u^{(1)}_k}{\partial x_l}+u^{(2)}_{k,l}\right)\right)_{,j}+\\
&+\frac{\partial}{\partial x_j}\left(C^m_{ijkl}\left(\frac{\partial u^{(0)}_k}{\partial x_l}+u^{(1)}_{k,l}\right)\right)+\left(e^m_{ijk}\left(\frac{\partial \phi^{(1)}}{\partial x_l}+\phi^{(2)}_{,k}\right)\right)_{,j}+\frac{\partial}{\partial x_j}\left(e^m_{ijk}\left(\frac{\partial \phi^{(0)}}{\partial x_l}+\phi^{(1)}_{,k}\right)\right)+\\
&-\rho^m\ddot{u}^{(0)}_i+\mathcal{O}\left(\varepsilon\right)\Bigg]\Bigg\}\Bigg|_{\boldsymbol{\xi}=\frac{\mathbf{x}}{\varepsilon}}+b_i=0,\\
&\Bigg\{\varepsilon^{-2}\left(\left(e^m_{kli}u^{(0)}_{k,l}\right)_{,i}-\left(\beta^m_{il}\phi^{(0)}_{,l}\right)_{,i}\right)+\varepsilon^{-1}\Bigg[\left(e^m_{kli}\left(\frac{\partial u^{(0)}_k}{\partial x_l}+u^{(1)}_{k,l}\right)\right)_{,i}+\frac{\partial}{\partial x_i}\left(e^m_{kli}u^{(0)}_{k,l}\right)+\\
&-\left(\beta^m_{il}\left(\frac{\partial \phi^{(0)}}{\partial x_l}+\phi^{(1)}_{,l}\right)\right)_{,i}-\frac{\partial}{\partial x_i}\left(\beta^m_{il}\phi^{(0)}_{,l}\right)\Bigg]+\Bigg[\left(e^m_{kli}\left(\frac{\partial u^{(1)}_k}{\partial x_l}+u^{(2)}_{k,l}\right)\right)_{,i}+\\
&+\frac{\partial}{\partial x_i}\left(e^m_{kli}\left(\frac{\partial u^{(0)}_k}{\partial x_l}+u^{(1)}_{k,l}\right)\right)-\left(\beta^m_{il}\left(\frac{\partial \phi^{(1)}}{\partial x_l}+\phi^{(2)}_{,l}\right)\right)_{,i}-\frac{\partial}{\partial x_i}\left(\beta^m_{il}\left(\frac{\partial \phi^{(0)}}{\partial x_l}+\phi^{(1)}_{,l}\right)\right)+\\
&+\mathcal{O}\left(\varepsilon\right)]\}|_{\boldsymbol{\xi}=\frac{\mathbf{x}}{\varepsilon}}-\rho_e=0.
\end{aligned} \tag{6}$$

After proper manipulations, by collecting the terms with equal power ε, a hierarchical set of recursive partial differential problems, in terms of the sensitivities $u_k^{(j)}$ and $\phi^{(j)}$, is obtained. The statement and the solution of such recursive problems are reported in Appendix A. In particular, the solution of the

ε^{-2}-order problem, in (43), takes the following form, where the dependence on the microscopic variable disappears

$$\begin{aligned} u_k^{(0)}\left(\mathbf{x},\boldsymbol{\xi},t\right) &= U_k\left(\mathbf{x},t\right), \\ \phi^{(0)}\left(\mathbf{x},\boldsymbol{\xi},t\right) &= \Phi\left(\mathbf{x},t\right). \end{aligned} \tag{7}$$

Analogously, the solution of the ε^{-1}-order problem, in (44), results in

$$\begin{aligned} u_k^{(1)}\left(\mathbf{x},\boldsymbol{\xi},t\right) &= N_{kpq_1}^{(1)}\left(\boldsymbol{\xi}\right)\frac{\partial U_p}{\partial x_{q_1}} + \widetilde{N}_{kq_1}^{(1)}\left(\boldsymbol{\xi}\right)\frac{\partial \Phi}{\partial x_{q_1}}, \\ \phi^{(1)}\left(\mathbf{x},\boldsymbol{\xi},t\right) &= W_{q_1}^{(1)}\left(\boldsymbol{\xi}\right)\frac{\partial \Phi}{\partial x_{q_1}} + \widetilde{W}_{pq_1}^{(1)}\left(\boldsymbol{\xi}\right)\frac{\partial U_p}{\partial x_{q_1}}, \end{aligned} \tag{8}$$

where $N_{kpq_1}^{(1)}$, $\widetilde{N}_{kq_1}^{(1)}$, $W_{q_1}^{(1)}$, $\widetilde{W}_{pq_1}^{(1)}$ are the first order perturbation functions, only depending on the geometric and physical properties of the microstructure, that will be evaluated in the following.
Finally, the solution of the ε^{0}-order problem, in (46), is

$$\begin{aligned} u_k^{(2)}\left(\mathbf{x},\boldsymbol{\xi},t\right) &= N_{kpq_1q_2}^{(2)}\left(\boldsymbol{\xi}\right)\frac{\partial^2 U_p}{\partial x_{q_1}\partial x_{q_2}} + \widetilde{N}_{kq_1q_2}^{(2)}\left(\boldsymbol{\xi}\right)\frac{\partial^2 \Phi}{\partial x_{q_1}\partial x_{q_2}} + \widehat{N}_{kp}^{(2)}\left(\boldsymbol{\xi}\right)\ddot{U}_p, \\ \phi^{(2)}\left(\mathbf{x},\boldsymbol{\xi},t\right) &= W_{q_1q_2}^{(2)}\left(\boldsymbol{\xi}\right)\frac{\partial^2 \Phi}{\partial x_{q_1}\partial x_{q_2}} + \widetilde{W}_{pq_1q_2}^{(2)}\left(\boldsymbol{\xi}\right)\frac{\partial^2 U_p}{\partial x_{q_1}\partial x_{q_2}} + \widehat{W}_{q_1q_2}^{(2)}\left(\boldsymbol{\xi}\right)\ddot{U}_p, \end{aligned} \tag{9}$$

being $N_{kpq_1q_2}^{(2)}$, $\widetilde{N}_{kq_1q_2}^{(2)}$, $\widehat{N}_{kp}^{(2)}$, $W_{q_1q_2}^{(2)}$, $\widetilde{W}_{pq_1q_2}^{(2)}$, and $\widehat{W}_{q_1q_2}^{(2)}$ the second order perturbation functions.
The perturbation functions are determined, in turn, by solving two sets of hierarchical differential problems referred to as cell problems. The cell problems are obtained by properly manipulating the recursive problems, reported in Appendix A, and exploiting the structure of the sensitivities in (7)-(9), according with (Smyshlyaev and Cherednichenko, 2000; Fantoni et al., 2017). It is remarked that the source terms involved in such cell problems are characterized by zero mean values in the Unit Cell $\mathfrak{Q}$. As a consequence, they admit sufficiently regular and $\mathfrak{Q}$-periodic solutions. Moreover, the uniqueness of cell problems solutions is guaranteed by enforcing the normalization condition of the perturbation functions, i.e. assuring zero mean values in $\mathfrak{Q}$.
The two cell problems at the order ε^{-1} read

$$\begin{aligned} &\left(C_{ijkl}^{m}N_{kpq_1,l}^{(1)}\right)_{,j} + \left(e_{ijk}^{m}\widetilde{W}_{pq_1,k}^{(1)}\right)_{,j} + C_{ijpq_1,j}^{m} = 0, \\ &\left(e_{kli}^{m}N_{kpq_1,l}^{(1)}\right)_{,i} - \left(\beta_{il}^{m}\widetilde{W}_{pq_1,l}^{(1)}\right)_{,i} + e_{pq_1i,i}^{m} = 0, \end{aligned} \tag{10}$$

$$\begin{aligned}
&\left(C^m_{ijkl}\widetilde{N}^{(1)}_{kq_1,l}\right)_{,j}+\left(e^m_{ijk}W^{(1)}_{q_1,k}\right)_{,j}+e^m_{ijq_1,j}=0,\\
&\left(e^m_{kli}\widetilde{N}^{(1)}_{kq_1,l}\right)_{,i}-\left(\beta^m_{il}W^{(1)}_{q_1,l}\right)_{,i}-\beta^m_{iq_1,i}=0,
\end{aligned}\tag{11}$$

in terms of the first order perturbation functions.

Finally, the three cell problems at the order ε^0 are

$$\begin{aligned}
&\left(C^m_{ijkl}N^{(2)}_{kpq_1q_2,l}\right)_{,j}+\left(e^m_{ijk}\widetilde{W}^{(2)}_{pq_1q_2,k}\right)_{,j}+\frac{1}{2}\left[\left(C^m_{ijpq_2}N^{(1)}_{kpq_1}\right)_{,j}+C^m_{iq_2kl}+C^m_{iq_2kl}N^{(1)}_{kpq_1,l}+\left(e^m_{ijq_2}\widetilde{W}^{(1)}_{pq_1}\right)_{,j}+\right.\\
&\left.+e^m_{iq_2k}\widetilde{W}^{(1)}_{pq_1,k}+\left(C^m_{ijpq_1}N^{(1)}_{kpq_2}\right)_{,j}+C^m_{iq_1kl}+C^m_{iq_1kl}N^{(1)}_{kpq_2,l}+\left(e^m_{ijq_1}\widetilde{W}^{(1)}_{pq_2}\right)_{,j}+e^m_{iq_1k}\widetilde{W}^{(1)}_{pq_2,k}\right]=\\
&=\frac{1}{2}\langle C^m_{iq_1pq_2}+C^m_{iq_2kl}N^{(1)}_{kpq_1,l}+e^m_{iq_2k}\widetilde{W}^{(1)}_{pq_1,k}+C^m_{iq_2pq_1}+C^m_{iq_1kl}N^{(1)}_{kpq_2,l}+e^m_{iq_1k}\widetilde{W}^{(1)}_{pq_2,k}\rangle,\\
&\left(e^m_{kli}N^{(2)}_{kpq_1q_2,l}\right)_{,i}-\left(\beta^m_{il}\widetilde{W}^{(2)}_{pq_1q_2,l}\right)_{,i}+\frac{1}{2}\left[\left(e^m_{kq_2i}N^{(1)}_{kpq_1}\right)_{,i}+e^m_{klq_2}N^{(1)}_{kpq_1,l}+e^m_{pq_2q_1}-\left(\beta^m_{iq_2}\widetilde{W}^{(1)}_{pq_1}\right)_{,i}+\right.\\
&\left.-\beta^m_{q_2l}\widetilde{W}^{(1)}_{pq_1,l}+\left(e^m_{kq_1i}N^{(1)}_{kpq_2}\right)_{,i}+e^m_{klq_1}N^{(1)}_{kpq_2,l}+e^m_{pq_1q_2}-\left(\beta^m_{iq_1}\widetilde{W}^{(1)}_{pq_2}\right)_{,i}-\beta^m_{q_1l}\widetilde{W}^{(1)}_{pq_2,l}\right]=\frac{1}{2}\left\langle e^m_{klq_2}N^{(1)}_{kpq_1,l}+\right.\\
&\left.+e^m_{pq_2q_1}-\beta^m_{q_2l}\widetilde{W}^{(1)}_{pq_1,l}+e^m_{klq_1}N^{(1)}_{kpq_2,l}+e^m_{pq_1q_2}-\beta^m_{q_1l}\widetilde{W}^{(1)}_{pq_2,l}\right\rangle,
\end{aligned}\tag{12}$$

$$\begin{aligned}
&\left(C^m_{ijkl}\widetilde{N}^{(2)}_{kq_1q_2,l}\right)_{,j}+\left(e^m_{ijk}W^{(2)}_{q_1q_2,k}\right)_{,j}+\frac{1}{2}\left[\left(C^m_{ijkq_2}\widetilde{N}^{(1)}_{kq_1}\right)_{,j}+C^m_{iq_2kl}\widetilde{N}^{(1)}_{kq_1,l}+\left(e^m_{ijq_2}W^{(1)}_{q_1}\right)_{,j}+\right.\\
&\left.+e^m_{iq_1q_2}+e^m_{iq_2k}W^{(1)}_{q_1,k}+\left(C^m_{ijkq_1}\widetilde{N}^{(1)}_{kq_2}\right)_{,j}+C^m_{iq_1kl}\widetilde{N}^{(1)}_{kq_2,l}+\left(e^m_{ijq_1}W^{(1)}_{q_2}\right)_{,j}+e^m_{iq_2q_1}+e^m_{iq_1k}W^{(1)}_{q_2,k}\right]=\\
&=\frac{1}{2}\langle C^m_{iq_2kl}\widetilde{N}^{(1)}_{kpq_1,l}+e^m_{iq_1q_2}+e^m_{iq_2k}W^{(1)}_{q_1,k}+C^m_{iq_1kl}\widetilde{N}^{(1)}_{kpq_2,l}+e^m_{iq_2q_1}+e^m_{iq_1k}W^{(1)}_{q_2,k}\rangle,\\
&\left(e^m_{kli}\widetilde{N}^{(2)}_{kq_1q_2,l}\right)_{,i}-\left(\beta^m_{il}W^{(2)}_{q_1q_2,l}\right)_{,i}+\frac{1}{2}\left[\left(e^m_{kq_2i}\widetilde{N}^{(1)}_{kq_1}\right)_{,i}+e^m_{klq_2}\widetilde{N}^{(1)}_{kq_1,l}-\left(\beta^m_{iq_2}W^{(1)}_{q_1}\right)_{,i}-\beta^m_{q_1q_2}+\right.\\
&\left.-\beta^m_{q_2l}W^{(1)}_{q_1,l}+\left(e^m_{kq_1i}\widetilde{N}^{(1)}_{kq_2}\right)_{,i}+e^m_{klq_1}\widetilde{N}^{(1)}_{kq_2,l}-\left(\beta^m_{iq_1}W^{(1)}_{q_2}\right)_{,i}-\beta^m_{q_2q_1}-\beta^m_{q_1l}W^{(1)}_{q_2,l}\right]=\frac{1}{2}\left\langle e^m_{klq_2}\widetilde{N}^{(1)}_{kq_1,l}+\right.\\
&\left.-\beta^m_{q_1q_2}-\beta^m_{q_2l}W^{(1)}_{q_1,l}+e^m_{klq_1}\widetilde{N}^{(1)}_{kq_2,l}-\beta^m_{q_2q_1}-\beta^m_{q_1l}W^{(1)}_{q_2,l}\right\rangle
\end{aligned}\tag{13}$$

$$\begin{aligned}
&\left(C^m_{ijkl}\widehat{N}^{(2)}_{kp,l}\right)_{,j}+\left(e^m_{ijk}\widehat{W}^{(2)}_{p,k}\right)_{,j}-\rho^m\delta_{pi}=-\langle\rho^m\rangle\delta_{pi},\\
&\left(e^m_{kli}\widehat{N}^{(2)}_{kp,l}\right)_{,i}-\left(\beta^m_{il}\widehat{W}^{(2)}_{p,l}\right)_{,i}=0
\end{aligned}\tag{14}$$

in terms of the first order perturbation functions, where a proper symmetrization with respect to indices q_1 and q_2 has been introduced. The symbol $\langle(\cdot)\rangle=1/|\mathfrak{Q}|\int_{\mathfrak{Q}}(\cdot)d\boldsymbol{\xi}$ has been introduced, $|\mathfrak{Q}|=\eta$, and δ_{pi}

is the Kronecker delta function.

After determining the perturbation functions, by solving the cell problems, the so-called down-scaling relations can be rigorously determined. In particular, by plugging the terms in (7)-(9) into the asymptotic expansion (4), the following down-scaling relations are found

$$\begin{aligned}
&u_k\left(\mathbf{x},\boldsymbol{\xi},t\right)=U_k\left(\mathbf{x},t\right)+\varepsilon\left(N^{(1)}_{kpq_1}\left(\boldsymbol{\xi}\right)\frac{\partial U_p}{\partial x_{q_1}}+\widetilde{N}^{(1)}_{kq_1}\left(\boldsymbol{\xi}\right)\frac{\partial \varPhi}{\partial x_{q_1}}\right)+\varepsilon^2\left(N^{(2)}_{kpq_1q_2}\left(\boldsymbol{\xi}\right)\frac{\partial^2 U_p}{\partial x_{q_1}\partial x_{q_2}}+\right.\\
&\left.+\widetilde{N}^{(2)}_{kq_1q_2}\left(\boldsymbol{\xi}\right)\frac{\partial^2 \varPhi}{\partial x_{q_1}\partial x_{q_2}}+\widehat{N}^{(2)}_{kp}\left(\boldsymbol{\xi}\right)\ddot{U}_p\right)+\mathcal{O}\left(\varepsilon^{\mathbf{3}}\right),\\
&\phi\left(\mathbf{x},\boldsymbol{\xi},t\right)=\varPhi\left(\mathbf{x},t\right)+\varepsilon\left(W^{(1)}_{q_1}\left(\boldsymbol{\xi}\right)\frac{\partial \varPhi}{\partial x_{q_1}}+\widetilde{W}^{(1)}_{pq_1}\left(\boldsymbol{\xi}\right)\frac{\partial U_p}{\partial x_{q_1}}\right)+\varepsilon^2\left(W^{(2)}_{q_1q_2}\left(\boldsymbol{\xi}\right)\frac{\partial^2 \varPhi}{\partial x_{q_1}\partial x_{q_2}}+\right.\\
&\left.+\widetilde{W}^{(2)}_{pq_1q_2}\left(\boldsymbol{\xi}\right)\frac{\partial^2 U_p}{\partial x_{q_1}\partial x_{q_2}}+\widehat{W}^{(2)}_{p}\left(\boldsymbol{\xi}\right)\ddot{U}_p\right)+\mathcal{O}\left(\varepsilon^{\mathbf{3}}\right),
\end{aligned} \tag{15}$$

where the microscopic fields are made dependent on the corresponding macroscopic ones.

The up-scaling relations are, in turn, determined as

$$\begin{aligned}
U_k\left(\mathbf{x},t\right)&\doteq\left\langle u_k\left(\mathbf{x},\frac{\mathbf{x}}{\varepsilon}+\boldsymbol{\zeta},t\right)\right\rangle_{\boldsymbol{\zeta}},\\
\varPhi\left(\mathbf{x},t\right))&\doteq\left\langle \phi\left(\mathbf{x},\frac{\mathbf{x}}{\varepsilon}+\boldsymbol{\zeta},t\right)\right\rangle_{\boldsymbol{\zeta}},
\end{aligned} \tag{16}$$

where $\boldsymbol{\zeta}\in\mathfrak{Q}$ is a *translation variable*, such that the vector $\varepsilon\,\boldsymbol{\zeta}\in\mathfrak{A}$ defines a translation of the heterogeneous medium with respect to $\mathfrak{L}$-periodic source terms (Smyshlyaev and Cherednichenko, 2000; Bacigalupo, 2014), and $\langle(\cdot)\rangle_{\boldsymbol{\zeta}}=1/|\mathfrak{Q}|\int_{\mathfrak{Q}}(\cdot)d\boldsymbol{\zeta}$. It is pointed out that the perturbation functions fulfil the invariance property satisfied by $\mathfrak{Q}$-periodic functions $g(\boldsymbol{\xi}+\boldsymbol{\zeta})|_{\boldsymbol{\xi}=\mathbf{x}/\varepsilon}$, such that $\langle g(\mathbf{x}/\varepsilon+\boldsymbol{\zeta})\rangle_{\boldsymbol{\zeta}}|\mathfrak{Q}|=\int\limits_{\mathfrak{Q}}g(\mathbf{x}/\varepsilon+\boldsymbol{\zeta})d\boldsymbol{\zeta}=\int\limits_{\mathfrak{Q}}g(\boldsymbol{\xi}+\boldsymbol{\zeta})d\boldsymbol{\zeta}=\int\limits_{\mathfrak{Q}}g(\boldsymbol{\xi}+\boldsymbol{\zeta})d\boldsymbol{\xi}=\langle g(\boldsymbol{\xi}+\boldsymbol{\zeta})\rangle|\mathfrak{Q}|$.

4 Identification of the homogenized constitutive tensors

The macroscopic piezoelectric constitutive properties and the macroscopic inertial term are derived by exploiting a generalized macro-homogeneity condition, establishing an energy equivalence between the macroscopic and the microscopic scales. To this aim, the generalized microscopic mean Lagrangian $\overline{\mathcal{L}}_m$, inspired by (Smyshlyaev and Cherednichenko, 2000; Bacigalupo, 2014), and the corresponding generalized macroscopic Lagrangian $\mathcal{L}_M$ are taken into account. Note that focus is on the identification of a first order homogenized continuum.

More specifically, the generalized microscopic mean Lagrangian is defined on the basis of the microscopic kinetic energy density t_m and of the microscopic electric enthalpy density h_m, as

$$\begin{aligned}\overline{\mathcal{L}}_m &= \int_{\mathfrak{L}} \left[\frac{1}{|\mathfrak{Q}|}\int_{\mathfrak{Q}} \left(t_m\left(\mathbf{x}, \frac{\mathbf{x}}{\varepsilon} + \boldsymbol{\zeta}, t\right) - h_m\left(\mathbf{x}, \frac{\mathbf{x}}{\varepsilon} + \boldsymbol{\zeta}, t\right) + w_m\left(\mathbf{x}, \frac{\mathbf{x}}{\varepsilon} + \boldsymbol{\zeta}, t\right)\right) d\boldsymbol{\zeta}\right] d\mathbf{x} = \\ &= \int_{\mathfrak{L}} \langle t_m - h_m + w_m \rangle d\mathbf{x},\end{aligned} \tag{17}$$

where the down-scaling relations have been exploited to express the densities t_m, h_m and w_m as asymptotic expansions in terms of the macroscopic displacement U_i and electric potential $\varPhi$, respectively, i.e.

$$\begin{aligned}
& t_m = \frac{1}{2}\rho^m \dot{u}_i \dot{u}_i = \frac{1}{2}\rho^m \dot{U}_i \dot{U}_i + \mathcal{O}\left(\varepsilon\right), \\
& h_m = \frac{1}{2} C^m_{ijhk} \frac{Du_i}{Dx_j}\frac{Du_h}{Dx_k} + e^m_{ijh}\frac{D\phi}{Dx_h}\frac{Du_i}{Dx_j} - \frac{1}{2}\beta^m_{ij}\frac{D\phi}{Dx_i}\frac{D\phi}{Dx_j} = \\
& = \frac{1}{2}\left[C^m_{ijhk}\left(\delta_{ip}\delta_{jq_1} + N^{(1)}_{ipq_1,j}\right)\left(\delta_{hs}\delta_{kr_1} + N^{(1)}_{hsr_1,k}\right) + 2e^m_{ijh}\left(\delta_{ip}\delta_{jq_1} + N^{(1)}_{ipq_1,j}\right)\widetilde{W}^{(1)}_{sr_1,h} + \right. \\
& \left. -\beta^m_{ij}\widetilde{W}^{(1)}_{pq_1,j}\widetilde{W}^{(1)}_{sr_1,i}\right]\frac{\partial U_p}{\partial x_{q_1}}\frac{\partial U_s}{\partial x_{r_1}} + \left[C^m_{ijhk}\left(\delta_{ip}\delta_{jq_1} + N^{(1)}_{ipq_1,j}\right)\widetilde{N}^{(1)}_{hr_1,k} + e^m_{ijh}\left(\delta_{ip}\delta_{jq_1} + N^{(1)}_{ipq_1,j}\right)\right. \\
& \left(\delta_{hr_1} + W^{(1)}_{r_1,h}\right) + e^m_{ijh}\widetilde{N}^{(1)}_{ir_1,j}\widetilde{W}^{(1)}_{pq_1,h} - \left.\beta^m_{ij}\widetilde{W}^{(1)}_{pq_1,j}\left(\delta_{ir_1} + W^{(1)}_{r_1,i}\right)\right]\frac{\partial U_p}{\partial x_{q_1}}\frac{\partial \varPhi}{\partial x_{r_1}} - \frac{1}{2}\left[\beta^m_{ij}\left(\delta_{jq_1} + W^{(1)}_{q_1,j}\right)\right. \\
& \left.\left(\delta_{ir_1} + W^{(1)}_{r_1,i}\right) - C^m_{ijhk}\widetilde{N}^{(1)}_{iq_1,j}\widetilde{N}^{(1)}_{hr_1,k} - 2e^m_{ijh}\widetilde{N}^{(1)}_{iq_1,j}\left(\delta_{hr_1} + \widetilde{W}^{(1)}_{r_1,h}\right)\right]\frac{\partial \varPhi}{\partial x_{q_1}}\frac{\partial \varPhi}{\partial x_{r_1}} + \mathcal{O}\left(\varepsilon\right), \\
& w_m = b_i u_i - \rho_e \phi = b_i U_i - \rho_e \varPhi + \mathcal{O}\left(\varepsilon\right).
\end{aligned} \tag{18}$$

Analogously, the generalized macroscopic Lagrangian is given as

$$\mathcal{L}_M = \int_{\mathfrak{L}} \left(t_M\left(\mathbf{x}, t\right) - h_M\left(\mathbf{x}, t\right) + w_M\left(\mathbf{x}, t\right)\right) d\mathbf{x}, \tag{19}$$

in terms of the macroscopic kinetic energy density t_M, of the macroscopic electric enthalpy density h_M and the density w_M, expressed in the following form

$$\begin{aligned}
& t_M = \frac{1}{2}\rho \dot{U}_i \dot{U}_i, \\
& h_M = \frac{1}{2} C_{pq_1sr_1}\frac{\partial U_p}{\partial x_{q_1}}\frac{\partial U_s}{\partial x_{r_1}} + e_{pq_1r_1}\frac{\partial U_p}{\partial x_{q_1}}\frac{\partial \varPhi}{\partial x_{r_1}} - \frac{1}{2}\beta_{q1r1}\frac{\partial \varPhi}{\partial x_{q_1}}\frac{\partial \varPhi}{\partial x_{r_1}}, \\
& w_M = b_i U_i - \rho_e \varPhi.
\end{aligned} \tag{20}$$

involving the components of the macroscopic constitutive tensors and of the macroscopic inertial term of the piezoelectric first order continuum.

The generalized macro-homogeneity condition is, thus, defined by

$$\overline{\mathcal{L}}_m^0 \doteq \mathcal{L}_M, \tag{21}$$

where $\overline{\mathcal{L}}_m^0$ identifies the generalized microscopic mean Lagrangian truncated at order 0-th, i.e. retaining only the coefficients of ε^0. It follows that the components of macroscopic piezoelectric constitutive properties and the macroscopic inertial term result as

$$\begin{aligned}
&\rho = \langle \rho^m \rangle, \\
&C_{pq_1sr_1} = \frac{1}{2}\left\langle C^m_{ijhk}\left(\delta_{ip}\delta_{jq_1} + N^{(1)}_{ipq_1,j}\right)\left(\delta_{hs}\delta_{kr_1} + N^{(1)}_{hsr_1,k}\right) + 2e^m_{ijh}\left(\delta_{ip}\delta_{jq_1} + N^{(1)}_{ipq_1,j}\right)\widetilde{W}^{(1)}_{sr_1,h} + \right. \\
&\left. -\beta^m_{ij}\widetilde{W}^{(1)}_{pq_1,j}\widetilde{W}^{(1)}_{sr_1,i}\right\rangle, \\
&e_{pq_1r_1} = \left\langle C^m_{ijhk}\left(\delta_{ip}\delta_{jq_1} + N^{(1)}_{ipq_1,j}\right)\widetilde{N}^{(1)}_{hr_1,k} + e^m_{ijh}\left(\delta_{ip}\delta_{jq_1} + N^{(1)}_{ipq_1,j}\right)\left(\delta_{hr_1} + W^{(1)}_{r_1,h}\right) + \right. \\
&\left. + e^m_{ijh}\widetilde{N}^{(1)}_{ir_1,j}\widetilde{W}^{(1)}_{pq_1,h} - \beta^m_{ij}\widetilde{W}^{(1)}_{pq_1,j}\left(\delta_{ir_1} + W^{(1)}_{r_1,i}\right)\right\rangle, \\
&\beta_{q_1r_1} = \frac{1}{2}\left\langle \beta^m_{ij}\left(\delta_{jq_1} + W^{(1)}_{q_1,j}\right)\left(\delta_{ir_1} + W^{(1)}_{r_1,i}\right) - C^m_{ijhk}\widetilde{N}^{(1)}_{iq_1,j}\widetilde{N}^{(1)}_{hr_1,k} - 2e^m_{ijh}\widetilde{N}^{(1)}_{iq_1,j}\left(\delta_{hr_1} + \widetilde{W}^{(1)}_{r_1,h}\right)\right\rangle.
\end{aligned} \tag{22}$$

Hence, they are expressed in terms of the perturbation functions and in terms of the components of the microscopic constitutive tensors and of the microscopic inertial term.

It is worth noting that first order homogenization schemes may lack in accurateness in modelling size-effects and non-local phenomena related to microstructural length scales. This drawback is particularly evident when severe stress and strain gradients are involved. With the aim of overcoming such issues, non-local higher order homogenization techniques can be used, see (Smyshlyaev and Cherednichenko, 2000; Bacigalupo, 2014; Addessi et al., 2016; Bacigalupo et al., 2017; Ameen et al., 2018). A more accurate description of the response of the considered piezoelectric heterogeneous material can be, indeed, consistently obtained resorting to such homogenization approaches, in which the generalized macro-homogeneity condition is properly modified, both taking into account higher order terms in the asymptotic expansions at the microscopic scale, and nonlocal constitutive tensors and inertial terms at the macroscopic level. An alternative rigorous and general approach is schematically reported in Appendix B. It consists in solving the so-called average field equations of infinite order (48), via perturbation methods. An infinite hierarchical set of macroscopic partial differential problems is, thus, obtained and higher order approximations can be obtained by properly truncating the asymptotic expansion of U_i and $\mathit{\Phi}$. In this framework, the piezoelectric behaviour of the microstructured material can be achieved also in the presence of strong gradients.

5 Characterization of dispersive wave propagation in piezoelectric periodic materials

The problem of characterizing the wave propagation in piezoelectric periodic materials can be addressed through the Floquet-Bloch theory, which is able to deduce the frequency band structure of the material characterized by periodic microstructure. Nevertheless, this approach could be computationally cumbersome in the case of very complex microstructural topologies. In this respect, a valuable alternative is the use of homogenization techniques, adopting either local or non-local approaches. More specifically, when first order approaches are used, an accurate description is obtained in the case of in the long wavelength regime.

With this in mind, in the following Section 5.1 the heterogeneous material is investigated to determine its frequency spectrum, with both acoustic and optical branches, while the Section 5.2 is devoted to determine the dispersive functions approximating only the acoustic branches in the long wavelength regime, adopting a first order asymptotic homogenization approach.

5.1 Frequency band structure of the heterogeneous material with periodic microstructure

In this Section, consistently with the rigorous Floquet-Bloch theory (Floquet, 1883; Bloch, 1928; Brillouin, 1960), a generalization to piezoelectric materials is used to study the band structure of the microstructured periodic material. To this aim we apply the time Fourier transform to the partial differential equations (1) at the microscopic scale, in the case of zero source terms, i.e. b_i=0 and ρ_e=0. For the sake of completeness, we recall the time Fourier transform for a generic $g(\mathbf{x}, t)$ is defined as

$$\mathcal{F}_t\left[g(\mathbf{x},t)\right] = \int_{-\infty}^{+\infty} g(\mathbf{x},t)e^{-\iota\omega t}d\mathbf{x} = \widehat{g}(\mathbf{x},\omega), \tag{23}$$

where the angular frequency $\omega \in \mathbb{R}$. The resulting generalized Christoffel equations are, thus, obtained as

$$\begin{aligned} &\frac{D}{Dx_j}\left(C_{ijkl}^{(m,\varepsilon)}\frac{D\widehat{u}_k}{Dx_l}\right) + \frac{D}{Dx_j}\left(e_{ijk}^{(m,\varepsilon)}\frac{D\widehat{\phi}}{Dx_k}\right) + \rho^{(m,\varepsilon)}\omega^2\widehat{u}_i = 0,\\ &\frac{D}{Dx_i}\left(\widetilde{e}_{ikl}^{(m,\varepsilon)}\frac{D\widehat{u}_k}{Dx_l}\right) - \frac{D}{Dx_i}\left(\beta_{il}^{(m,\varepsilon)}\frac{D\widehat{\phi}}{Dx_l}\right) = 0, \end{aligned} \tag{24}$$

in which the the well-known property $\mathcal{F}_t(\frac{\partial^n g(\mathbf{x},t)}{\partial t^n}) = (\iota\omega)^n\widehat{g}(\mathbf{x},\omega)$ has been exploited.

Due to the periodicity of the microstructured medium, only the Periodic Cell $\mathfrak{A}$ is analysed, subject to the Floquet-Bloch boundary conditions, that is

$$\widehat{u}_i^{+} = \widehat{u}_i^{-}e^{\iota k_j v_j^{(p)}}, \tag{25}$$

$$\widehat{\phi}^{+} = \widehat{\phi}^{-} e^{\iota k_j v_j^{(p)}}, \tag{26}$$

$$\widehat{\sigma}_{lr}^{+} = -\widehat{\sigma}_{lr}^{-}(m_r^{(p)})^{-} e^{\iota k_j v_j^{(p)}}, \tag{27}$$

$$\widehat{d}_r^{+}(m_r^{(p)})^{+} = -\widehat{d}_r^{-}(m_r^{(p)})^{-} e^{\iota k_j v_j^{(p)}}, \tag{28}$$

being $v_j^{(p)}$ the components of the vector of periodicity $\mathbf{v}_p = v_j^{(p)}\mathbf{e}_j$, and $(m_r^{(p)})^{\pm}$ the components of the outward normal $\mathbf{m}_p^{\pm} = (m_j^{(p)})^{\pm}\mathbf{e}_j$ to the boundary $\partial\mathbf{A}$, $j, p = 1, 2, 3$. Moreover, the apexes $^{\pm}$ are referred to the positive part $\partial\mathbf{A}^{+}$ (with outward normal $\mathbf{m}_p^{+}$) and the corresponding negative parts $\partial\mathbf{A}^{-}$ (with outward normal $\mathbf{m}_p^{-}$) of the Periodic Cell boundary. Note that for the generic function $\widehat{g}$ the following notation is used, i.e. $\widehat{g}^{\pm} \doteq \widehat{g}(\mathbf{x}^{\pm})$ where $\mathbf{x}^{\pm} \in \partial\mathbf{A}^{\pm}$, and $\mathbf{x}^{+} = \mathbf{x}^{-} + \mathbf{v}_p$. Finally, k_j are the components of the wave vector $\mathbf{k}$. In this context, the dimensionless first Brillouin zone $\mathfrak{B} = [-\pi, \pi] \times [-\pi, \pi] \times [-\pi, \pi]$ is defined in the space of the dimensionless wave vectors (whose components are $k_1 d$, $k_2 d$ and $k_3 h$) and is associated to the Periodic Cell $\mathfrak{A}$. Such Brillouin zone is characterized by three orthogonal vectors $\pi\mathbf{n}_i$, parallel to $\mathbf{e}_i$, with i=1,2,3.

5.2 Dispersion functions in the first order homogeneous material

A first order asymptotic homogenization approach is here adopted to study the dispersion functions of piezoelectric periodic material. The equations of motion for the homogenized continuum, in the absence of source terms take the following form

$$\begin{aligned} C_{ijkl}\frac{\partial^2 U_p}{\partial x_{q_1}\partial x_{q_2}} + e_{ijk}\frac{\partial^2 \Phi}{\partial x_{q_1}\partial x_{q_2}} &= \rho\ddot{U}_i, \\ \widetilde{e}_{ikl}\frac{\partial^2 U_p}{\partial x_{q_1}\partial x_{q_2}} - \beta_{il}\frac{\partial^2 \Phi}{\partial x_{q_1}\partial x_{q_2}} &= 0, \end{aligned} \tag{29}$$

where C_{ijkl} are the components of the fourth order macro elasticity tensor, e_{ijk} are the components of the third order macroscopic piezoelectric stress-charge coupling tensor, with the following relation between the components $\widetilde{e}_{ijk} = e_{jki}$. Moreover, β_{il} are the components of the second order macroscopic dielettric permittivity tensor and ρ is the macroscopic mass density, reported in Equation (22). Equations (29) are here properly manipulated, by first exploiting the time Fourier transform, see equation (23), and then the space Fourier transform in the macroscopic space, that is hereafter recalled

$$\mathcal{F}_{\mathbf{x}}\left[\widehat{g}(\mathbf{x}, \omega)\right] = \int_{\mathbb{R}^2} \widehat{g}(\mathbf{x}, \omega) e^{-\iota \mathbf{k}\mathbf{x}} d\mathbf{x} = \breve{\widehat{g}}(\mathbf{k}, \omega), \tag{30}$$

where $\mathbf{k} \in \mathbb{R}^2$ is the the wave vector, and recalling the property $\mathcal{F}_{\mathbf{x}}(\frac{\partial^n \widehat{g}(\mathbf{x},\omega)}{\partial x_j^n}) = (\imath k_j)^n \breve{\widehat{g}}(\mathbf{k},\omega)$ the following governing equations in the frequency and wave vector space are obtained

$$\begin{aligned} &- C_{ijkl} k_j k_l \breve{\widehat{U}}_k - e_{ikj} k_j k_k \breve{\widehat{\Phi}} + \rho \omega^2 \breve{\widehat{U}}_i = 0, \\ &- \widetilde{e}_{ikl} k_l k_i \breve{\widehat{U}}_k + \beta_{il} k_l k_i \breve{\widehat{\Phi}} = 0. \end{aligned} \tag{31}$$

Equation (31) can be rewritten in an equivalent form, after simple manipulations, in terms of the phase velocity and of the propagation direction, as

$$\begin{aligned} &- C_{ijkl} n_j n_l \breve{\widehat{U}}_k - e_{ikj} n_j n_k \breve{\widehat{\Phi}} + \rho c^2 \breve{\widehat{U}}_i = 0, \\ &- \widetilde{e}_{ikl} n_l n_i \breve{\widehat{U}}_k + \beta_{il} n_l n_i \breve{\widehat{\Phi}} = 0, \end{aligned} \tag{32}$$

where the phase velocity is $c = \omega/k$, the wave number is $k = ||\mathbf{k}||_2$ and the unit vector of propagation is $\mathbf{n} = \mathbf{k}/k$ with components n_j.

A static condensation is, at this stage, performed so that from the second equation in (32) we obtain $\breve{\widehat{\Phi}} = \widetilde{e}_{ikl} n_l n_i \breve{\widehat{U}}_k / (\beta_{il} n_l n_i)$ and, after substituting in the first equation in (32), the eigenproblem governing the Bloch-wave propagation, expressed in terms of phase velocity and the transformed displacement components, is obtained as

$$\left(C_{ijkl} n_j n_l + e_{ijq} n_j n_q \frac{\widetilde{e}_{pkl} n_l n_p}{\beta_{rs} n_s n_r} - \rho c^2 \delta_{ki} \right) \breve{\widehat{U}}_k = 0, \quad i = 1, 2, 3, \tag{33}$$

where $\widetilde{e}_{pkl} = e_{klp}$ is exploited. Note that for any unit vector of propagation $\mathbf{n}$, the eigenvalues c^2 are the square of the wave velocity in the first order homogenized continuum. The corresponding eigenvectors, whose components $\breve{\widehat{U}}_k$ correspond to the time and space Fourier transform of the components of the macroscopic displacement in the first order homogenized continuum, identify the components of the polarization vector.

It is underlined that the use of a first order homogenized material implies some limitations in the characterization of dispersive wave propagation in periodic heterogeneous materials. A way out to overcome this problem is the use of higher order homogenization techniques that naturally account for additional higher order constitutive and inertial terms. A more accurate description of non-local waves dispersion is, thus, achieved, as shown in (Bacigalupo and Gambarotta, 2014; Hui and Oskay, 2014; De Domenico and Askes, 2016; Tan and Poh, 2018).

6 Illustrative applications

In this Section some illustrative examples are shown. We refer to the realistic assumption of materials with periodic cells characterized by orthogonal periodic vectors, as schematically shown in Figure 1. First, the components of the homogenized constitutive tensors, characterizing the composite material with periodic nano-structure, are shown for different geometric parameters, i.e. the height of the nanorods and their volumetric density. Then, both the results obtained with a micromechanical model and with a first order piezoelectric homogenized model are compared with each other, in the case of an extensional nanoscopic generator. Moreover, the influence of the volumetric density on the overall efficiency of such extensional nanostructured devices has been investigated in order to provide broad guidelines to maximize their efficiency.

Both analytic and numerical solutions are considered. Concerning the latter ones, finite elements analyses have been performed adopting fully coupled tetrahedral second order elements with displacements and electric potential independent degrees of freedom.

6.1 Homogenized piezoelectric properties

We consider a hybrid piezoelectric nanogenerator made of equispaced ZnO-nanorods embedded in a polymeric matrix and sandwiched in two homogeneous polymeric layers. The homogenized constitutive properties of the piezoelectric material are investigated with reference to the Periodic Cell, shown in Figure 2(a). The Periodic Cell $\mathfrak{A} = [-d/2, d/2] \times [-d/2, d/2] \times [-h/2, h/2]$ is characterized by the three orthogonal periodicity vectors $\mathbf{v}_1$, $\mathbf{v}_2$ and $\mathbf{v}_3$. We assume d=200 nm, the nanorod has hexagonal section with edge 80 nm, while the height in the polarization direction is h= 1100 nm, and the thickness of both top and bottom layers is 50 nm. Such average geometric values are representative of actual ZnO-rods based nanostructures, see Wang (2004).

The nanorod with hexagonal section is made of Zinc oxide with polarization along the vertical axis $\mathbf{e}_3$. Considering the ZnO material, see (Yang, 2004), the non-vanishing components of the elasticity tensor are: C^m_{1111} = 2.097 $\cdot 10^{11}$ Pa, C^m_{2222} = 2.097 $\cdot 10^{11}$ Pa, C^m_{3333} = 2.111 $\cdot 10^{11}$ Pa, C^m_{1122} = 1.211$\cdot 10^{10}$ Pa, C^m_{1133} = 1.053$\cdot 10^{10}$ Pa, C^m_{2233} = 1.053$\cdot 10^{10}$ Pa, C^m_{1212}= 4.237$\cdot 10^{10}$ Pa, C^m_{1313}= 4.237$\cdot 10^{10}$ Pa, C^m_{2323}= 4.424$\cdot 10^{10}$ Pa. Moreover, the non-vanishing components of the coupling tensor in the stress-charge form are: $\widetilde{e}^m_{311}$=$\widetilde{e}^m_{322}$ =-0.567 C/m^2, $\widetilde{e}^m_{333}$=1.3204 C/m^2, $\widetilde{e}^m_{113}$=$\widetilde{e}^m_{223}$=-0.4805 C/m^2. Finally, the non-vanishing components of the dielectric permittivity tensor are $\beta^m_{11}/\varepsilon_0$= $\beta^m_{22}/\varepsilon_0$=8.5446, $\beta^m_{33}/\varepsilon_0$=10.204, where ε_0=8.854 $\cdot 10^{-12}$ C/(Vm) is the vacuum permittivity. Both the matrix and the top and bottom layers are made out of an isotropic polymeric material doped with a highly conductive polymer (PANI), see (Huang and Zhang, 2004; Wang et al., 2005; Eftekhari, 2011; Almadhoun et al., 2014; Wang et al., 2015). The Young modulus is E= 535 MPA and the Poisson's coefficient is ν=0.4. We assume the dimensionless dielectric constant $\varepsilon_r^{P/PANI} = \beta/\varepsilon_0$=5.

A first numerical investigation concerns the influence of the heights of ZnO-nanorods on the overall piezoelectric constitutive response. The values of the actual height of the nanorods h_{nr} are supposed to vary between $0.5 \times h^*_{nr}$ and $2 \times h^*_{nr}$, where h^*_{nr}=1100 nm is the reference initial height. In Figure 2(b) the non-vanishing components of the homogenized elasticity tensor, normalized with respect to the corresponding components of bulk ZnO material, are plotted against $\alpha = h_{nr}/h^*_{nr}$. A monotonic increasing variation is found for all the considered components. As expected, C_{3333} (red curve) is the component most affected by the variation of α, with a maximum value about three times the initial one. The remaining components exhibit variations significantly lower, see the zoomed plot in Figure 2(b). Similar considerations apply to the components of the coupling tensor, shown in Figure 2(c). Only the component e_{333} (red curve) exhibits remarkable variations. Moreover, also the maximum variations of the components $\beta_{ij}/\beta^{ZnO}_{ij}$ are referred to the component β_{33} (red curve), see Figure 2(d).

The second numerical study is devoted to analyse the influence of the volumetric density of ZnO-nanorods on the overall constitutive response of the Periodic Cell. The density is defined as $\delta = V_{NR}/V$, i.e. the ratio between the volume occupied by the nanorods and the volume of a Periodic Cell, neglecting the contribution of the top and bottom layers. We let the density δ varying between a minimum value of about δ=0.066, corresponding to the case where d=500 nm in the Periodic Cell $\mathfrak{A}$, and a maximum value of about δ=0.65, for which d=160 nm, see the sketch in Figure 3(a).

In Figure 3(b) the dimensionless non-vanishing components of the homogenized elasticity tensor C_{ijhk} $/C^{ZnO}_{ijhk}$ are plotted versus the density δ. We observe that all the components monotonically increase, and the C_{3333} (red curve) shows the maximum variation between the extremal δ values. Moreover, due to the geometrical and material symmetries of the Periodic Cell, the curves related to the components C_{3333}, C_{1133} and C_{2233} are concave upward, while all the others have opposite concavity. The components e_{ijh}/e^{ZnO}_{ijh} are plotted in Figure 3(c). Again, monotonic variations are observed with maximum values reached for e_{333}. Finally, in Figure 3(d) the dimensionless non-vanishing components $\beta_{ij}/\beta^{ZnO}_{ij}$ are plotted, confirming monotonic variations that take maximum values for β_{33}. Note that the maximum variations are significantly lower than those shown by the components C_{3333} and e_{333}.

6.2 Benchmark tests: two-phase piezoelectric hybrid composite

We study the microstructured nanogenerators under two different loading conditions, considering a cluster of $m \times n$ cells (with base dimensions $L \times \frac{n}{m}L$ and height h), obtained by repeating the Periodic Cell along the periodicity vectors $\mathbf{v}_1$ and $\mathbf{v}_2$, see Figure 3(a) where a sketch is shown.

First benchmark test

First we consider a cluster of $n \times n$ cells and a uniform surface compressive load q applied on the top horizontal face of the specimen, while the displacements of the points on the bottom face are restricted in $\mathbf{e}_3$ direction. The electrodes are located along the top and bottom faces. Two alternative cases are considered, depending on the boundary conditions applied on the lateral faces. *Case* 1 is characterized

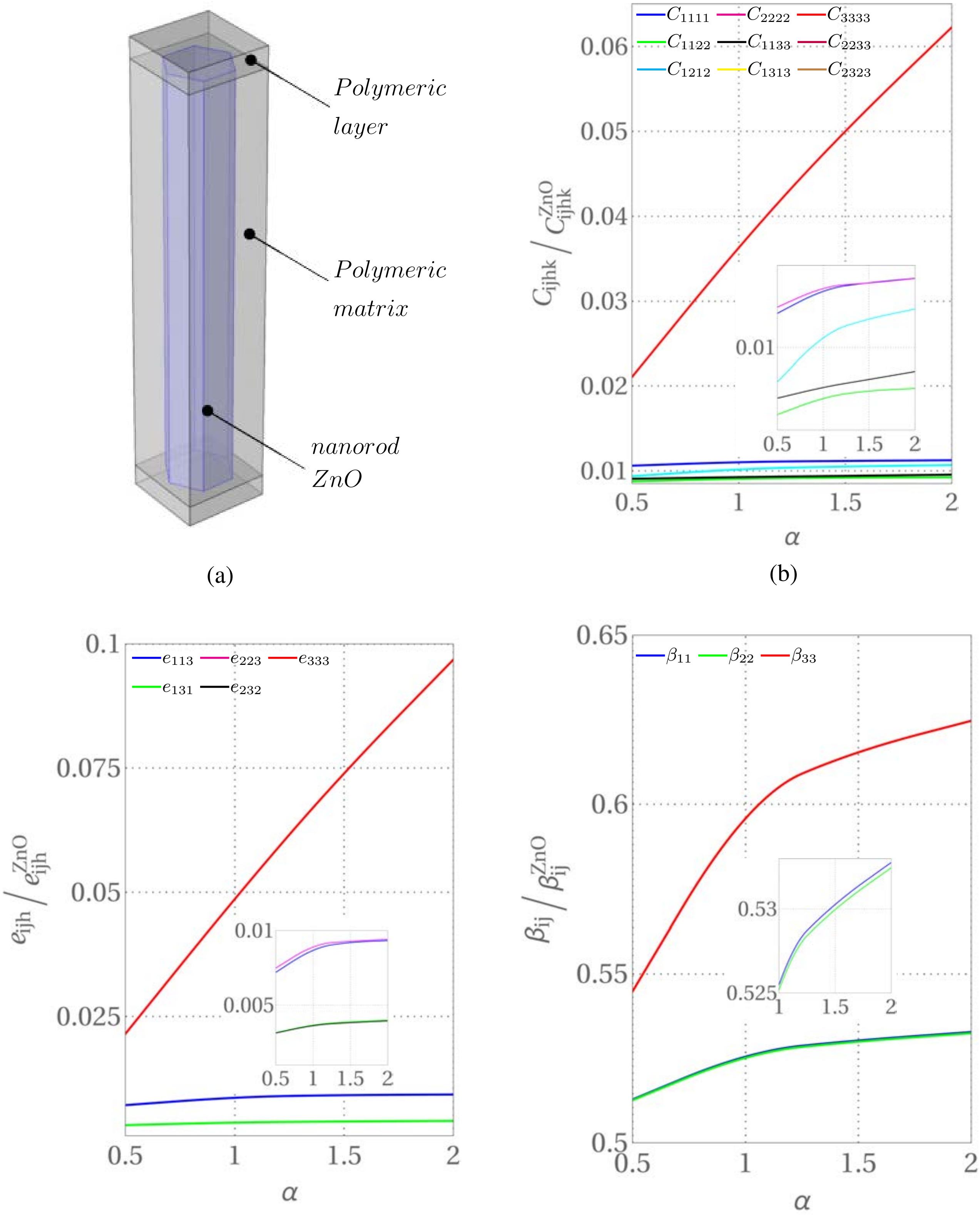

(a)

(b)

(c)

(d)

Fig. 2: Components of the homogenized constitutive tensors versus $\alpha = h_{nr}/h^*_{nr}$, with h^*_{nr}=1000 nm, for the Periodic Cell. (a) Schematic of the Periodic Cell. (b) Components of the elastic tensor. (c) Components of the coupling tensor. (d) Components of the dielectric permittivity tensor.

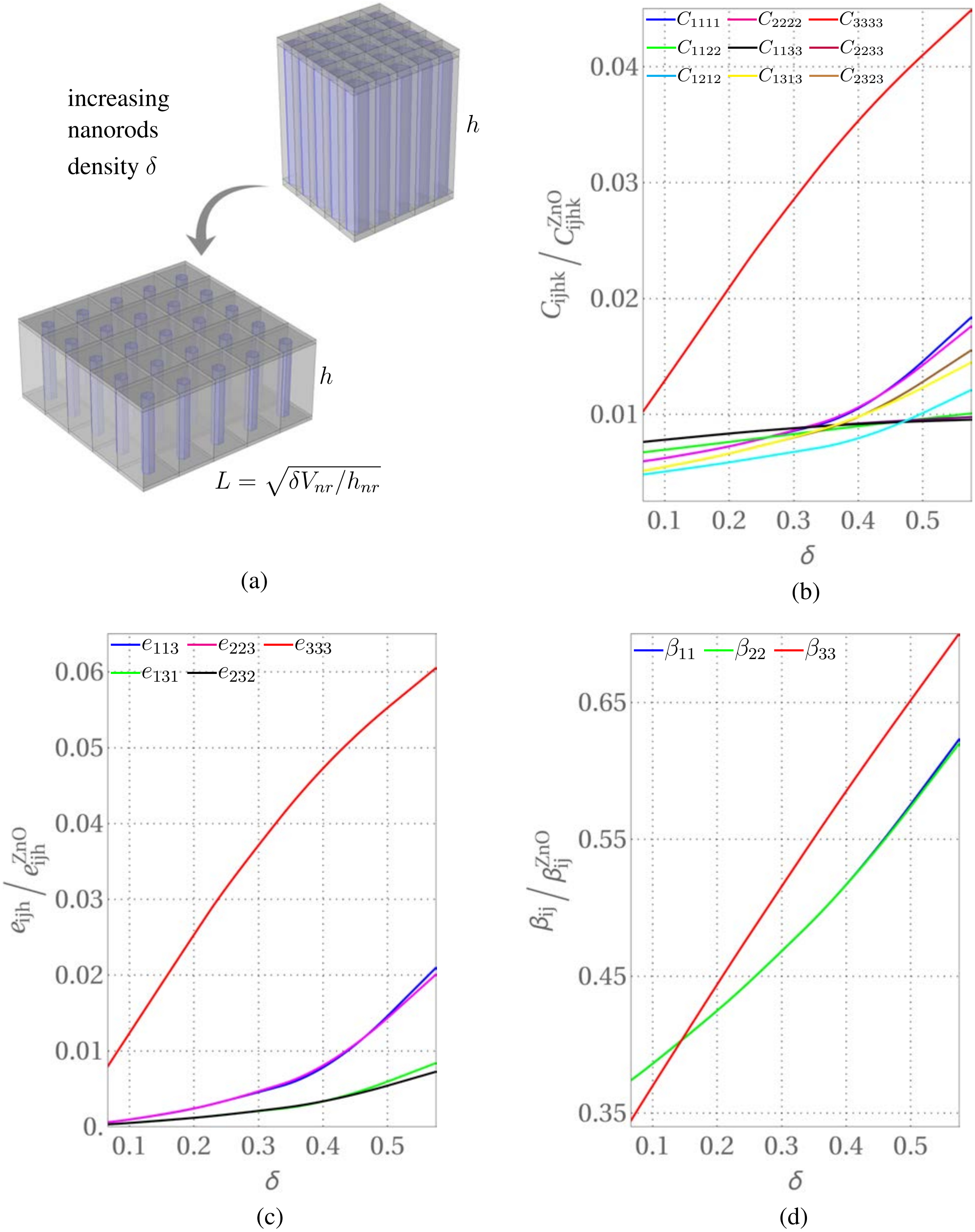

(a)

(b)

(c)

(d)

Fig. 3: Components of the homogenized constitutive tensors versus δ for the cluster of nanorods.(a) Cluster of 5×5 nanorods for different values of density δ. (b) Components of the elastic tensor. (c) Components of the coupling tensor. (d) Components of the dielectric permittivity tensor.

by free lateral faces, while in the $Case$ 2 the displacements are restricted along the outward normal to the lateral surface.

In order to reduce the computational costs involved in micromechanical analyses of such piezoelectric nanogenerators, their macroscopic behaviour can be satisfactorily described via a first order equivalent homogeneous material.

The macroscopic field equations of the first order homogenized continuum, specialized to the considered material symmetries, and with zero source terms, result as

$$\begin{aligned}
&\frac{\partial}{\partial x_1}\left(C_{1111}\frac{\partial U_1}{\partial x_1}+C_{1122}\frac{\partial U_2}{\partial x_2}+C_{1133}\frac{\partial U_3}{\partial x_3}\right)+\frac{\partial}{\partial x_3}\left(C_{1313}\left(\frac{\partial U_3}{\partial x_1}+\frac{\partial U_1}{\partial x_3}\right)\right)+\\
&+\frac{\partial}{\partial x_2}\left(C_{1212}\left(\frac{\partial U_2}{\partial x_1}+\frac{\partial U_1}{\partial x_2}\right)\right)+\frac{\partial}{\partial x_3}\left(e_{131}\frac{\partial \Phi}{\partial x_1}\right)+\frac{\partial}{\partial x_1}\left(e_{113}\frac{\partial \Phi}{\partial x_3}\right)=0,
\end{aligned}\tag{34}$$

$$\begin{aligned}
&\frac{\partial}{\partial x_2}\left(C_{2222}\frac{\partial U_2}{\partial x_2}+C_{2233}\frac{\partial U_3}{\partial x_3}+C_{1122}\frac{\partial U_2}{\partial x_2}\right)+\frac{\partial}{\partial x_3}\left(C_{3232}\left(\frac{\partial U_3}{\partial x_2}+\frac{\partial U_2}{\partial x_3}\right)\right)+\\
&+\frac{\partial}{\partial x_1}\left(C_{1212}\frac{\partial U_1}{\partial x_2}\right)+\frac{\partial}{\partial x_2}\left(e_{223}\frac{\partial \Phi}{\partial x_3}\right)+\frac{\partial}{\partial x_3}\left(e_{322}\frac{\partial \Phi}{\partial x_2}\right)=0,
\end{aligned}\tag{35}$$

$$\begin{aligned}
&\frac{\partial}{\partial x_3}\left(C_{3333}\frac{\partial U_3}{\partial x_3}+C_{1133}\frac{\partial U_1}{\partial x_1}+C_{2233}\frac{\partial U_2}{\partial x_2}\right)+\frac{\partial}{\partial x_2}\left(C_{3232}\left(\frac{\partial U_3}{\partial x_2}+\frac{\partial U_2}{\partial x_3}\right)\right)+\\
&+\frac{\partial}{\partial x_1}\left(C_{1313}\left(\frac{\partial U_3}{\partial x_1}+\frac{\partial U_1}{\partial x_3}\right)\right)+\frac{\partial}{\partial x_3}\left(e_{333}\frac{\partial \Phi}{\partial x_3}\right)+\frac{\partial}{\partial x_2}\left(e_{322}\frac{\partial \Phi}{\partial x_2}\right)+\frac{\partial}{\partial x_1}\left(e_{131}\frac{\partial \Phi}{\partial x_1}\right)=0,
\end{aligned}\tag{36}$$

$$\begin{aligned}
&\frac{\partial}{\partial x_3}\left(e_{113}\frac{\partial U_1}{\partial x_1}+e_{223}\frac{\partial U_2}{\partial x_2}\right)+\frac{\partial}{\partial x_2}\left(e_{322}\left(\frac{\partial U_2}{\partial x_3}+\frac{\partial U_3}{\partial x_2}\right)\right)+\frac{\partial}{\partial x_1}\left(e_{131}\left(\frac{\partial U_1}{\partial x_3}+\frac{\partial U_3}{\partial x_1}\right)\right)-\\
&-\frac{\partial}{\partial x_1}\left(\beta_{11}\frac{\partial \Phi}{\partial x_1}\right)-\frac{\partial}{\partial x_2}\left(\beta_{22}\frac{\partial \Phi}{\partial x_2}\right)-\frac{\partial}{\partial x_3}\left(\beta_{33}\frac{\partial \Phi}{\partial x_3}\right)=0.
\end{aligned}\tag{37}$$

Considering the $Case$ 1, the boundary conditions are: $U_1(x_1=-L/2)=0$, $U_2(x_2=-L/2)=0$, $U_3(x_3=-h/2)=0$, $\Phi(x_3=-h/2)=0$, $\Sigma_{11}(x_1=L/2)=0$, $\Sigma_{22}(x_2=L/2)=0$, $\Sigma_{33}(x_3=h/2)=-q$, $d_3(x_3=h/2)=0$.

The solution of this ODE problem takes the following form

$$\begin{aligned}
&U_1(x_1)=-q\,(2\,x_1+L)\,\Psi^{-1}\left[C_{1133}{e_{223}}^2-(C_{1122}e_{333}-C_{2233}e_{113})\,e_{223}-C_{1122}C_{2233}\beta_{33}+\right.\\
&\left.+C_{2222}\,(C_{1133}\beta_{33}+e_{113}e_{333})\right],\\
&U_2(x_2)=q\,(2\,x_2+L)\,\Psi^{-1}\left[-C_{2233}{e_{113}}^2+(C_{1,1112}e_{333}+C_{1133}e_{223})\,e_{113}+C_{1122}C_{1133}\beta_{33}-\right.\\
&\left.+C_{1111}\,(C_{2233}\beta_{33}+e_{223}e_{333})\right],\\
&U_3(x_3)=q\,(2\,x_3+h)\,\Psi^{-1}\left[-{C_{1122}}^2\beta_{33}-2\,C_{1122}e_{113}e_{223}+C_{2222}{e_{113}}^2+C_{1111}\left(C_{2222}\beta_{33}+{e_{223}}^2\right)\right],\\
&\Phi(x_3)=q\,(2\,x_3+h)\,\Psi^{-1}\left[{C_{1122}}^2e_{333}+(-C_{1133}e_{223}-C_{2233}e_{113})\,C_{1122}+C_{1133}C_{2222}e_{113}-\right.\\
&\left.+C_{1111}\,(C_{2222}e_{333}-C_{2233}e_{223})\right],
\end{aligned}\tag{38}$$

where the constant Ψ takes the form

$$\begin{aligned}\Psi = &- \big[2\, C_{3333}\beta_{33} + 2\, {e_{333}}^2\big)\, {C_{1122}}^2 + ((4\, C_{2233}\beta_{33} + 4\, e_{223}e_{333})\, C_{1133} + \\ &-4\, e_{113}\, (C_{2233}e_{333} - C_{3333}e_{223}))\, C_{1122} - 2\, \big(\, C_{2222}\beta_{33} +\, {e_{223}}^2\big)\, {C_{1133}}^2 + \\ &-\, 4\, e_{113}\, (C_{2222}e_{333} - C_{2233}e_{223})\, C_{1133} - 2\, \big(\, C_{1111}\beta_{33} +\, {e_{113}}^2\big)\, {C_{2233}}^2 - \\ &+\, 4\, C_{1111}C_{2233}e_{223}e_{333} + 2\, C_{2222}C_{3333}{e_{113}}^2 + \\ &+\, 2\, \big(C_{3333}{e_{223}}^2 + C_{2222}\, \big(C_{3333}\beta_{33} + {e_{333}}^2\big)\big]\, C_{1111}. \end{aligned} \tag{39}$$

The strain field and the electric field are consistently derived. The electric displacement field is identically zero, while the only non-vanishing component of the resulting stress field is $\Sigma_{33} = -q$.
Concerning, instead, the $Case$ 2, the new set of boundary conditions is $U_1(x_1 = \pm L/2) = 0$, $U_2(x_2 = \pm L/2) = 0$, $U_3(x_3 = -h/2) = 0$, $\Phi(x_3 = -h/2) = 0$, $\Sigma_{33}(x_3 = h/2) = -q$, $d_3(x_3 = h/2) = 0$. The corresponding solution of the ODE problem is

$$\begin{aligned} &U_1(x_1) = 0, \\ &U_2(x_2) = 0, \\ &U_3(x_3) = -\frac{q}{2}\, (2\, x_3 + h)\, \Xi^{-1}\beta_{33}, \\ &\Phi(x_3) = -\frac{q}{2}\, (2\, x_3 + h)\, \Xi^{-1}e_{333}, \end{aligned} \tag{40}$$

with the constant Ξ expressed in the form

$$\Xi = C_{3333}\beta_{33} + e_{333}^2. \tag{41}$$

The components of the electric displacement field are equal to zero, and the non-vanishing components of the stress field are

$$\begin{aligned} &\Sigma_{11}(x_1) = -q\Xi^{-1}\, (C_{1133}\, \beta_{33} + e_{113}\, e_{333})\, , \\ &\Sigma_{22}(x_2) = -q\Xi^{-1}\, (C_{2233}\, \beta_{33} + e_{223}\, e_{333})\, , \\ &\Sigma_{33}(x_3) = -q. \end{aligned} \tag{42}$$

The macroscopic fields, analytically determined, are compared against numerical results obtained with a micro-mechanical model. To this aim, a convergence study is performed considering clusters of increasing dimensions at the microscopic scale. This permits to detect the minimum size of the cluster such that the results related to the central cell remain almost unchanged. We observe that already for a cluster of 5 × 5 satisfactory results are obtained, so that the numerical results presented below are referred to this minimum size cluster geometry.

A first investigation is referred to the behaviour of the nanogenerators as the volume fraction of PANI nanoscopic particles varies within the matrix and the top and bottom layers, i.e. for dielectric permittivity $\varepsilon_r^{P/PANI}$ ranging from 5 to 10000. We, indeed, assume that the matrix and the layers are characterized by very high values of dielectric constants, varying with the volume fraction of PANI nanoscopic particles dispersed in the polymeric matrix. In Figure 4(a) the macroscopic dimensionless potential differences $\mathit{\Delta\Phi}\sqrt{\beta_{33}^{ZnO}}/(\sqrt{q}h)$ obtained from the heterogeneous model via up-scaling relations (solid plots) and from the equivalent homogenized model (dotted plots) are shown. Two densities are considered for both $Case$ 1 and $Case$ 2. In particular, blue and green curves refer to $Case$ 1 and $Case$ 2, respectively, considering a density δ=0.415, while red and black curves refer to $Case$ 1 and $Case$ 2, respectively, considering a density δ=0.104. We observe that the macroscopic analytical solutions are in very good agreement with the macroscopic numeric results obtained via up-scaling from the heterogeneous model. A non-linear trend is observed, with potential differences increasing as the the volume fraction of PANI decreases. Better performances are obtained for low values of $\varepsilon_r^{P/PANI}$. Note that the maximum values of potential differences are observed for the $Case$ 1 with lower density. For both the densities, the $Case$ 1 exhibits better performances.

A further investigation is devoted to study the influence of the height of the nanorods, considering the parameter $\alpha = h/h^*$, as the height h varies between 550 nm and 2200 nm, with h^*=1100 nm. An isotropic polymeric material doped with a highly conductive polymer (PANI), assuming the dimensionless dielectric constant $\varepsilon_r^{P/PANI} = \beta/\varepsilon_0$=5, is adopted for both the matrix and the top and bottom layers. In Figure 4(b) the macroscopic dimensionless potential differences $\mathit{\Delta\Phi}\sqrt{\beta_{33}^{ZnO}}/(\sqrt{q}h^*)$ are, thus, plotted versus α. Also in this plot, blue and green curves refer to $Case$ 1 and $Case$ 2, respectively, considering a density δ=0.415, while red and black curves refer to $Case$ 1 and $Case$ 2, respectively, considering a density δ=0.104. The solid lines refer to the solution of the micromechanical problems, while the dotted lines are the analytical solutions. Again, a nearly perfect match is observed. In this case, nearly linear variations are found as α varies. As expected, higher values of nanorods' heights are associated with better performances. Also in this case, the $Case$ 1 is more effective than $Case$ 2 irrespective of the considered density.

A more comprehensive investigation concerns the comparison between dimensionless potentials and dimensionless displacement components, evaluated along the top surface of the central Periodic Cell in the Cluster, adopting the heterogeneous model and the corresponding quantities derived from the first order homogenized model. In particular, we consider the $Case$ 2, δ=0.415 and $h = 1000$ nm, with both the matrix and the top and bottom layers made of PANI characterized by $\varepsilon_r^{P/PANI} = \beta/\varepsilon_0$=3. In Figure 5(a) the dimensionless macroscopic and microscopic electric potentials, $\mathit{\Phi}\sqrt{\beta_{33}^{ZnO}}/(\sqrt{q}h)$ and $\phi\sqrt{\beta_{33}^{ZnO}}/(\sqrt{q}h)$, respectively, evaluated along the top surface of the central Periodic Cell, are plotted, confirming the effectiveness of the homogenized model in predicting the averaged behaviour of the heterogeneous model. Finally, in Figure 5(b), both the dimensionless macroscopic and the microscopic displacement components,

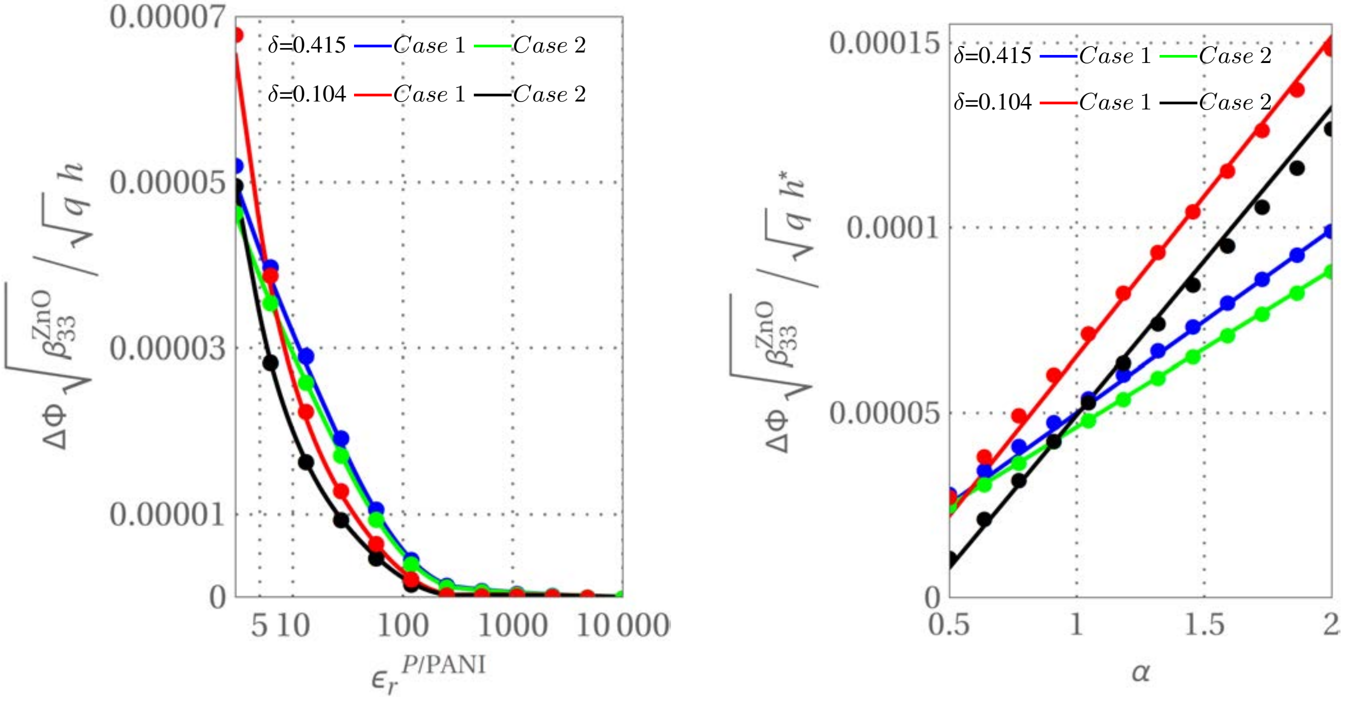

(a)

(b)

Fig. 4: Comparison of the macroscopic dimensionless potential differences obtained from the heterogeneous model via up-scaling relations (solid plots) and from the equivalent homogenized model (dotted plots). (a) Macroscopic dimensionless potential difference $\Delta\Phi\sqrt{\beta_{33}^{ZnO}}/(\sqrt{q}h)$ vs volume fraction of PANI. (b) Macroscopic dimensionless potential difference $\Delta\Phi\sqrt{\beta_{33}^{ZnO}}/(\sqrt{q}h^*)$ vs α, with h^*=1100 nm.

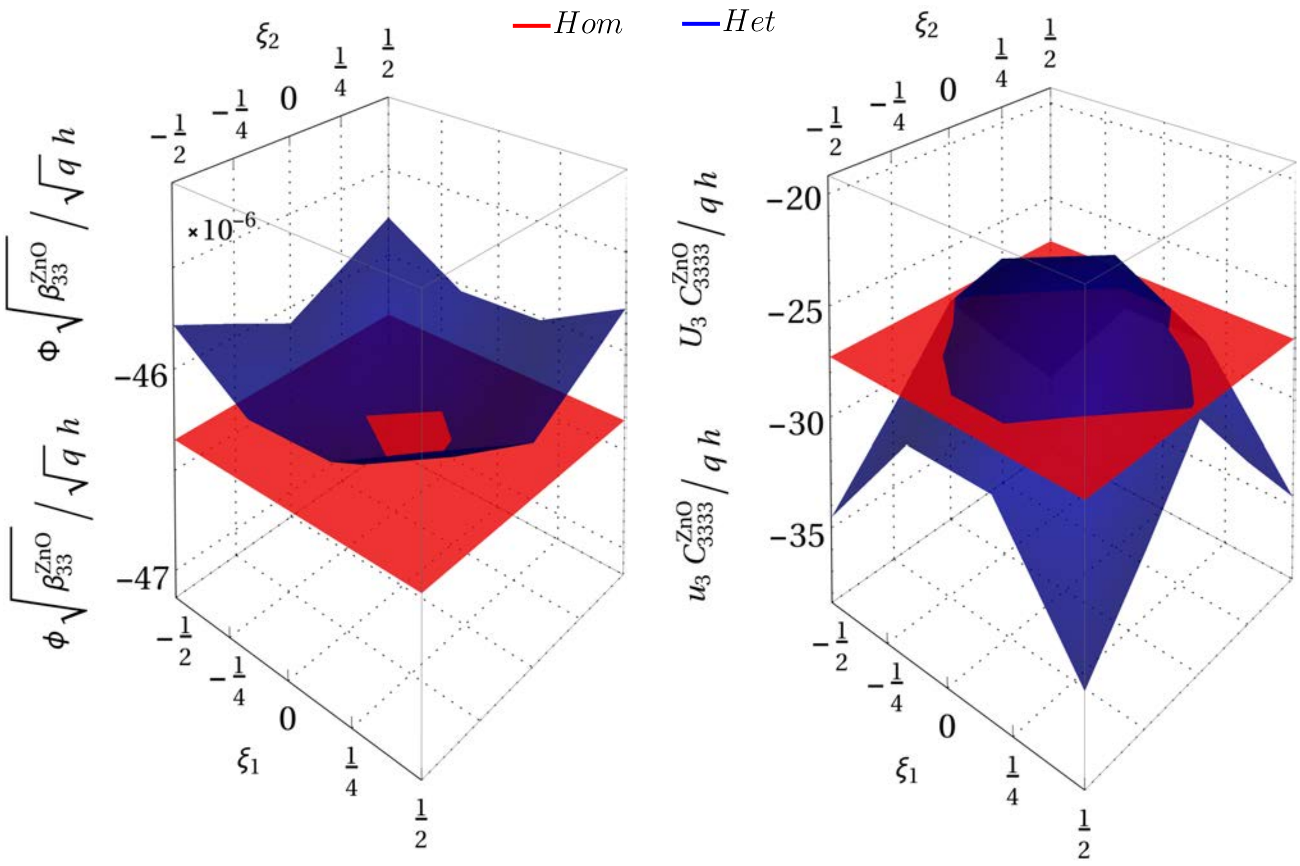

(a)

(b)

Fig. 5: Comparison between the heterogeneous model (Het) and the equivalent homogenized model (Hom) for the $Case$ 2, δ=0.415 and $h = 1100$ nm. (a) Dimensionless potentials of both the heterogeneous and the homogenized models. (b) Dimensionless displacement components of both the heterogeneous and the homogenized models.

$U_3 C^{ZnO}_{3333}/(qh)$ and $u_3 C^{ZnO}_{3333}/(qh)$, respectively, are compared with each other, again in good agreement. Furthermore, for the same case a further comparison between the heterogeneous model and the homogenized one is proposed. Focusing on the central cell of the Cluster, the local fields of both the dimensionless potential $\phi\sqrt{\beta^{ZnO}_{33}}/\sqrt{q}h$ (Figure 6(a)) and the dimensionless displacement $u_3 C^{ZnO}_{33}/qh$ (Figure 6(b)) are plotted in terms of ξ_1, ξ_2 and ξ_3. Specifically, the comparison between the micro-scale fields obtained from the equivalent homogeneous model via down-scaling relations (15), properly truncated, and those obtained from the heterogeneous model are proposed. A good agreement is observed from both the qualitative and quantitative point of view.

Second benchmark test

We are interested in comparing the results of the heterogeneous model with those of the first order equivalent homogeneous one, when the microstructured nanogenerator undergoes a different loading condition.

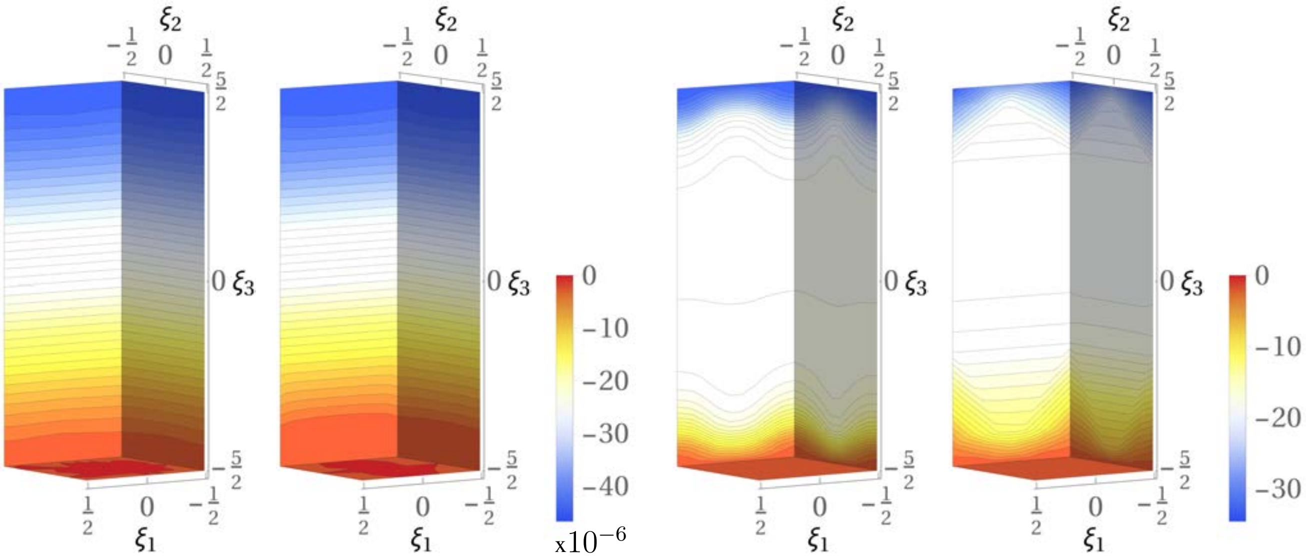

(a) (b)

Fig. 6: Comparison between the micro-scale fields obtained from the equivalent homogeneous model via down-scaling relations (figures (a) and (b) on the left) and the heterogeneous model (figures (a) and (b) on the right), respectively,for the $Case$ 2, δ=0.415 and h = 1100 nm. (a) Dimensionless potentials $\phi\sqrt{\beta_{33}^{ZnO}}/\sqrt{q}h$ of both models. (b) Dimensionless displacement $u_3C_{33}^{ZnO}/qh$ components of both models.

Flexible nanogenerators are, indeed, characterized by the ability to undergo bending deflections by exploiting the flexible substrates. For this reason, we consider a cluster of 5×15 cells (with base dimensions $L \times 3L$ and height h), for the case δ= 0.415 and h=1100 nm, and apply a bending by imposing opposite rigid rotations to the lateral faces (with normal parallel to x_2), around the axis x_1, that falls at half the height of the device, as schematically shown in Figure 7(a).The boundary conditions are characterized by longitudinal faces with restricted displacements in the x_1 direction. The electrodes are located along the top and bottom faces. In Figure 7(b) a good agreement is found between the heterogeneous model (blue curve) and the homogenized one (red curve) considering the dimensionless vertical displacement evaluated, along a longitudinal cut line characterized by x_1=0 and x_3=0. Also a zoomed view of the central cells is depicted. In Figure 7(c), the dimensionless potential is plotted for both the heterogeneous model (blue curve) and the homogenized one (red curve), along a vertical line with x_1=0 and x_2=$\frac{5}{2}L$. Again a satisfactory correspondence is found along the considered abscissa. Finally, in Figure 7(d) the dimensionless longitudinal displacement for both the heterogeneous (blue curve) and the homogeneous model (red curve) are plot along the same vertical line with x_1=0 and x_2=$\frac{5}{2}L$. In this case a nearly perfect match is observed.

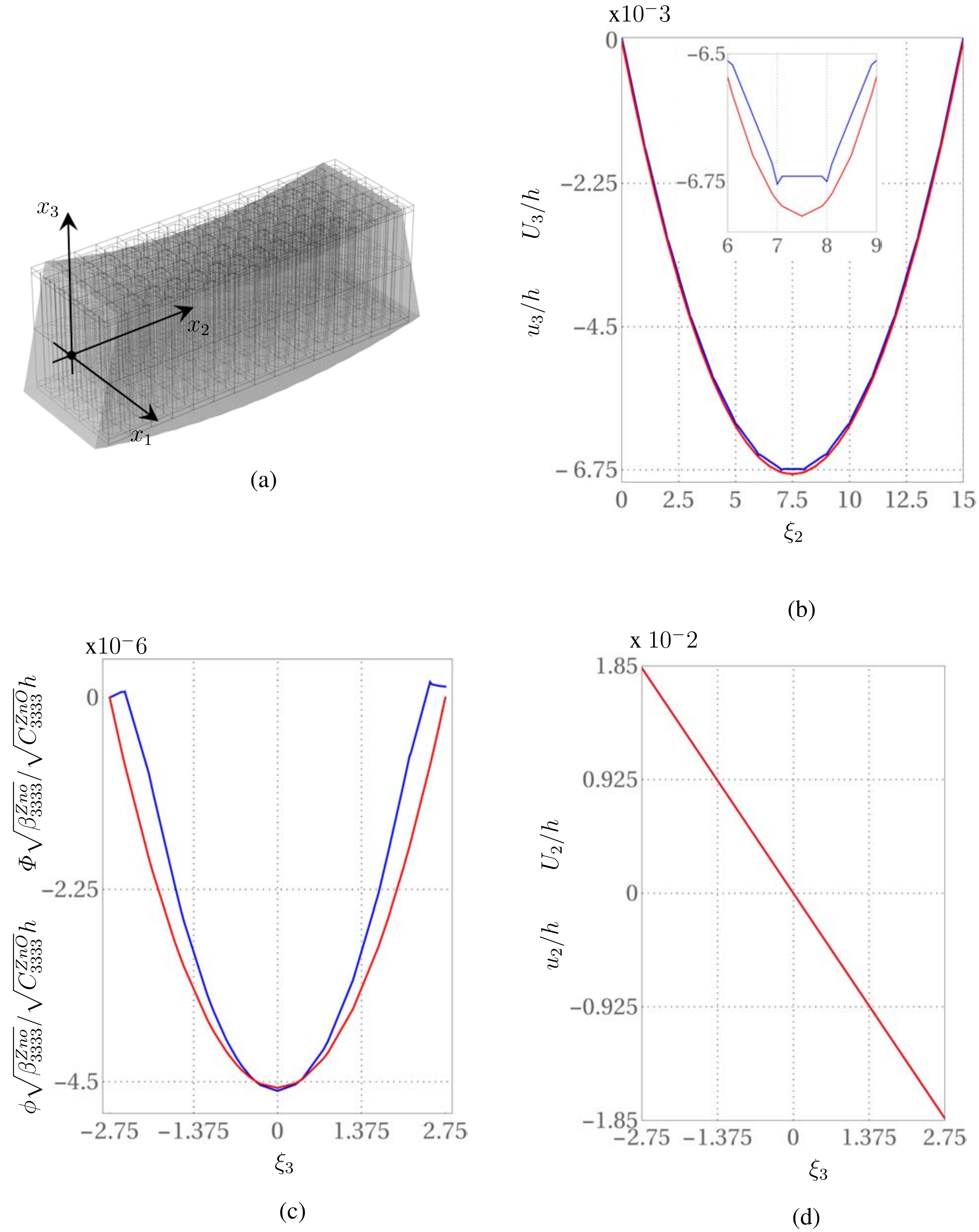

(a)

(b)

(c)

(d)

Fig. 7: Comparison between the heterogeneous model (blue curves) and the equivalent homogenized model (red curves) for the bending case, δ=0.415 and $h = 1100$ nm. (a) Schematic of the loading conditions applied to a cluster of 5×15 cells. (b) dimensionless vertical displacement components along a longitudinal cut line characterized by x_1=0 and x_3=0; (c) dimensionless potential along a vertical line with x_1=0 and x_2=$\frac{5}{2}L$; (d) dimensionless longitudinal displacement along a vertical line with x_1=0 and x_2=$\frac{5}{2}L$.

7 Applications of the asymptotic piezoelectric homogenization to microstructured nanogenerators

In this Section, the behaviour of three piezoelectric microstructured nanogenerators, with different working principles, is investigated as a set of geometrical parameters changes. Both extensional and bending nanogenerators are taken into account, considering either extension along the nanorods axis, or orthogonally to it. The influence of both the height of nanorods and their density on the overall behaviour of such devices is analysed. These geometric parameters can be, indeed, properly modified during the synthesis process of the ZnO-nanorods cluster, in order to tune the overall piezoelectric response and obtain improved performances, to possibly orient a final user towards optimal design choices.

In Subsection 7.1, microstructured extension nanogenerators are investigated. In this case, uniform mechanical loads act along the nanorods axis and the related potential differences are evaluated. Moreover, in Subsection 7.2, microstructured bending nanogenerators are analysed. The bending behaviour is induced by properly defined boundary conditions. Finally, in Subsection 7.3, microstructured transversal extension nanogerators are taken into account. The extension/contraction behaviour is due to the adoption of appropriate boundary conditions. In all the considered cases, the homogenized equivalent response of the device at hand is examined. Finite elements analyses have been performed adopting fully coupled tetrahedral second order elements with displacements and electric potential independent degrees of freedom. Note that we are particularly interested in determining the potential difference $\Delta\Phi$ measured between the top and bottom faces of the nanogenerator.

7.1 Microstructured extensional nanogenerators

We consider a microstructured device made of a cluster of 5×5 Periodic Cells, with base dimension L and height h. Electrodes are present on the upper and lower surfaces the device. The heterogeneous material is ideally replaced by a homogeneous equivalent piezoelectric first order continuum, obtained by exploiting the proposed asymptotic homogenization approach, see Figure 8 where a sketch is shown. Two loading conditions are alternatively taken into account, i.e. a uniform force distribution constant as L varies, and a uniform force distribution with the same resultant as L varies, both applied on the top horizontal face. Moreover, the multiscale analyses are performed assuming either free ($Case$ 1) or restrained ($Case$ 2) lateral vertical faces of the cluster, according to what proposed in the previous Section 6.2.

The initial investigation relates the influence of the nanorods density δ on the overall piezoelectric response of the devices. In Figure 9, a set of clusters made of 5×5 Periodic Cells, corresponding to various densities is reported.

We first consider the uniform surface load. In Figure 10, the overall response of the nanogenerators is reported in terms of averaged values, referred to the central Periodic Cell of the cluster, of the dimension-

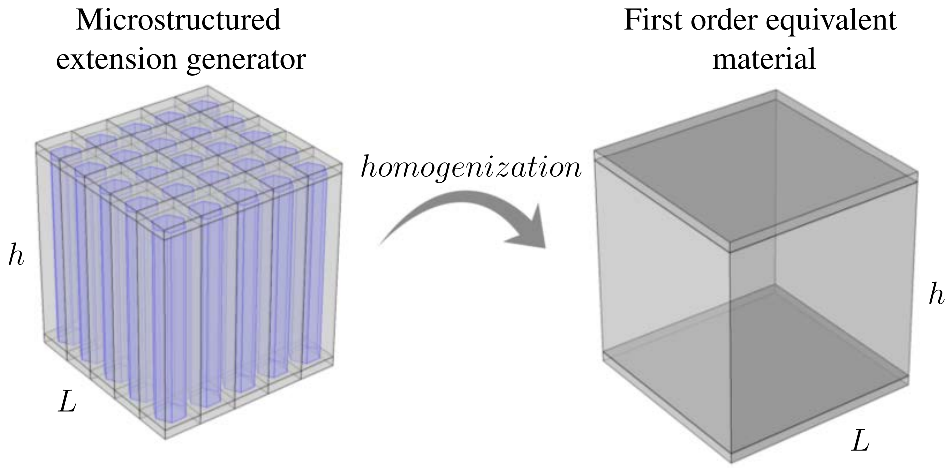

Fig. 8: Two-scales description of the extensional nanogenerator made by a cluster of 5×5 Periodic Cells.

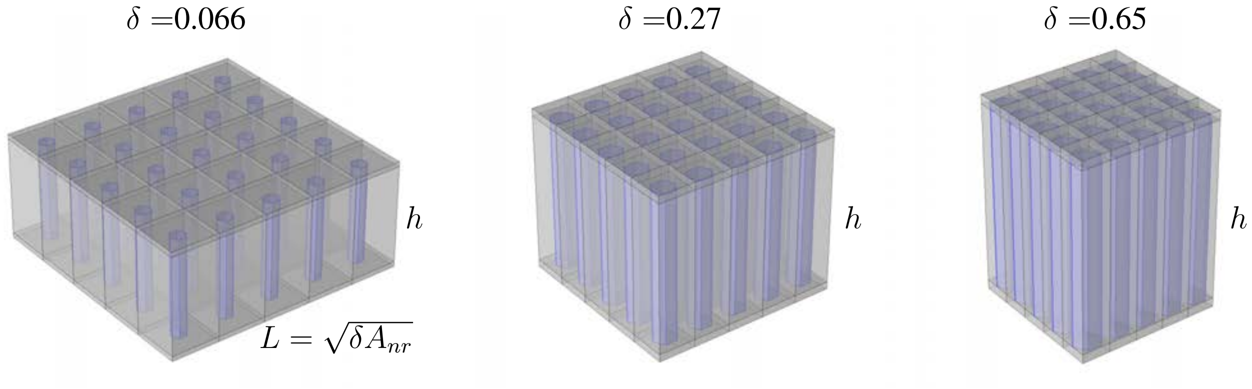

Fig. 9: Schematic of the extensional nanogenerator as the density δ varies, while the height of the ZnO nanorods is kept constant.

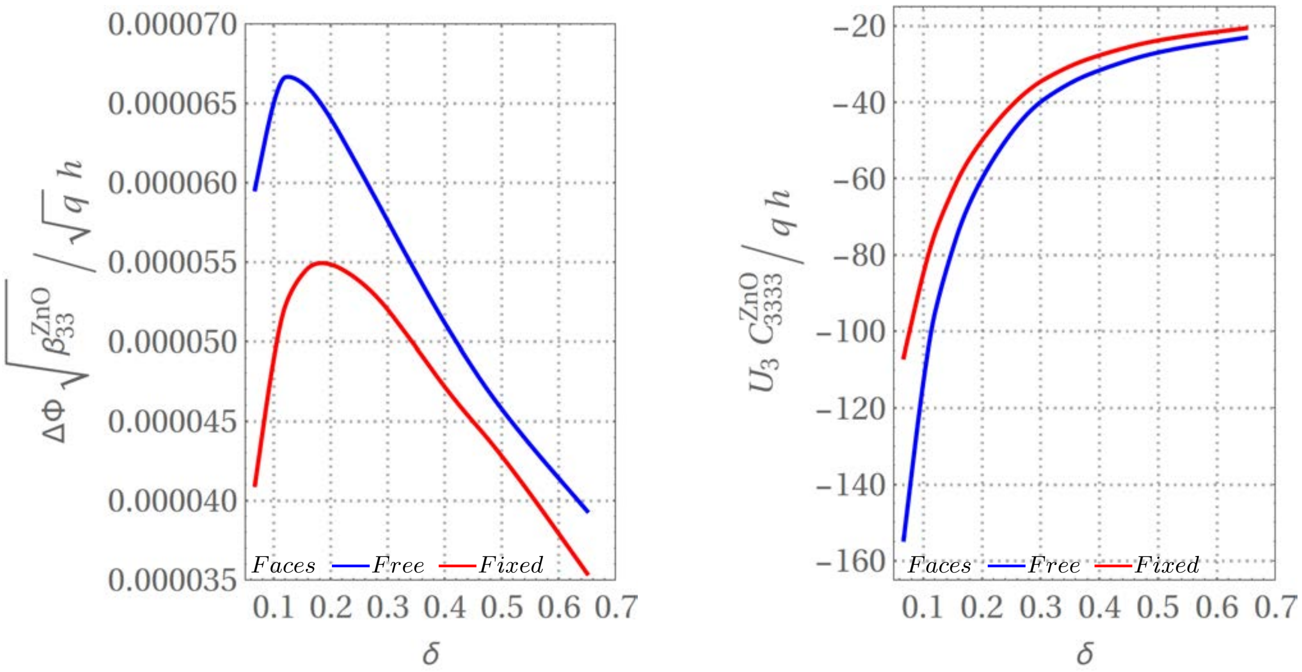

(a) (b)

Fig. 10: Uniform surface load. (a) Dimensionless potential difference vs δ. (b) Dimensionless displacement component vs δ.

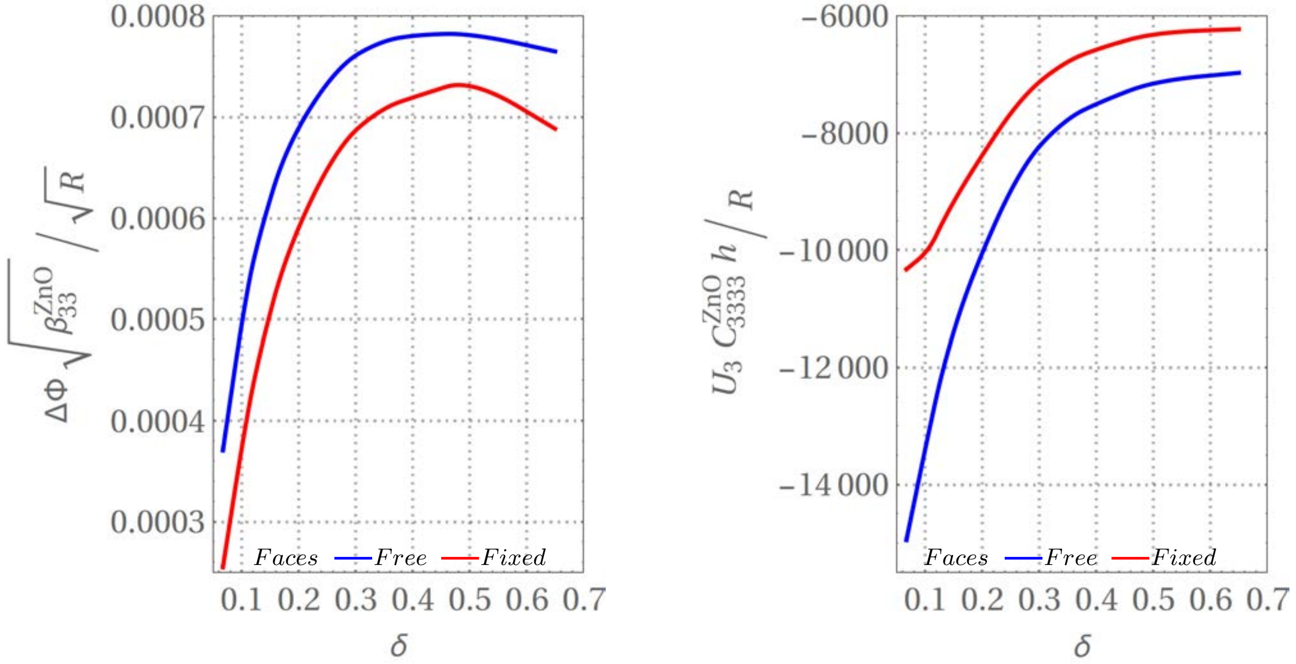

(a) (b)

Fig. 11: Surface load with constant resultant. (a) Dimensionless potential difference vs δ. (b) Dimensionless displacement component vs δ.

less potential difference and dimensionless vertical displacements versus δ. In particular, in Figure 10(a) the dimensionless values of $\Delta\Phi\sqrt{\beta_{33}^{ZnO}}/(\sqrt{q}h)$ where β_{33} is the 33 component of the permittivity matrix of the bulk Zinc Oxyde material, are shown versus the nanorods density. The blue curve refers to $Case$ 1, while the red curve to $Case$ 2. It is interesting to notice that the optimal behaviour that maximizes the potential difference of the device is achieved for different values of δ considering either $Case$ 1 or $Case$ 2. The maximum values of the curves correspond to small δ, in the range between 0.1 and 0.2. Moreover, in Figure 10(b) the dimensionless values of $U_3C_{3333}^{ZnO}/(qh)$, are shown as δ varies. As expected, the vertical displacements of the central cell increase as the density decreases. The sensor with free faces ($Case$ 1) is more flexible than the other. Similarly, the case where the resultant load is kept constant on clusters of variable densities is considered. In Figure 11, the overall response of the sensors in terms of averaged values, referred to the central cell, of the potential difference and the vertical displacements versus the nanorods density are plotted. In this case the normalization is performed considering the load resultant R. Referring to Figure 11(a), it is confirmed that the sensor with free faces (blue curve) is characterized by higher sensitivity (better performances). Nevertheless, the maximum of the curves is achieved for values of δ in the range between 0.4 and 0.5, that is shifted to the right with respect to the previous case. Also, considering the vertical displacements in Figure 11(b), again the blue curve (sensor with free lateral faces) is always below the red one.

Furthermore, the influence of the height h, directly related to the the nanorods length, is investigated.

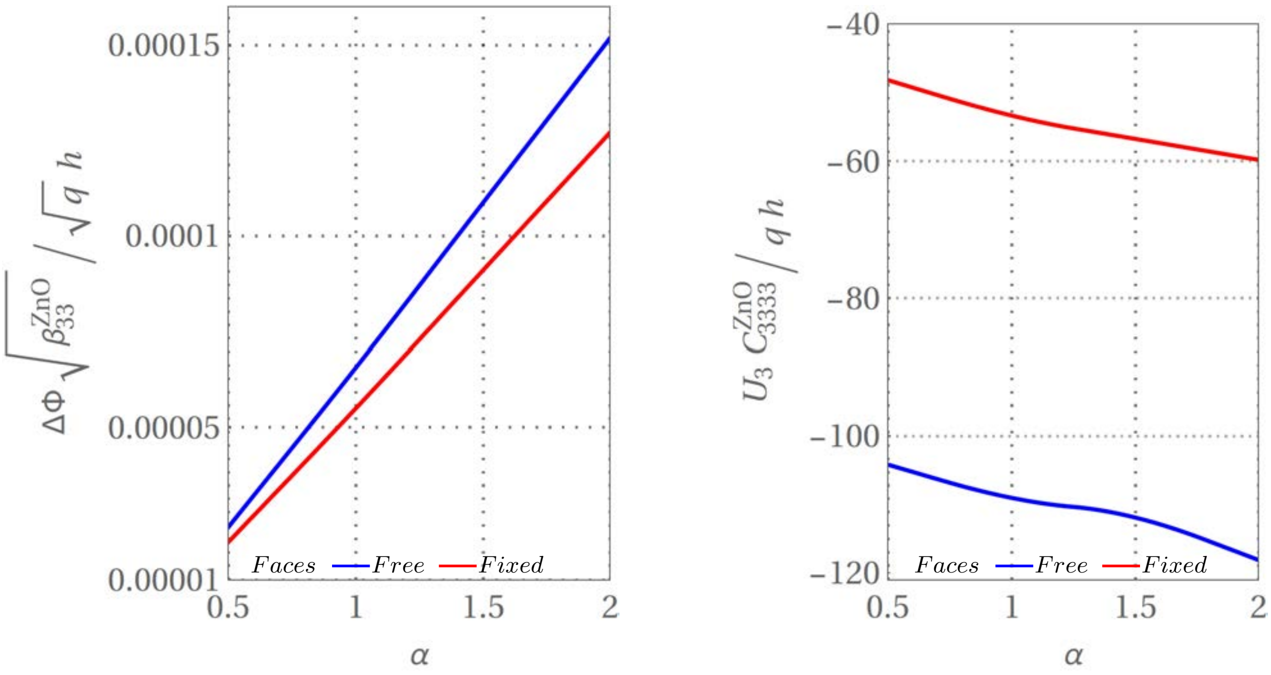

(a) (b)

Fig. 12: Uniform surface load. (a) Dimensionless potential difference vs α. (b) Dimensionless displacement component vs α.

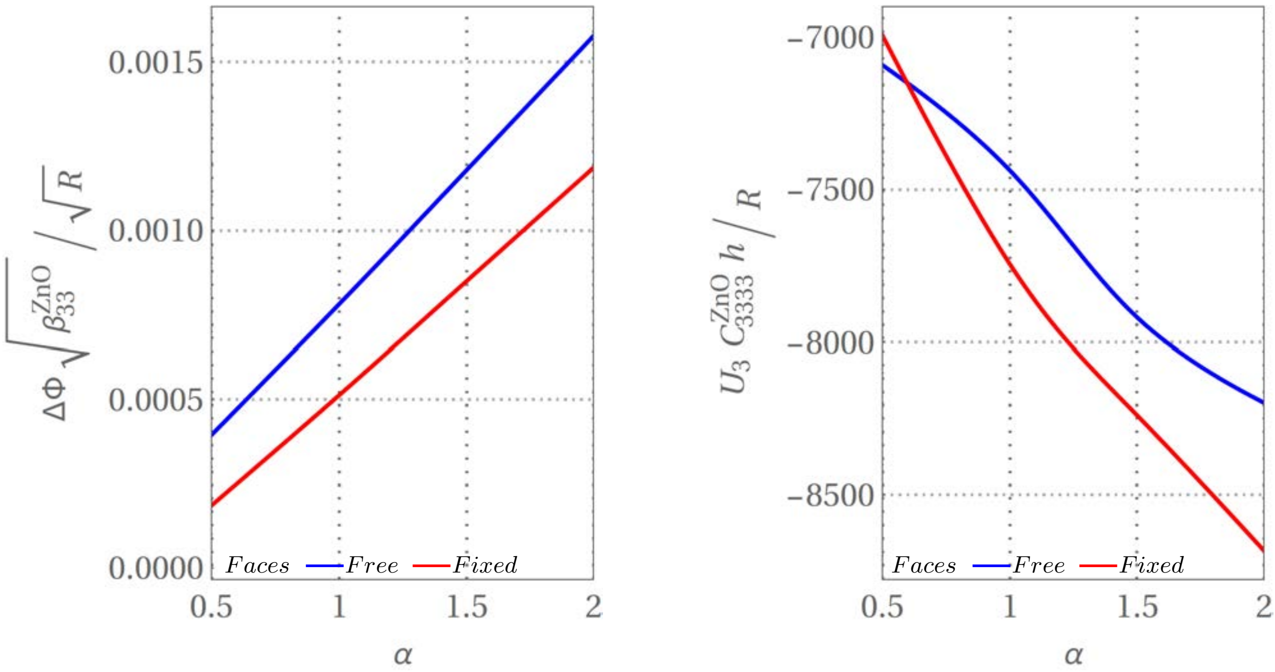

(a) (b)

Fig. 13: Surface load with constant resultant. (a) Dimensionless potential difference vs α. (b) Dimensionless displacement component vs α.

Considering again both the cases with uniform surface load, and load with fixed resultant, the response of the sensors for $Case$ 1 and $Case$ 2 is investigated. For each of the four analysed cases, the density δ that maximizes the corresponding responses in Figures 10(a) and 11(a) is taken into account. Starting with uniform surface load, in Figure 12 the response in terms of averaged values of the potential difference and the vertical displacements versus α are reported. The dimensionless value α is let varying between 0.5 and 2 and is equal to the ratio between the actual height of the device h and a reference value of h^*=1100 nm. As expected, a nearly linear variation of $\Delta\Phi\sqrt{\beta_{33}}/(\sqrt{q}h)$, as α varies, is found, see Figure 12 (a). In the case with free faces, blue curves, higher values of both potential difference and vertical displacements are observed. Finally, the results for the load with fixed resultant are shown in Figure 13. Again, a linear variation of the dimensionless potential difference versus α is found. On the other hand, concerning the vertical displacements, a nearly linear variation is observed. It is confirmed that the microstructured extension nanogenerators with free faces provide the better response in terms of potential difference, and are more flexible.

7.2 Microstructured bending nanogenerators

As already emphasized, a key point of the hybrid flexible nanogenerators is the possibility to exploit flexural mechanisms, related to the bending of the base support, to ensure energy harvesting. This peculiar behaviour is particularly emphasized in such innovative flexible devices, differently from what happen

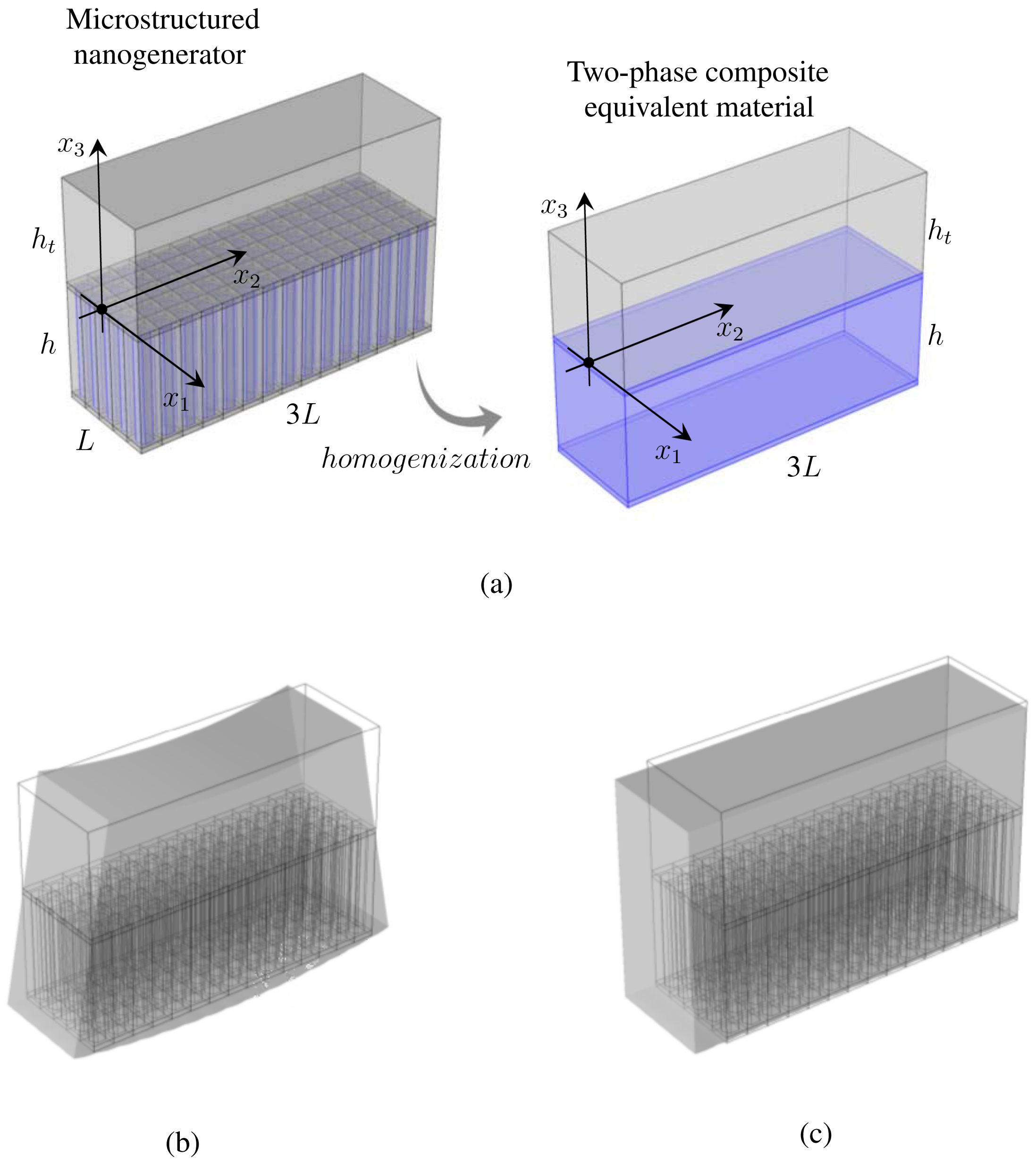

(a)

(b)

(c)

Fig. 14: Microstructured nanogenerators modeled at two scales. (a) Two-scales description of the microstructured nanogenerator made by a cluster of 15×5 Periodic Cells with a top polymeric layer of thickness h_t. (b) Qualitative deformed shape of the microstructured bender nanogenerator. (c) Qualitative deformed shape of the microstructured transverse extensional nanogenerator.

with standard ZnO-nanorods nanogenerator, provided with rigid supports, in which this behaviour is inhibited. Therefore, in this Section, the bending behaviour of such hybrid flexible nanogenerators is investigated and critically commented.

We consider devices made of a cluster of periodic cells topped by a further layer of electroactive polymeric material, see Figure 14(a) where a scheme of the microstructured nanogenerator is depicted. Adopting this particular geometry, we are interested in investigating how the thickness of the top layer influences the overall behaviour of the bending nanogenerator, inspired by the work by Opoku and co-authors, (Opoku et al., 2015). Two electrodes are located at the top and at the bottom faces of the microstructured device.

This problem is solved via a multi-scale approach, suitable to reduce high computational costs related to the adoption of micromechanical models. In particular, the cluster of periodic cells is preliminary homogenized into an equivalent piezoelectric first order continuum by exploiting the asymptotic homogenization approach. The resulting two-phase composite equivalent material is depicted in Figure 14(a), where the bottom layer is a homogeneous material characterized by overall piezoelectric constitutive tensors equivalent to periodic cells, and the top layer is a homogeneous electroactive polymer. The two-phase device is bent by applying opposite rigid rotations Θ to the lateral faces (with normal parallel to x_2), around the axis x_1, that falls at half the height of the device, see Figure 14(a). The qualitative deformed shape of this device is reported in Figure 14 (b). Again, two set of boundary conditions are considered. They are characterized either by free longitudinal faces (with normal parallel to x_1) or by longitudinal faces with restricted displacements in the x_1 direction. Hence, in this framework the potential Φ is only dependent on the x_3 axis, i.e. is uniform in x_1 and x_2, so that the potential difference, measured between two opposite points laying on the top and bottom faces (orthogonal to the x_3 axis), is constant.

A set of numerical analyses is proposed hereafter, where we consider the geometry of the device associated with a cluster of 15 $\times$ 5 periodic cells and adopting for the top layer the same polymeric material of the matrix, i.e. with Young modulus E= 535 MPa and Poisson's coefficient equal to ν=0.4. The relative permittivity is β=3.

In a first investigation we vary the thickness of the top layer h_t vary between 0 nm and 1100 nm (so that the maximum total height is h+h_t= 2200 nm). Considering a reference heterogeneous material with nanorods density δ=0.415, a rigid rotation $\Theta = 1/100$ radiants is applied. In Figure 15 the overall response of the nanogerators in terms of the potential difference and of displacement component U_3 (measured in the geometric center of the top face) versus h_t are reported. In Figure 15(a), the dimensionless potential difference $\Delta\Phi\sqrt{\beta_{33}^{ZnO}}/(\sqrt{C_{3333}^{ZnO}}(h+h_t))$ is plotted versus the thickness of the top layer h_t for both the cases with free (blue curve) and prescribed (red curve) lateral displacements. It clearly emerges that when h_t= 0 nm, no potential difference is measured, while as soon as the thickness h_t of the top layer is greater than zero, increasingly higher values are found. Better performances are experienced by the device with prescribed displacements. Concerning the dimensionless displacement component $U_3/(h+h_t)$ shown in

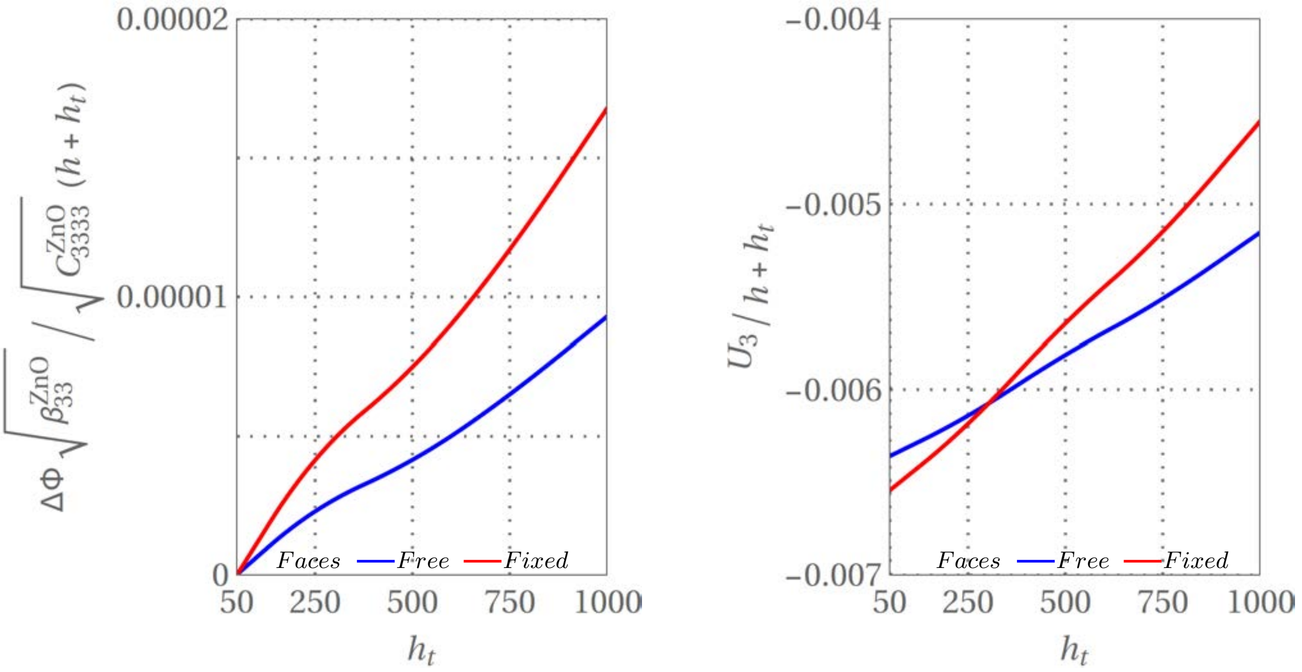

(a) (b)

Fig. 15: Bending nanogenerators obtained by homogenizing a cluster of 15 × 5 nanorods with δ=0.415. (a) Dimensionless potential difference vs h_t. (b) Dimensionless displacement component vs h_t.

Figure 15(b) versus h_t, nearly linear trends are observed. The red and blue curves intersect each other around h_t=300 nm, so that below this value the case with fixed longitudinal faces is more flexible than the other. Note that similar trends of both dimensionless $\varDelta\varPhi$ and u_3 are found for different values of δ referred to the corresponding heterogeneous material.

A principal outcome of this first study is that the nanogerator exhibits the best performances with maximum values of h_t. It follows that the second investigation concerns the analysis of bending nanogenerators with h_t=1100 nm as the density δ of the corresponding heterogeneous material varies. In Figure 16(a), the dimensionless potential difference is plotted versus the density δ. As before, blue curves refer to the case with free longitudinal faces, while and red curves refer to the case with displacements fixed. An interesting nonlinear behaviour is found, with the potential difference that increases with δ. Also in this case, better performances are provided by the device with prevented lateral displacements (red curve). A nonlinear response is also confirmed in the dimensionless displacement component $U_3/(h+h_t)$. The curves are nearly indistinguishable for low values of δ, while as $\delta > 0.2$ are increasingly far apart. Finally, it can be remarked that the bending nanogenerators show optimal behaviours when designed with very thick top layers, fixed lateral faces and high nanorods densities.

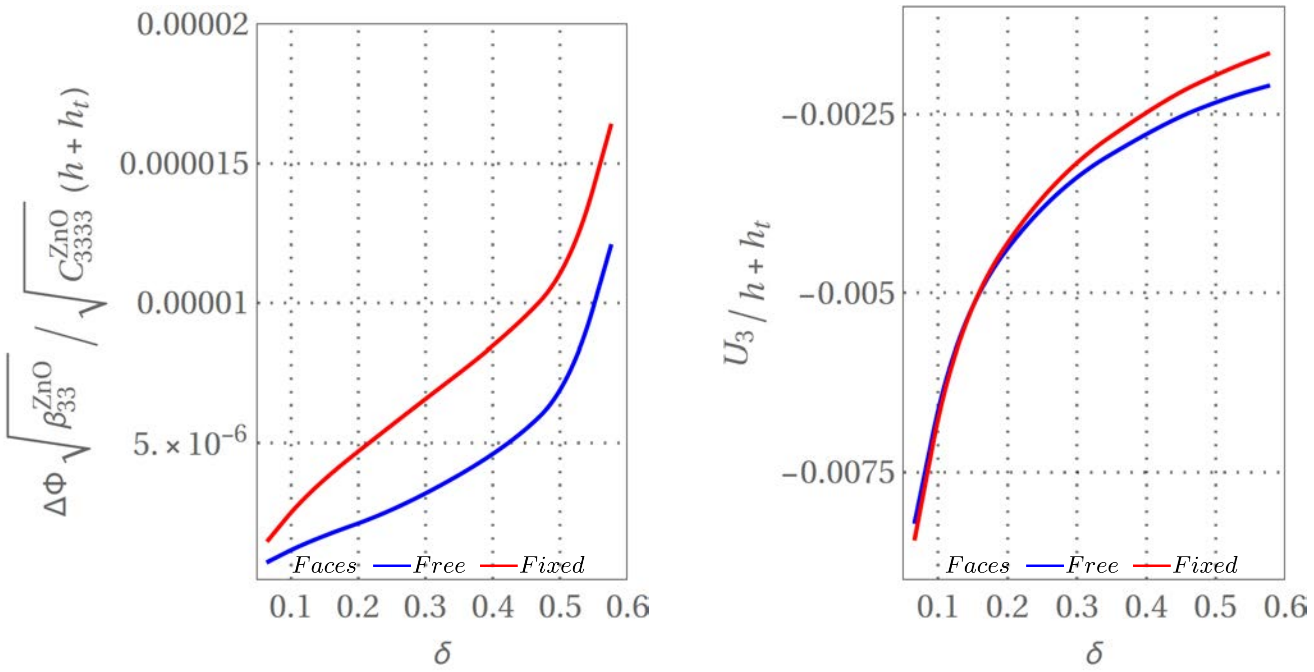

(a) (b)

Fig. 16: Bending nanogenerators obtained by homogenizing a cluster of 15 × 5 nanorods with h_t=1100 nm. (a) Dimensionless potential difference vs h_t. (b) Dimensionless displacement component vs h_t.

7.3 Microstructured transversal extension nanogenerators

The same devices analysed in Section 7.2, is here investigated adopting a different working principle related to transversal extension mechanism, see . Similarly to the previous case, the considered devices are made of a cluster of periodic cells topped with a polymeric layer of variable thickness. Again the multiscale approach is adopted to obtain a two-phase composite equivalent material, see Figure 14(a). The same geometries and materials as in Section 7.2 are taken into account. In this case, the two-phase device undergoes uniform opposite displacements along x_2 direction applied to the lateral faces (with normal parallel to x_2), inducing an overall extension ΔU_2= 10 nm of the nanogenerator. Moreover, the displacements of the points on the bottom face are restricted in the x_3 direction. The qualitative deformed shape of this device is reported in Figure 14 (c). We choose ΔU_2 so that it is comparable with the maximum displacement in the direction x_2 induced by the bending (when h_t=1100 nm) in the previous Section. Again, the displacement components along the x_1 direction of the longitudinal faces are alternatively free or set equal to zero.

Also in this case, first the influence of the thickness h_t of the top layer (for a fixed corresponding density δ=0.415) is investigated, and then the response as the corresponding density δ varies (for h_t=1100 nm) is studied. In Figure 17(a), the dimensionless potential difference versus the thickness of the top layer h_t is shown for both the cases with free longitudinal faces (blue curve) and restrained faces (red curve). As expected, nearly constant values of potential difference are found, irrespective of the thickness h_t.

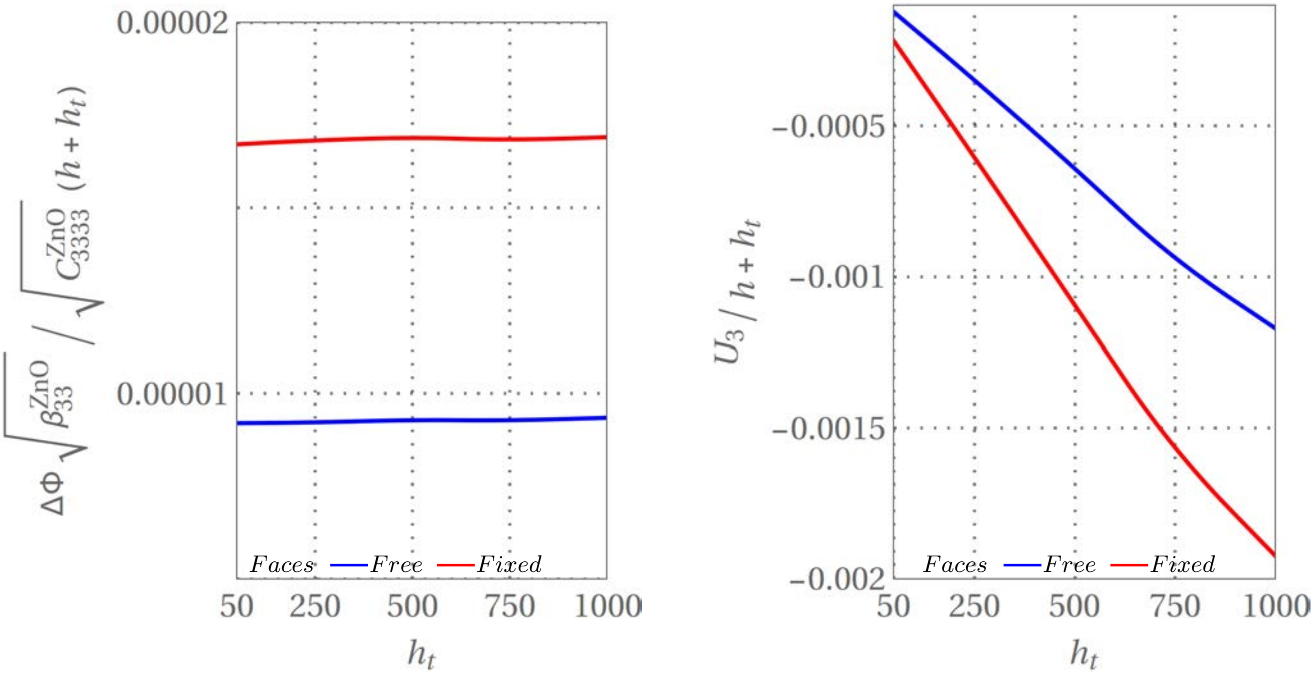

(a) (b)

Fig. 17: Transversal extension nanogenerators obtained by homogenizing a cluster of 15 × 5 nanorods with δ=0.415. (a) Dimensionless potential difference vs h_t. (b) Dimensionless displacement component vs h_t.

Moreover, the case with fixed longitudinal faces provides higher potential differences. On the other hand, concerning the vertical displacement U_3, pseudo-linear variations are observed as h_t varies.

Finally, for the case with h_t=1100 nm, the dimensionless potential difference is shown in Figure 18(a), while the dimensionless displacement components $U_3/(h+h_t)$, of the points laying on the top face, is plotted in Figure 18(b)) versus the corresponding density δ of the heterogeneous ZnO based hybrid nanogenerator. The plots of the potential difference with δ are almost overlapping with those in Figure 16(a). It is, nevertheless, noted that a qualitative different distribution of the macroscopic electric potential $\varPhi$ along the height $(h+h_t)$ of the specimen is observed in the case of bending nanogenerators and transversal extension nanogenerators. In particular, both a nonlinear and a linear monotonic trends are observed along the height of the bottom homogenized layer, in the former and the latter cases, respectively. Moreover, in both cases a nearly constant value is maintained within the polymeric top layer. Concerning the U_3 displacement components, as expected, significantly lower values are found (one order of magnitude lower) with respect to the Figure 16(b). It is noteworthy that in the case of combined effects of bending and transversal extension, optimal performances of the device are obtained by combining positive rigid rotations and extension, as qualitatively shown in Figures 14(b) and 14(c).

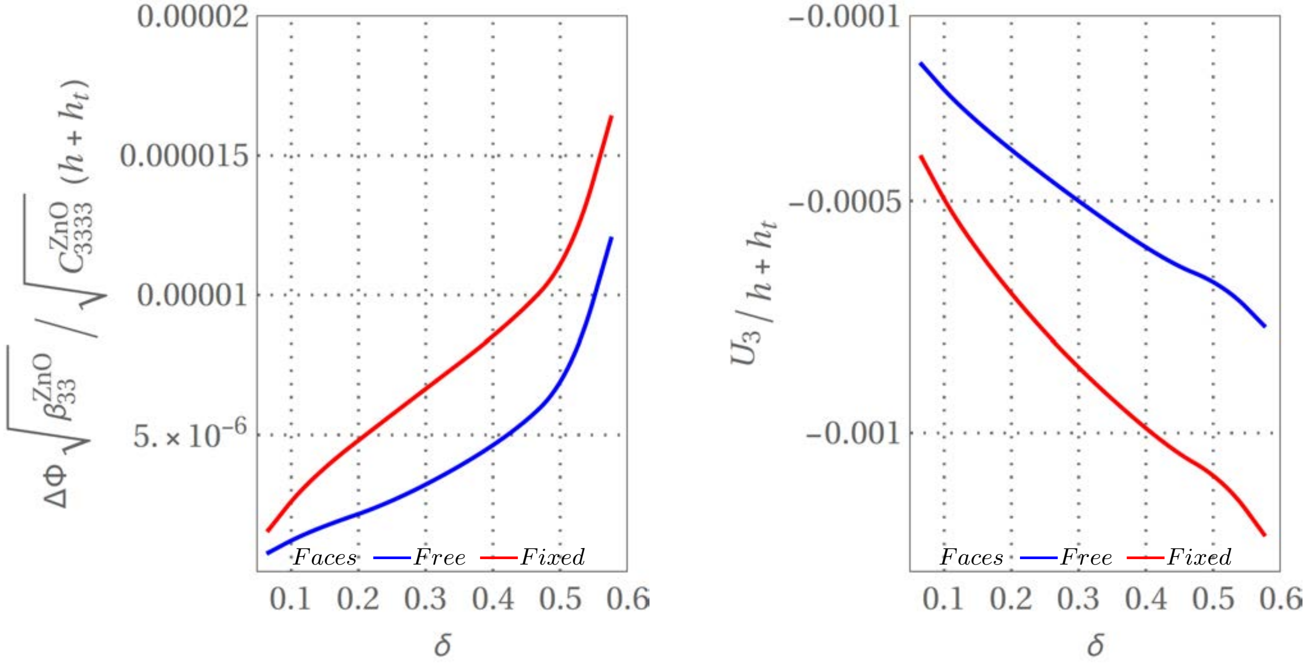

(a) (b)

Fig. 18: Transversal extension nanogenerators obtained by homogenizing a cluster of 15 × 5 nanorods with h_t=1050 nm. (a) Dimensionless potential difference vs δ. (b) Dimensionless displacement component vs δ.

8 Bloch waves in piezoelectric nanogenerators

This Section is devoted to investigate the dynamic characterization of the piezoelectric periodic nanostructured material for the purpose of analysing the Bloch waves propagation. In particular, the frequency spectrum of the heterogeneous material is obtained for different unit vectors of propagation. Moreover the acoustic branches of such frequency spectrum are compared against the dispersion functions obtained by the homogenized model.

Different Periodic Cells $\mathfrak{A} = [-d/2, d/2] \times [-d/2, d/2] \times [-h/2, h/2]$ of the microstructured nanogenerators are considered (see Figure 2(a)). They are characterized by various nanorods densities δ. The ZnO-nanorod has hexagonal section with edge 80 nm, while the height in the polarization direction is h= 1100 nm. The ZnO nanorod is embedded within a polymeric matrix (E=535 MPa, ν=0.4 and β=3). The same polymeric material is adopted for the top and bottom layers. The mass density of the nanorod is ρ^{ZnO}= 5680 kg/m^3, while the mass density of the polymeric material is set equal to ρ= 1500 kg/m^3. In this framework, the Periodic Cell $\mathfrak{A}$ is associated with the dimensionless first Brillouin zone $\mathfrak{B} = [-\pi, \pi] \times [-\pi, \pi] \times [-\pi, \pi]$, defined in the space of the dimensionless wave vectors (whose components are $k_1 d$, $k_2 d$ and $k_3 h$). Such Brillouin zone is characterized by three orthogonal vectors $\pi \mathbf{n}_i$, parallel to $\mathbf{e}_i$, with i=1,2,3.

The influence of the nanorods density δ on the Floquet-Bloch spectrum, as the unit vector of propaga-

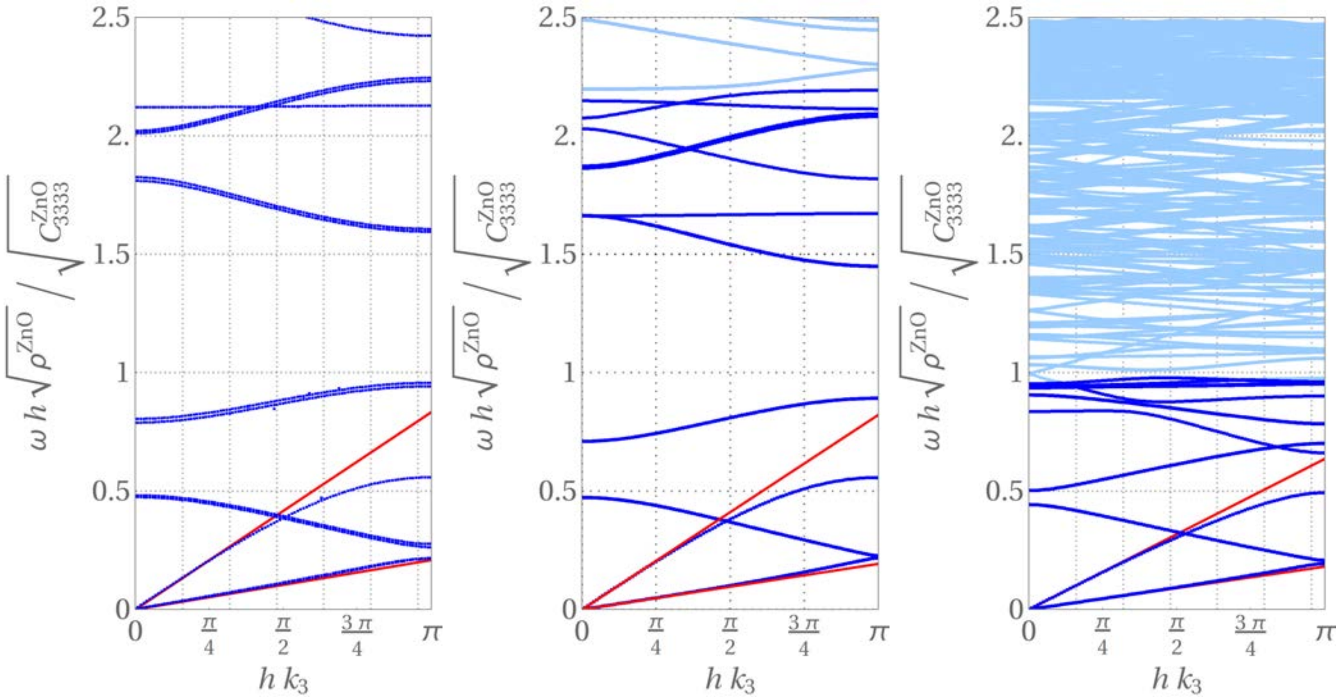

(a) (b) (c)

Fig. 19: Floquet-Bloch spectra for unit vector of propagation $\mathbf{n}_3$ and different densities δ of the piezoelectric composite material. The dimensionless angular frequency is plotted versus the dimensionless wave number. (a) δ=0.57. (b) δ=0.415. (c) δ=0.10.

tion **n** varies, is thus analysed. Main attention is devoted to identifying the existence, the position and the frequency range of full or partial band gaps in the microstructured piezoelectric material. Note that in this case of nanogenerators, the Floquet-Bloch spectrum analysis is particularly relevant in view of providing design guidelines. Such devices are, indeed, intended to operate under dynamical loadings that can trigger the electrical energy production. A detailed investigation concerning the band gaps is very useful to identify possible frequency ranges in which the device behaves as a filter. It is, thus, clear that a dynamical loading is supposed to be characterized by frequencies falling outside frequency band gaps, in order to be effective.

The values of the dimensionless angular frequency $\omega\, h\sqrt{\rho^{ZnO}}/\sqrt{C_{3333}^{ZnO}}$, against the dimensionless wave number $k_3 h$, related to the unit vector of propagation $\mathbf{n}_3$ parallel to $\mathbf{e}_3$, are shown in Figure 19 for three densities δ equal to 0.57, 0.415 and 0.10, respectively. The piezoelectric nanogenerator exhibits a high spectral density for all the densities. The first 15 branches of the spectrum are plotted in dark blue, while the other ones in light blue. In particular, in Figure 19(a) the Floquet-Bloch spectrum for density δ=0.57 is plotted. Only ten curves are visible, since multiple roots are found by virtue of material symmetry characterizing the Periodic Cell. As expected, three acoustic branches departs from zero angular frequency (in the Figure only two are distinguishable, since two of them are coincident). The remaining 8 curves are the optical branches. The Floquet-Bloch spectrum exhibits one point of crossing between acoustic and optical branches and also a point of crossing between different optical branches. Four partial band gaps are detected. In Figure 19(b), instead, the Floquet-Bloch spectrum for the material with density δ= 0.415 is plotted. The spectrum is qualitatively similar to the previous one, in Figure 19(a). The first three acoustic branches and the first two optical branches (two coincident curves) are very similar to the corresponding ones for δ=0.57. On the other hand, all the remaining branches are pulled down, resulting in curves closer together (more dense spectrum) and partial band gaps basically characterized by lower amplitudes. As a consequence, the relative position of the band gaps is shifted towards lower frequencies. Moreover, in Figure 19(c) the Floquet-Bloch spectrum for the material with density δ=0.1 is shown. The same trend of Figure 19(b) is confirmed and emphasized. Again the first three acoustic branches and the first two optical branches remain almost unchanged, but all the others are shifted towards smaller angular frequencies. A very dense spectrum is observed. This analysis suggests that, by focusing on a given frequency interval, for instance $0 < \omega\, h\sqrt{\rho^{ZnO}}/\sqrt{C_{3333}^{ZnO}} < 1$, as the density δ decreases, the microstructured piezoelectric device exhibits better performances, since the spectrum is more dense. A considerably broader passband width is, indeed, found. The acoustic branches of the Floquet-Bloch spectrum that characterize the heterogeneous material are compared against the dispersion curves obtained adopting the first order homogenization theory (red curves in Figure 19). A good agreement is found, confirming the capability of the first order homogenization theory to satisfactorily reproducing the lowest (acoustic) branches of the Bloch spectrum for a wide range of wavelengths. As expected, the model at the first order only describes non-dispersive waves exhibiting a linear dependence between the angular frequency and the wave-number.

A further investigation concerns the Floquet-Bloch spectrum for waves characterized by unit vector of propagation $\mathbf{n}_3$, studying the influence of the height of the nanorods, considering the parameter $\alpha = h/h^*$, as the height h varies with h^*=1100 nm. A density δ=0.415 is considered. In this case, the dimensionless angular frequency, against the dimensionless wave number, are shown in Figure 20 for three heights h equal to 550 nm, 1650 nm and 2200 nm, respectively. The first 15 branches of the spectrum are plotted in dark blue, while the others are plotted in light blue. It is remarked that, in the considered frequency range, the spectral density tends to increase as the height h increases. In Figure 20(a), the case with h=0.5 h^* is taken into account. A wide partial band gap is found with central dimensionless frequency around 1.2, while a second partial band gap is characterized by lower amplitude and higher central angular frequency. Again, various crossing points are observed. Figures 20(b), and 20(c) shows the cases with h=1.5 h^* and h=2 h^*, respectively. As the height increases, a higher number of partial band gaps, characterized by lower frequencies, are observed. The acoustic and optical branches tend to be shifted towards lower angular frequencies. Also in this case, the red curves represent the acoustic branches of the Floquet-Bloch spectrum obtained via a first order homogenization approach. Such linear dispersion functions are in good agreement with the the lowest (acoustic) branches of the Bloch spectrum, charac-

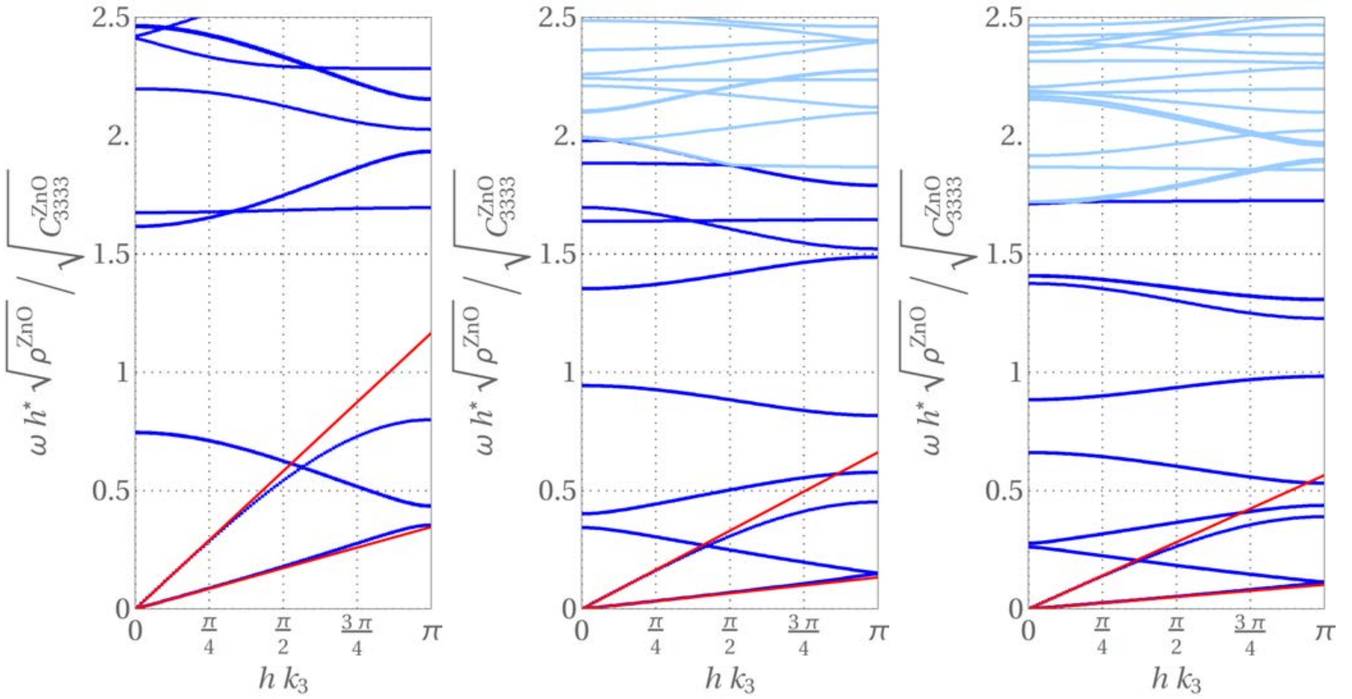

(a) (b) (c)

Fig. 20: Floquet-Bloch spectra for unit vector of propagation $\mathbf{n}_3$ for different ratios between the height h of the ZnO nanorod and the reference height h^*=1100 nm. The dimensionless angular frequency is plotted versus versus the dimensionless wave number. (a) h=0.5 h^*. (b) h=1.5 h^*. (c) h=2 h^*.

terizing the heterogeneous material, for a wide range of wavelengths.

A similar investigation, concerning both the influence of the density δ and of the height h, is performed considering the unit vector of propagation $\mathbf{n}_1$ parallel to $\mathbf{e}_1$. Also in this case, the first 15 branches of the spectrum are plotted in dark blue, while the others are plotted in light blue. In Figure 21, three densities δ equal to 0.57, 0.415 and 0.10, respectively, are taken into account. Very dense spectra are here observed, where no partial band gaps are detected irrespective of the considered density. It is confirmed that the spectrum density increases as the density δ decreases. Focusing on Figure 21(a), various crossing points and a veering point (with dimensionless frequency about 2) are found. Three distinct acoustic branches are observed, well approximated by the dispersion functions (red linear curves) obtained by the first order piezoelectric continuum. It is, moreover, noted that the first two acoustic branches tend to overlap each other as the density δ decreases. It is noteworthy that in the long wave regime the phase and group velocity, associated with the acoustic branches, tend to decrease as the density δ decreases.

Analogous considerations are valid for the Figure 22, in which the dimensionless angular frequency, against the dimensionless wave number $k_1 d$, are shown, for three heights h equal to 550 nm, 1650 nm and 2200 nm, respectively, adopting δ=0.415. Also in this case, indeed, no partial band gaps are detected, and the spectrum density increases as the height h increases. Various crossing and points are found.

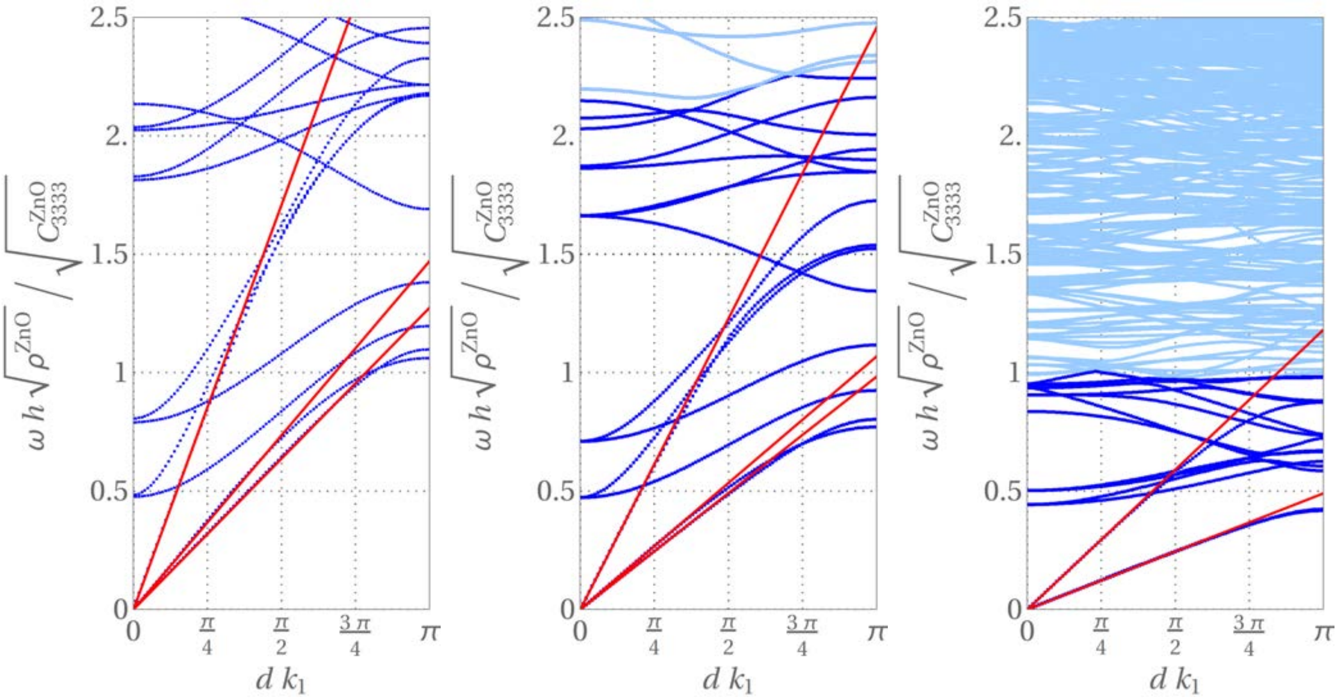

(a) (b) (c)

Fig. 21: Floquet-Bloch spectra for unit vector of propagation $\mathbf{n}_1$ and different densities δ of the piezoelectric composite material. The dimensionless angular frequency is plotted versus versus the dimensionless wave number $k_1 d$. (a) δ=0.57. (b) δ=0.415. (c) δ=0.1.

Finally, three distinct acoustic branches are observed, well approximated by the red linear curves, representing the dispersion functions of a first order homogeneous equivalent continuum.

A more comprehensive description of the acoustic characteristics of the piezoelectric nanoscopic material is given by the dispersion surfaces in the Brillouin zone, representing the dimensionless angular frequency $\omega\, h\sqrt{\rho^{ZnO}}/\sqrt{C^{ZnO}_{3333}}$ of waves characterized by unit vector of propagation $\mathbf{n}$=cos $\theta\, \mathbf{n}_1$+sin $\theta\, \mathbf{n}_2$, with $0 \leq \theta \leq \pi/2$. In Figure 23(a), an axonometric view is show for the case with density δ= 0.415. In the domain of considered wave vectors, a high spectral density is observed, since the acoustic surfaces intersect the first optical ones and, moreover, the optical surfaces at higher frequencies intersect each other over and over. One partial band gap is detected between the eight and ninth surfaces.

In particular, in Figure 23(a) a zoomed view of the surfaces defining the partial band gap is shown. As a consequence, in this range the propagation of waves characterized by $k_3 = 0$ is inhibited.

As a final investigation, it is interesting to evaluate the velocity c of Bloch waves propagating in the long wavelength regime. To this aim, it is required to solve the eigenvalue problem in (33) in terms of the constants of the overall constitutive tensors of the first order homogenized continuum. In particular, we refer to a specific example, considering ZnO-nanorods, embedded within a polymeric matrix (E=535 MPa, ν=0.4 and β=3), characterized by density δ=0.415. The same polymeric material is adopted for the top

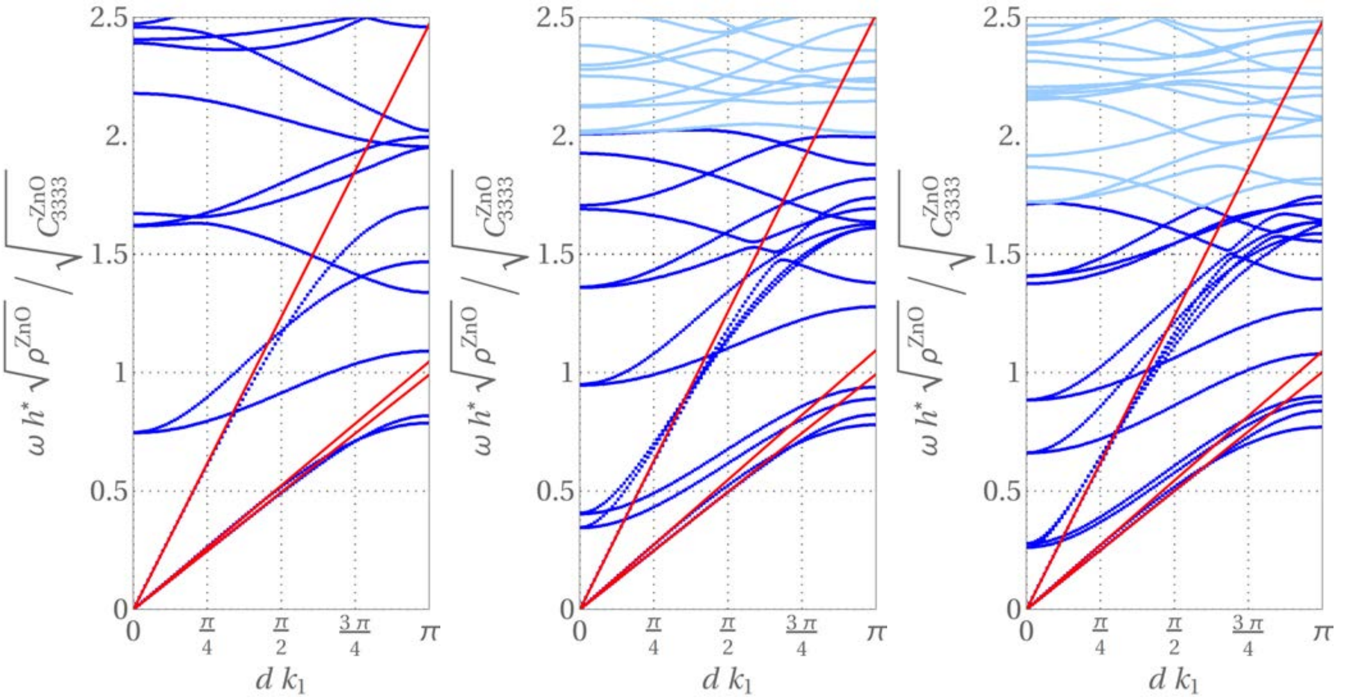

(a) (b) (c)

Fig. 22: Floquet-Bloch spectra for unit vector of propagation $\mathbf{n}_1$ for different ratios between the height h of the ZnO nanorod and the reference height h^*=1100 nm. The dimensionless angular frequency is plotted versus versus the dimensionless wave number $k_1 d$. (a) h=0.5 h^*. (b) h=1.5 h^*. (c) h=2 h^*.

and bottom layers and the height of the Periodic Cell h=1100 nm. In Figure 24 the dimensionless values of the wave velocities $c^{(i)}\sqrt{\rho^{ZnO}}/\sqrt{C_{3333}^{ZnO}}$ are plotted in terms of the angular variables θ and ϕ representing the components of the unit vector of propagation $\mathbf{n}$, i.e. n_1=sinθ cos ϕ, n_2=sinθ sinϕ, n_3=cosθ. In Figure 24(a) the three surfaces referred to the velocities $c^{(1)}$, $c^{(2)}$ and $c^{(3)}$ are plotted against θ and ϕ. In Figure 24(b) the polar plot of $c^{(1)}$, $c^{(2)}$ and $c^{(3)}$ for a fixed value of ϕ=0 is plotted as θ varies, while Figures 24(c) and (d) report the polar plot of $c^{(1)}$, $c^{(2)}$ and $c^{(3)}$ as ϕ varies for θ=$\pi/2$ and θ=$\pi/4$, respectively.

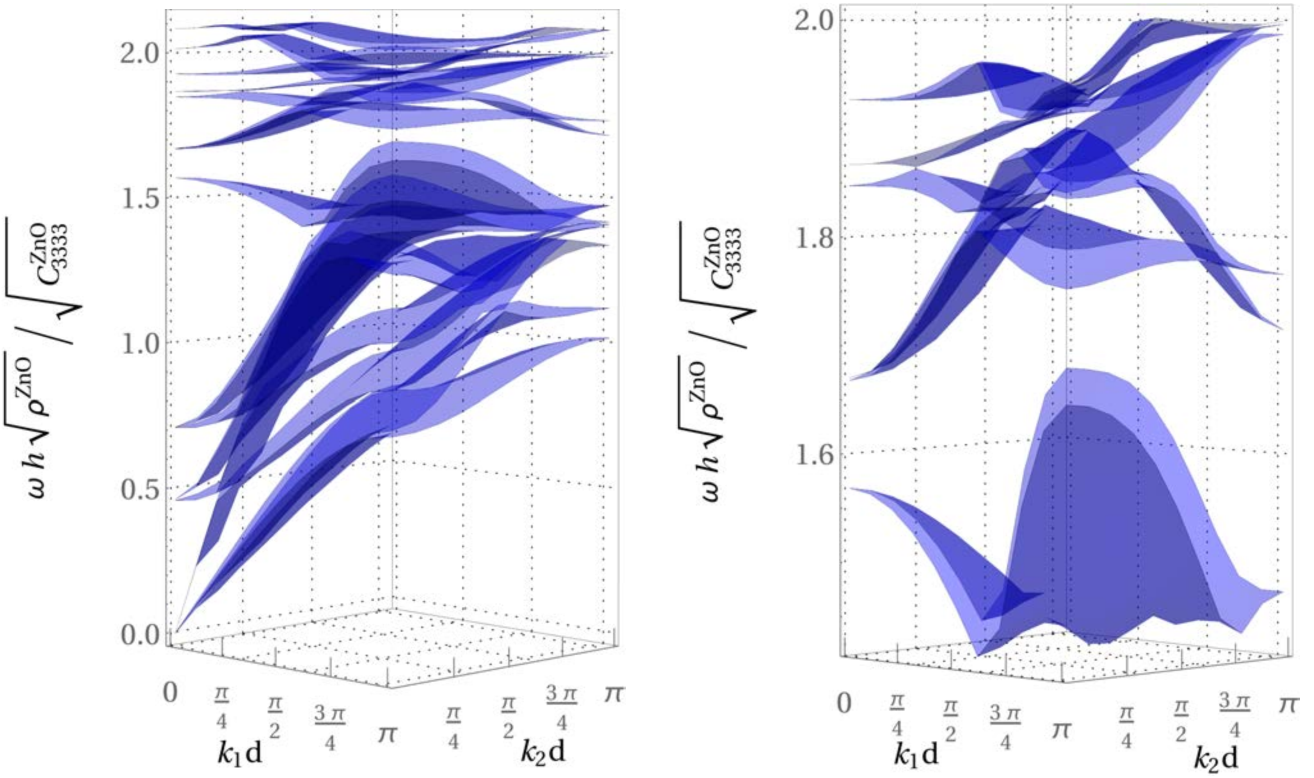

(a)

(b)

Fig. 23: Axonometric view of the Floquet-Bloch spectra for unit vector of propagation **n** laying on the plane with normal $\mathbf{n}_3$. (a) First 15 surfaces. (b) zoomed view of the partial band gap.

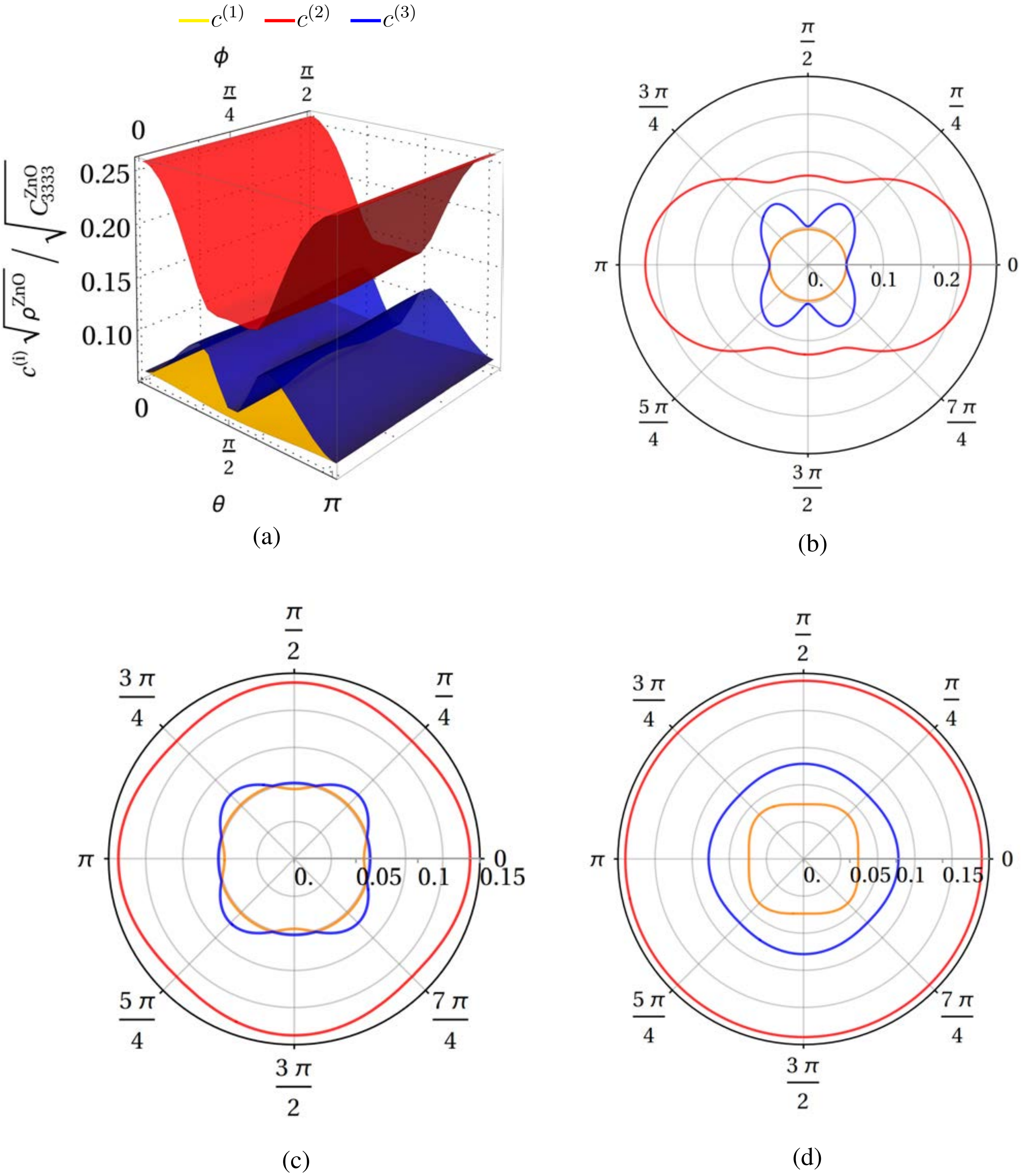

Fig. 24: Velocity of Bloch waves propagating in the long wavelength regime. (a) Surfaces of the velocities $c^{(1)}$, $c^{(2)}$ and $c^{(3)}$ versus θ and ϕ; (b) polar plot of $c^{(1)}$, $c^{(2)}$ and $c^{(3)}$ versus θ for ϕ=0; (c) polar plot of $c^{(1)}$, $c^{(2)}$ and $c^{(3)}$ versus ϕ for θ=$\pi/2$; (d) polar plot of $c^{(1)}$, $c^{(2)}$ and $c^{(3)}$ versus ϕ for θ=$\pi/4$.

9 Final Remarks

Hybrid piezoelectric nanogenerators, made of Zinc Oxyde nanorods, embedded into a polymeric matrix and growth on a flexible polymeric supports, are investigated. Due to the high density and nearly regular distribution of the nanorods, an equivalent periodic topology can be considered. The resulting device is made of a microstructured composite material, whose global response is strongly influenced by the microstructure, i.e. by the geometry and materials properties of each constituents and by their collaborative behaviour.

In such case, a very detailed description could be obtained via micromechanical approaches, resulting in often too cumbersome analyses. For this reason, multi-scale techniques can be alternatively used, being a very valuable tool to gather the overall behaviour. In this framework, a dynamic asymptotic homogenization approach, for periodic piezoelectric composites, is proposed. By exploiting this homogenization approach, a rigorous constitutive characterization of the periodic piezoelectric microstructured material is carried out, with the aim of optimizing their performances by analysing the behaviour of the material/device in the space of the physical-mechanical parameters. Among different parameters, focus is on the influence of both the height of the nanorods and of the density (defined as ratio between the volume occupied by the nanorods and the volume of the Periodic Cell), since during the synthesis process of the samples it is possible to directly modify those parameters. Under the assumption of considering an equivalent homogenized material at the macroscopic scale, also analytical solutions are found, providing benchmark comparative solutions. Almost perfect match is found by comparing the macroscopic analytic results with those obtained by the heterogeneous model via up-scaling relations, by confirming the optimal accuracy of the proposed homogenization scheme.

The behaviour of three piezoelectric microstructured nanogenerators, characterized by different working principles, is studied as a set of geometrical parameters changes. Both extension and bending nanogenerators are taken into account, considering either extension along the nanorods axis, or orthogonally to it. The influence of either the height of nanorods and their density on the overall behaviour of such devices is analysed. Concerning the microstructured extension nanogenerators, both cases of uniform surface load and load with fixed resultant have been investigated. In the first case, maximum values of the potential differences are observed for low values of the density, in the range 0.1-0.2. In the second case, instead, the maximum potential differences correspond to higher values of 0.4-0.5. As expected, the variation of the nanorods height determine a grossly linear variation of the potential difference in the considered nanogenerator. In all the analysed case, it is noted that devices with free lateral faces exhibit better performances in terms of potential difference, with respect to the corresponding ones with constrained faces. With reference to microstructured bending nanogenerators, it is noted that an improved response is achieved by adding a further top layer, of increasing thickness, on the initial composite material made of two equal layers sandwiching the periodically distributed nanorods, embedded into the polymeric matrix. Moreover, for a fixed thickness of the additional top layer, the best response in terms of potential difference is observed for the highest values of the nanorods density. As regards the microstructured transversal extension nanogenerators, it emerges that the response, in terms of potential difference, is not affected by the thickness of the additional top layer. Moreover, for a fixed thickness, again, the best response is observed for the highest values of the nanorods density.

With reference to the study in the dynamic regime, the free wave propagation in such a periodic material is analysed. Considering waves travelling along the nanorords axis, it turns out that as the material density decreases and the height of nanorods increases, more dense spectra are found. Moreover, various partial partial band gaps are detected for higher values of density, suggesting that lower values of the density enables better functioning as nanogenerators. As the nanorods height increases, a higher number of partial band gaps, characterized by lower frequencies, are observed. The acoustic and optical branches tend to be shifted towards lower angular frequencies. Finally, with reference to waves travelling in the plane normal to the nanorods axis, very dense spectra are here observed, where no partial band gaps, in the low frequency range, are detected irrespective of the considered density and height (few partial band gaps are found in the high frequency and characterized by small amplitudes). It is confirmed that the spectrum density increases as the density decreases and the height increases. The acoustic branches of the Floquet-Bloch spectrum, characterizing the heterogeneous material, are compared against the dispersion curves obtained adopting the first order homogenization theory. A good agreement is found, confirming the capability of the first order homogenization theory to satisfactorily reproducing the lowest (acoustic) branches of the Bloch spectrum for a wide range of wavelengths.

Acknowledgement

The authors thankfully acknowledge financial support by Regione Puglia under the Future in Research Program Development of next generation NEMS for energy harvesting-NSUX1F1, and National Group of Mathematical Physics (GNFM-INdAM). G. Z. gratefully acknowledges the support received from the The Ministry of Education, Universities and Research, through the PRIN 2015 funding scheme (project 2015JW9NJT Advanced mechanical modeling of new materials and structures for the solution of 2020 Horizon challenges)

References

Aboudi, J., Pindera, M., and Arnold, S. (2001). Linear thermoelastic higher-order theory for periodic multiphase materials. *Journal of Applied Mechanics*, 68(5):697–707.

Addessi, D., De Bellis, M. L., and Sacco, E. (2013). Micromechanical analysis of heterogeneous materials subjected to overall cosserat strains. *Mechanics Research Communications*, 54:27 – 34.

Addessi, D., De Bellis, M. L., and Sacco, E. (2016). A micromechanical approach for the cosserat modeling of composites. *Meccanica*, 51(3):569–592.

Ahmed, A., Saadatnia, Z., Hassan, I., Zi, Y., Xi, Y., He, X., Zu, J., and Wang, Z. L. (2017). Self-powered wireless sensor node enabled by a duck-shaped triboelectric nanogenerator for harvesting water wave energy. *Advanced Energy Materials*, 7(7):1601705.

Allaire, G. (1992). Homogenization and two-scale convergence. *SIAM Journal on Mathematical Analysis*, 23(6):1482–1518.

Almadhoun, M. N., Hedhili, M. N., Odeh, I. N., Xavier, P., Bhansali, U. S., and Alshareef, H. N. (2014). Influence of stacking morphology and edge nitrogen doping on the dielectric performance of graphene-polymer nanocomposites. *Chemistry of Materials*, 26(9):2856–2861.

Ameen, M., Peerlings, R., and Geers, M. (2018). A quantitative assessment of the scale separation limits of classical and higher-order asymptotic homogenization. *European Journal of Mechanics - A/Solids*, 71:89 – 100.

Andrianov, I. V., Bolshakov, V. I., Danishevs' kyy, V. V., and Weichert, D. (2008). Higher order asymptotic homogenization and wave propagation in periodic composite materials. In *Proceedings of the Royal Society of London A: Mathematical, Physical and Engineering Sciences*, volume 464, pages 1181–1201.

Askari, H., Hashemi, E., Khajepour, A., Khamesee, M. B., and Wang, Z. L. (2019). Tire condition monitoring and intelligent tires using nanogenerators based on piezoelectric, electromagnetic, and triboelectric effects. *Advanced Materials Technologies*, 4(1):1800105.

Bacca, M., Bigoni, D., Corso, F. D., and Veber, D. (2013a). Mindlin second-gradient elastic properties from dilute two-phase cauchy-elastic composites. part i: Closed form expression for the effective higher-order constitutive tensor. *International Journal of Solids and Structures*, 50(24):4010 – 4019.

Bacca, M., Bigoni, D., Corso, F. D., and Veber, D. (2013b). Mindlin second-gradient elastic properties from dilute two-phase cauchy-elastic composites part ii: Higher-order constitutive properties and application cases. *International Journal of Solids and Structures*, 50(24):4020 – 4029.

Bacigalupo, A. (2014). Second-order homogenization of periodic materials based on asymptotic approximation of the strain energy: formulation and validity limits. *Meccanica*, 49(6):1407–1425.

Bacigalupo, A. and Gambarotta, L. (2010). Second-order computational homogenization of heterogeneous materials with periodic microstructure. *ZAMM Journal of Applied Mathematics and Mechanics*, 90:796–811.

Bacigalupo, A. and Gambarotta, L. (2012). Computational two-scale homogenization of periodic masonry: Characteristic lengths and dispersive waves. *Computer Methods in Applied Mechanics and Engineering*, 213-216:16 – 28.

Bacigalupo, A. and Gambarotta, L. (2013). A multi-scale strain-localization analysis of a layered strip with debonding interfaces. *International Journal of Solids and Structures*, 50(13):2061 – 2077.

Bacigalupo, A. and Gambarotta, L. (2014). Second-gradient homogenized model for wave propagation in heterogeneous periodic media. *International Journal of Solids and Structures*, 51(5):1052–1065.

Bacigalupo, A., Morini, L., and Piccolroaz, A. (2016). Multiscale asymptotic homogenization analysis of thermo-diffusive composite materials. *International Journal of Solids and Structures*, 85-86:15–33.

Bacigalupo, A., Paggi, M., Dal Corso, F., and Bigoni, D. (2017). Identification of higher-order continua equivalent to a cauchy elastic composite. *Mechanics Research Communications*, doi.org/10.1016/j.mechrescom.2017.07.002.

Bakhvalov, N. and Panasenko, G. (1984). *Homogenization: Averaging Processes in Periodic Media*. Kluwer Academic Publishers, Dordrecht-Boston-London.

Bansal, M., Singh, I., Patil, R., Claus, S., and Bordas, S. (2019). A simple and robust computational homogenization approach for heterogeneous particulate composites. *Computer Methods in Applied Mechanics and Engineering*, 349:45 – 90.

Baraldi, D., Cecchi, A., and Tralli, A. (2015). Continuous and discrete models for masonry like material: A critical comparative study. *European Journal of Mechanics - A/Solids*, 50:39 – 58.

Berger, H., Kari, S., Gabbert, U., Rodrguez-Ramos, R., Bravo-Castillero, J., and Guinovart-Daz, R. (2005). A comprehensive numerical homogenisation technique for calculating effective coefficients of uniaxial piezoelectric fibre composites. *Materials Science and Engineering: A*, 412(1):53 – 60. International Conference on Recent Advances in Composite Materials.

Bigoni, D. and Drugan, W. J. (2007). Analytical derivation of Cosserat moduli via homogenization of heterogeneous elastic materials. *J Appl Mech*, 74:741–753.

Biswas, R. and Poh, L. H. (2017). A micromorphic computational homogenization framework for heterogeneous materials. *Journal of the Mechanics and Physics of Solids*, 102:187–208.

Biswas, R., Shedbale, A., and Poh, L. (2019). Nonlinear analyses with a micromorphic computational homogenization framework for composite materials. *Computer Methods in Applied Mechanics and Engineering*, 350:362 – 395.

Bloch, F. (1928). Uber die quantenmechanik der elektronen in kristallgittern. *Z. Phys.*, 52:555–600.

Boutin, C. (1996). Microstructural effects in elastic composites. *International Journal of Solids and Structures*, 33:1023–1051.

Brillouin, L. (1960). *Wave Propagation and Group Velocity*. New York: Academic Press.

Briscoe, J. and Dunn, S. (2015). Piezoelectric nanogenerators a review of nanostructured piezoelectric energy harvesters. *Nano Energy*, 14:15 – 29. Special issue on the 2nd International Conference on Nanogenerators and Piezotronics (NGPT 2014).

Cecchi, A. and Tralli, A. (2012). A homogenized viscoelastic model for masonry structures. *International Journal of Solids and Structures*, 49(13):1485 – 1496.

Chen, Y., Scarpa, F., Liu, Y., and Leng, J. (2013). Elasticity of anti-tetrachiral anisotropic lattices. *International Journal of Solids and Structures*, 50(6):996 – 1004.

Cherednichenko, K. D. and Evans, J. A. (2019). Homogenisation of thin periodic frameworks with high-contrast inclusions. *Journal of Mathematical Analysis and Applications*, 473(2):658 – 679.

Choi, M., Murillo, G., Hwang, S., Kim, J. W., Jung, J. H., Chen, C.-Y., and Lee, M. (2017). Mechanical and electrical characterization of pvdf-zno hybrid structure for application to nanogenerator. *Nano Energy*, 33:462 – 468.

De Bellis, M. L. and Addessi, D. (2011). A Cosserat based multi–scale model for masonry structures. *International Journal for Multiscale Computational Engineering*, 9(5):543–563.

De Bellis, M. L. and Bacigalupo, A. (2017). Auxetic behavior and acoustic properties of microstructured piezoelectric strain sensors. *Smart Materials and Structures*, 26(8):085037.

De Domenico, D. and Askes, H. (2016). A new multi-scale dispersive gradient elasticity model with micro-inertia: Formulation and -finite element implementation. *International Journal for Numerical Methods in Engineering*, 108(5):485–512.

Deraemaeker, A. and Nasser, H. (2010). Numerical evaluation of the equivalent properties of macro fiber composite (mfc) transducers using periodic homogenization. *International Journal of Solids and Structures*, 47(24):3272–3285.

Dirrenberger, J., Forest, S., and Jeulin, D. (2013). Effective elastic properties of auxetic microstructures: anisotropy and structural applications. *International Journal of Mechanics and Materials in Design*, 9(1):21–33.

Eftekhari, A. (2011). *Nanostructured conductive polymers*. John Wiley & Sons.

Fan, F. R., Tang, W., and Wang, Z. L. (2016). Flexible nanogenerators for energy harvesting and self-powered electronics. *Advanced Materials*, 28(22):4283–4305.

Fantoni, F., Bacigalupo, A., and Paggi, M. (2017). Multi-field asymptotic homogenization of thermo-piezoelectric materials with periodic microstructure. *International Journal of Solids and Structures*, 120:31–56.

Fantoni, F., Bacigalupo, A., and Paggi, M. (2018). Design of thermo-piezoelectric microstructured bending actuators via multi-field asymptotic homogenization. *International Journal of Mechanical Sciences*, 146-147:319 – 336.

Fish, J. and Chen, W. (2001). Higher-order homogenization of initial/boundary-value problem. *Journal of engineering mechanics*, 127(12):1223–1230.

Floquet, G. (1883). Sur les quations diffrentielles linaires coefficients priodiques. *Annales de l'cole Normale Suprieure*, 12:47–88.

Gałka, A., Telega, J. J., and Wojnar, R. (1996). Some computational aspects of homogenization of thermopiezoelectric composites. *Comp. Assisted Mech. Eng. Sci*, 3(2):133–154.

Gambin, B. and Kröner, E. (1989). Higher order terms in the homogenized stressstrain relation of periodic elastic media. physica status solidi (b). *International Journal of Engineering Science*, 151(2):513–519.

Huang, C. and Zhang, Q. (2004). Enhanced dielectric and electromechanical responses in high dielectric constant all-polymer percolative composites. *Advanced Functional Materials*, 14(5):501–506.

Hui, T. and Oskay, C. (2014). A high order homogenization model for transient dynamics of heterogeneous media including micro-inertia effects. *Computer Methods in Applied Mechanics and Engineering*, 273:181 – 203.

Hütter, G. (2017). Homogenization of a cauchy continuum towards a micromorphic continuum. *Journal of the Mechanics and Physics of Solids*, 99:394–408.

Jin, L., Chen, J., Zhang, B., Deng, W., Zhang, L., Zhang, H., Huang, X., Zhu, M., Yang, W., and Wang, Z. L. (2016). Self-powered safety helmet based on hybridized nanogenerator for emergency. *ACS nano*, 10(8):7874–7881.

Kamotski, I. V. and Smyshlyaev, V. P. (2019). Two-scale homogenization for a general class of high contrast pde systems with periodic coefficients. *Applicable Analysis*, 98(1-2):64–90.

Kanouté, P., Boso, D., Chaboche, J., and Schrefler, B. (2009). Multiscale methods for composites: a review. *Archives of Computational Methods in Engineering*, 16(1):31–75.

Kouznetsova, V., Geers, M., and Brekelmans, W. (2004). Multi-scale second-order computational homogenization of multi-phase materials: a nested finite element solution strategy. *Computer Methods in Applied Mechanics and Engineering*, 193(48):5525–5550.

Lesičar, T., Tonković, Z., and Sorić, J. (2014). A second-order two-scale homogenization procedure using c-1 macrolevel discretization. *Computational mechanics*, 54(2):425–441.

Li, J., Zhu, Z., Fang, L., Guo, S., Erturun, U., Zhu, Z., West, J. E., Ghosh, S., and Kang, S. H. (2017a). Analytical, numerical, and experimental studies of viscoelastic effects on the performance of soft piezoelectric nanocomposites. *Nanoscale*, 9:14215–14228.

Li, M., Porter, A. L., and Wang, Z. L. (2017b). Evolutionary trend analysis of nanogenerator research based on a novel perspective of phased bibliographic coupling. *Nano Energy*, 34:93 – 102.

Li, X., Zhang, J., and Zhang, X. (2011). Micro-macro homogenization of gradient-enhanced cosserat media. *European Journal of Mechanics-A/Solids*, 30(3):362–372.

Liu, R., Kuang, X., Deng, J., Wang, Y.-C., Wang, A. C., Ding, W., Lai, Y.-C., Chen, J., Wang, P., Lin, Z., et al. (2018). Shape memory polymers for body motion energy harvesting and self-powered mechanosensing. *Advanced Materials*, 30(8):1705195.

McCarthy, J., Watkins, S., Deivasigamani, A., and John, S. (2016). Fluttering energy harvesters in the wind: A review. *Journal of Sound and Vibration*, 361:355 – 377.

Mindlin, R. (1974). Equations of high frequency vibrations of thermopiezoelectric crystal plates. *International Journal of Solids and Structures*, 10(6):625–637.

Mühlich, U., Zybell, L., and Kuna, M. (2012). Estimation of material properties for linear elastic strain gradient effective media. *European Journal of Mechanics-A/Solids*, 31(1):117–130.

Opoku, C., Dahiya, A. S., Oshman, C., Cayrel, F., Poulin-Vittrant, G., Alquier, D., and Camara, N. (2015). Fabrication of zno nanowire based piezoelectric generators and related structures. *Physics Procedia*, 70:858 – 862. Proceedings of the 2015 ICU International Congress on Ultrasonics, Metz, France.

Peerlings, R. and Fleck, N. (2004). Computational evaluation of strain gradient elasticity constants. *International Journal for Multiscale Computational Engineering*, 2(4).

Pettermann, H. E. and Suresh, S. (2000). A comprehensive unit cell model: a study of coupled effects in piezoelectric 13 composites. *International Journal of Solids and Structures*, 37(39):5447 – 5464.

Reccia, E., De Bellis, M., Trovalusci, P., and Masiani, R. (2018). Sensitivity to material contrast in homogenization of random particle composites as micropolar continua. *Composites Part B: Engineering*, 136:39 – 45.

Saadatnia, Z., Asadi, E., Askari, H., Zu, J., and Esmailzadeh, E. (2017). Modeling and performance analysis of duck-shaped triboelectric and electromagnetic generators for water wave energy harvesting. *International Journal of Energy Research*, 41(14):2392–2404.

Salvadori, A., Bosco, E., and Grazioli, D. (2014). A computational homogenization approach for li-ion battery cells: Part 1 formulation. *Journal of the Mechanics and Physics of Solids*, 65:114 – 137.

Scarpa, F., Adhikari, S., Gil, A. J., and Remillat, C. (2010). The bending of single layer graphene sheets: the lattice versus continuum approach. *Nanotechnology*, 21(12):125702.

Scarpa, F., Adhikari, S., and Phani, A. S. (2009). Effective elastic mechanical properties of single layer graphene sheets. *Nanotechnology*, 20(6):065709.

Sepe, V., Auricchio, F., Marfia, S., and Sacco, E. (2016). Homogenization techniques for the analysis of porous sma. *Computational Mechanics*, 57(5):755–772.

Smyshlyaev, V. and Cherednichenko, K. (2000). On rigorous derivation of strain gradient effects in the overall behaviour of periodic heterogeneous media. *Journal of the Mechanics and Physics of Solids*, 48(6):1325–1357.

Stassi, S., Cauda, V., Ottone, C., Chiodoni, A., Pirri, C. F., and Canavese, G. (2015). Flexible piezoelectric energy nanogenerator based on zno nanotubes hosted in a polycarbonate membrane. *Nano Energy*, 13:474 – 481.

Tan, S. H. and Poh, L. H. (2018). Homogenized gradient elasticity model for plane wave propagation in bilaminate composites. *Journal of Engineering Mechanics*, 144(9):04018075.

Trovalusci, P., Bellis, M. L. D., and Masiani, R. (2017). A multiscale description of particle composites: From lattice microstructures to micropolar continua. *Composites Part B: Engineering*, 128:164 – 173.

Trovalusci, P., Ostoja-Starzewski, M., Bellis, M. L. D., and Murrali, A. (2015). Scale-dependent homogenization of random composites as micropolar continua. *European Journal of Mechanics - A/Solids*, 49:396 – 407.

Wang, D., Wu, X., Wang, Z., and Chen, L. (2005). Cracking causing cyclic instability of lifepo4 cathode material. *Journal of Power Sources*, 140(1):125–128.

Wang, D., You, F., and Hu, G.-H. (2015). Graphene/polymer nanocomposites with high dielectric performance: Interface engineering. In *Graphene-Based Polymer Nanocomposites in Electronics*, pages 49–65. Springer.

Wang, J., Kulkarni, A., Ke, F., Bai, Y., and Zhou, M. (2008). Novel mechanical behavior of zno nanorods. *Computer Methods in Applied Mechanics and Engineering*, 197(41):3182 – 3189. Recent Advances in Computational Study of Nanostructures.

Wang, Z. L. (2004). Zinc oxide nanostructures: growth, properties and applications. *Journal of Physics: Condensed Matter*, 16(25):R829–R858.

Wang, Z. L., Jiang, T., and Xu, L. (2017a). Toward the blue energy dream by triboelectric nanogenerator networks. *Nano Energy*, 39:9–23.

Wang, Z. L. and Song, J. (2006). Piezoelectric nanogenerators based on zinc oxide nanowire arrays. *Science*, 312(5771):242–246.

Wang, Z.-P., Poh, L. H., Dirrenberger, J., Zhu, Y., and Forest, S. (2017b). Isogeometric shape optimization of smoothed petal auxetic structures via computational periodic homogenization. *Computer Methods in Applied Mechanics and Engineering*, 323:250 – 271.

Yang, D., Qiu, Y., Jiang, Q., Guo, Z., Song, W., Xu, J., Zong, Y., Feng, Q., and Sun, X. (2017). Patterned growth of zno nanowires on flexible substrates for enhanced performance of flexible piezoelectric nanogenerators. *Applied Physics Letters*, 110(6):063901.

Yang, J. (2004). *An introduction to the theory of piezoelectricity*, volume 9. Springer Science & Business Media.

Yi, G.-C., Wang, C., and Park, W. I. (2005). Zno nanorods: synthesis, characterization and applications. *Semiconductor Science and Technology*, 20(4):S22.

Zah, D. and Miehe, C. (2013). Computational homogenization in dissipative electro-mechanics of functional materials. *Computer Methods in Applied Mechanics and Engineering*, 267:487 – 510.

Zhang, H., Zhang, S., Bi, J., and Schrefler, B. (2007). Thermomechanical analysis of periodic multiphase materials by a multiscale asymptotic homogenization approach. *International Journal for Numerical Methods in Engineering*, 69(1):87–113.

Zhang, N., Chen, J., Huang, Y., Guo, W., Yang, J., Du, J., Fan, X., and Tao, C. (2016). A wearable all-solid photovoltaic textile. *Advanced Materials*, 28(2):263–269.

Zhang, X., OBrien, D. J., and Ghosh, S. (2019). Parametrically homogenized continuum damage mechanics (phcdm) models for composites from micromechanical analysis. *Computer Methods in Applied Mechanics and Engineering*, 346:456 – 485.

Appendix A: Solutions of the hierarchical differential problems

The following hierarchical differential problems, expressed in terms of the sensitivities $u_k^{(j)}$, $\phi^{(j)}$ of both microscopic displacement u_k and potential ϕ fields, can be obtained from the asymptotic expansion of the field equations (6) by collecting the terms at the same order of ε.
More specifically, the recursive problem the at the order ε^{-2} reads

$$\begin{aligned} &\left(C^m_{ijkl} u^{(0)}_{k,l}\right)_{,j} + \left(e^m_{ijk} \phi^{(0)}_{,k}\right)_{,j} = f_i^{(0)}(\mathbf{x}, t), \\ &\left(e^m_{kli} u^{(0)}_{k,l}\right)_{,i} - \left(\beta^m_{il} \phi^{(0)}_{,l}\right)_{,i} = g^{(0)}(\mathbf{x}, t). \end{aligned} \tag{43}$$

The solvability condition in the class of the Q-periodic functions implies that both source terms vanish, i.e. $f_i^{(0)}(\mathbf{x}, t) = 0$ and $g^{(0)}(\mathbf{x}, t) = 0$. It follows that the solution of the differential problem is independent on the fast variable $\boldsymbol{\xi}$ and it takes the form reported in (7).
Analogously, by exploiting the solution of the differential problem (43), the recursive problem the at the order ε^{-1} is

$$\begin{aligned} &\left(C^m_{ijkl} u^{(1)}_{k,l}\right)_{,j} + C^m_{ijkl,j} \frac{\partial U_k}{\partial x_l} + \left(e^m_{ijk} \phi^{(1)}_{,k}\right)_{,j} + e^m_{ijk,j} \frac{\partial \varPhi}{\partial x_k} = f_i^{(1)}(\mathbf{x}, t), \\ &\left(e^m_{kli} u^{(1)}_{k,l}\right)_{,i} + e^m_{kli,i} \frac{\partial U_k}{\partial x_l} - \left(\beta^m_{il} \phi^{(1)}_{,l}\right)_{,i} - \beta^m_{il,i} \frac{\partial \varPhi}{\partial x_l} = g^{(1)}(\mathbf{x}, t). \end{aligned} \tag{44}$$

Here, the solvability condition in the class of the Q-periodic functions implies that

$$\begin{aligned} &f_i^{(1)}(\mathbf{x}, t) = \langle C^m_{ijkl,j} \rangle \frac{\partial U_k}{\partial x_l} + \langle e^m_{ijk,j} \rangle \frac{\partial \varPhi}{\partial x_k} = 0, \\ &g^{(1)}(\mathbf{x}, t) = \langle e^m_{kli,i} \rangle \frac{\partial U_k}{\partial x_k} - \langle \beta^m_{il,i} \rangle \frac{\partial \varPhi}{\partial x_l} = 0, \end{aligned} \tag{45}$$

since the components of the constitutive tensors at the microscopic scale are Q-periodic. In this case, the solution of the differential problem takes the form reported in (8).
Similarly, the recursive problem the at the order ε^0 is obtained by exploiting the solution of both the differential problems (43) and (44), and it reads

$$\begin{aligned} &\left(C^m_{ijkl} u^{(2)}_{k,l}\right)_{,j} + \left[\left(C^m_{ijkq_2} N^{(1)}_{kpq_1}\right)_{,j} + C^m_{iq_1pq_2} + C^m_{iq_2kl} N^{(1)}_{kpq_1,l} + \left(e^m_{ijq_2} \widetilde{W}^{(1)}_{pq_1}\right)_{,j} + e^m_{iq_2k} \widetilde{W}^{(1)}_{pq_1,k}\right] \frac{\partial^2 U_p}{\partial x_{q_1} \partial x_{q_2}} + \\ &+ \left(e^m_{ijk} \phi^{(2)}_{,k}\right)_{,j} + \left[\left(C^m_{ijkq_2} \widetilde{N}^{(1)}_{kq_1}\right)_{,j} + C^m_{iq_2kl} \widetilde{N}^{(1)}_{kq_1,l} + \left(e^m_{ijq_2} W^{(1)}_{q_1}\right)_{,j} + e^m_{iq_1q_2} + e^m_{iq_2k} W^{(1)}_{q_1,k}\right] \frac{\partial^2 \varPhi}{\partial x_{q_1} \partial x_{q_2}} + \\ &- \rho^m \ddot{U}_i = f_i^{(2)}(\mathbf{x}, t), \end{aligned} \tag{46}$$

$$\left(e^m_{kli}u^{(2)}_{k,l}\right)_{,i}+\left[\left(e^m_{kq_2i}N^{(1)}_{kpq_1}\right)_{,i}+e^m_{klq_2}N^{(1)}_{kpq_1,l}+e^m_{pq_2q_1}-\left(\beta^m_{iq_2}\widetilde{W}^{(1)}_{pq_1}\right)_{,i}-\beta^m_{q_2l}\widetilde{W}^{(1)}_{pq_1,l}\right]\frac{\partial^2 U_p}{\partial x_{q_1}\partial x_{q_2}}+$$
$$-\left(\beta^m_{il}\phi^{(2)}_{,l}\right)_{,i}+\left[\left(e^m_{kq_2i}\widetilde{N}^{(1)}_{kq_1}\right)_{,i}+e^m_{klq_2}\widetilde{N}^{(1)}_{kq_1,l}-\left(\beta^m_{iq_2}W^{(1)}_{q_1}\right)_{,i}-\beta^m_{q_1q_2}-\beta^m_{q_2l}W^{(1)}_{q_1,l}\right]\frac{\partial^2 \varPhi}{\partial x_{q_1}\partial x_{q_2}}=$$
$$=g^{(2)}(\mathbf{x},t).$$

Finally, the solvability condition in the class of the Q-periodic functions implies that

$$\begin{aligned}
f^{(2)}_i(\mathbf{x},t)&=\langle C^m_{iq_1pq_2}+C^m_{iq_2kl}N^{(1)}_{kpq_1,l}+e^m_{iq_2k}\widetilde{W}^{(1)}_{,k}\rangle\frac{\partial^2 U_p}{\partial x_{q_1}\partial x_{q_2}}+\\
&+\langle C^m_{iq_2kl}\widetilde{N}^{(1)}_{kq_1,l}+e^m_{iq_1q_2}+e^m_{iq_2k}W^{(1)}_{q_1,k}\rangle\frac{\partial^2 \varPhi}{\partial x_{q_1}\partial x_{q_2}}-\langle\rho^m\rangle\ddot{U}_i,\\
g^{(2)}(\mathbf{x},t)&=\langle e^m_{klq_2}N^{(1)}_{kpq_1,l}+e^m_{pq_2q_1}-\beta_{q_2l}\widetilde{W}^{(1)}_{pq_1,l}\rangle\frac{\partial^2 U_p}{\partial x_{q_1}\partial x_{q_2}}+\\
&+\langle e^m_{klq_2q}\widetilde{N}^{(1)}_{kq_1,l}-\beta^m_{q_1q_2}-\beta^m_{q_2l}W^{(1)}_{q_1,l}\rangle\frac{\partial^2 \varPhi}{\partial x_{q_1}\partial x_{q_2}},
\end{aligned}\qquad(47)$$

The solution of the differential problem takes the form reported in (9).

Appendix B: Average field equation of infinite order

By plugging the down-scaling relations (15) in the field equations (1), i.e. by reassembling the recursive differential problems at different ε orders (43), (44) and (46), the following average field equation of infinite order are obtained as

$$\begin{aligned}
&n^{(2,0)}_{ipq_1q_2}\frac{\partial^2 U_p}{\partial x_{q_1}\partial x_{q_2}}+\widetilde{n}^{(2,0)}_{iq_1q_2}\frac{\partial^2 \varPhi}{\partial x_{q_1}\partial x_{q_2}}-n^{(2,0)}_{ip}\ddot{U}_p+\mathcal{O}\left(\varepsilon\right)+b_i=0,\\
&\widetilde{w}^{(2,0)}_{pq_1q_2}\frac{\partial^2 U_p}{\partial x_{q_1}\partial x_{q_2}}-w^{(2,0)}_{q_1q_2}\frac{\partial^2 \varPhi}{\partial x_{q_1}\partial x_{q_2}}+\mathcal{O}\left(\varepsilon\right)-\rho_e=0,
\end{aligned}\qquad(48)$$

where the components of the constant global constitutive tensors, involved in the governing equations, take the form

$$\begin{aligned}
n^{(2,0)}_{ipq_1q_2}&=\frac{1}{2}\left\langle C^m_{iq_1pq_2}+C^m_{iq_2kl}N^{(1)}_{kpq_1,l}+e^m_{iq_2k}\widetilde{W}^{(1)}_{,k}+C^m_{iq_2pq_1}+C^m_{iq_1kl}N^{(1)}_{kpq_2,l}+e^m_{iq_1k}\widetilde{W}^{(1)}_{,k}\right\rangle,\\
\widetilde{n}^{(2,0)}_{iq_1q_2}&=\frac{1}{2}\left\langle C^m_{iq_2kl}\widetilde{N}^{(1)}_{kq_1,l}+e^m_{iq_1q_2}+e^m_{iq_2k}W^{(1)}_{q_1,k}+C^m_{iq_1kl}\widetilde{N}^{(1)}_{kq_2,l}+e^m_{iq_2q_1}+e^m_{iq_1k}W^{(1)}_{q_2,k}\right\rangle,\\
n^{(2,0)}_{ip}&=\left\langle\rho^m\right\rangle\delta_{ip},\\
\widetilde{w}^{(2,0)}_{pq_1q_2}&=\frac{1}{2}\left\langle e^m_{klq_2}N^{(1)}_{kpq_1,l}+e^m_{pq_2q_1}-\beta_{q_2l}\widetilde{W}^{(1)}_{pq_1,l}+e^m_{klq_1}N^{(1)}_{kpq_2,l}+e^m_{pq_1q_2}-\beta_{q_1l}\widetilde{W}^{(1)}_{pq_2,l}\right\rangle,\\
w^{(2,0)}_{q_1q_2}&=\frac{1}{2}\left\langle\beta^m_{q_1q_2}+\beta^m_{q_2l}W^{(1)}_{q_1,l}-e^m_{klq_2q}\widetilde{N}^{(1)}_{kq_1,l}+\beta^m_{q_2q_1}+\beta^m_{q_1l}W^{(1)}_{q_2,l}-e^m_{klq_1q}\widetilde{N}^{(1)}_{kq_2,l}\right\rangle.
\end{aligned}\qquad(49)$$

In order to obtain a formal solution of equations (48), the macroscopic variables U_k and $\mathit{\Phi}$ are asymptotically expanded as follows

$$\begin{aligned} U_k\left(\mathbf{x},t\right) &= \sum_{j=0}^{+\infty} \varepsilon^j U_k^{(j)}\left(\mathbf{x},t\right), \\ \mathit{\Phi}\left(\mathbf{x},t\right) &= \sum_{j=0}^{+\infty} \varepsilon^j \mathit{\Phi}^{(j)}\left(\mathbf{x},t\right). \end{aligned} \tag{50}$$

By plugging (50) into the (48), the asymptotic expansion of the average field equation of infinite order takes the form

$$\begin{aligned} & n_{ipq_1q_2}^{(2,0)}\left(\frac{\partial^2 U_p^{(0)}}{\partial x_{q_1}\partial x_{q_2}} + \varepsilon \frac{\partial^2 U_p^{(1)}}{\partial x_{q_1}\partial x_{q_2}} + \varepsilon^2 \frac{\partial^2 U_p^{(2)}}{\partial x_{q_1}\partial x_{q_2}} + \ldots\right) + \widetilde{n}_{iq_1q_2}^{(2,0)}\left(\frac{\partial^2 \mathit{\Phi}^{(0)}}{\partial x_{q_1}\partial x_{q_2}} + \varepsilon \frac{\partial^2 \mathit{\Phi}^{(1)}}{\partial x_{q_1}\partial x_{q_2}} + \right. \\ & \left. +\varepsilon^2 \frac{\partial^2 \mathit{\Phi}^{(2)}}{\partial x_{q_1}\partial x_{q_2}} + \ldots\right) - n_{ip}^{(2,0)}\left(\ddot{U}_p^{(0)} + \varepsilon \ddot{U}_p^{(1)} + \varepsilon^2 \ddot{U}_p^{(2)}\right) + \ldots + b_i = 0, \\ & \widetilde{w}_{pq_1q_2}^{(2,0)}\left(\frac{\partial^2 U_p^{(0)}}{\partial x_{q_1}\partial x_{q_2}} + \varepsilon \frac{\partial^2 U_p^{(1)}}{\partial x_{q_1}\partial x_{q_2}} + \varepsilon^2 \frac{\partial^2 U_p^{(2)}}{\partial x_{q_1}\partial x_{q_2}} + \ldots\right) - w_{q_1q_2}^{(2,0)}\left(\frac{\partial^2 \mathit{\Phi}^{(0)}}{\partial x_{q_1}\partial x_{q_2}} + \varepsilon \frac{\partial^2 \mathit{\Phi}^{(1)}}{\partial x_{q_1}\partial x_{q_2}} + \right. \\ & \left. +\varepsilon^2 \frac{\partial^2 \mathit{\Phi}^{(2)}}{\partial x_{q_1}\partial x_{q_2}} + \ldots\right) + \ldots - \rho_e = 0. \end{aligned} \tag{51}$$

In particular, by collecting the terms in (51) at the same order of ε, an infinite set of macroscopic hierarchical differential problems, expressed in terms of the sensitivities $U_p^{(j)}$, $\mathit{\Phi}^{(j)}$ of both macroscopic displacement U_p and potential $\mathit{\Phi}$ fields can be determined. Namely, the recursive problem at the macroscopic scale of order ε^0 reads

$$\begin{aligned} & n_{ipq_1q_2}^{(2,0)} \frac{\partial^2 U_p^{(0)}}{\partial x_{q_1}\partial x_{q_2}} + \widetilde{n}_{iq_1q_2}^{(2,0)} \frac{\partial^2 \mathit{\Phi}^{(0)}}{\partial x_{q_1}\partial x_{q_2}} - n_{ip}^{(2,0)} \ddot{U}_p^{(0)} + b_i = 0, \\ & \widetilde{w}_{pq_1q_2}^{(2,0)} \frac{\partial^2 U_p^{(0)}}{\partial x_{q_1}\partial x_{q_2}} - w_{q_1q_2}^{(2,0)} \frac{\partial^2 \mathit{\Phi}^{(0)}}{\partial x_{q_1}\partial x_{q_2}} - \rho_e = 0, \end{aligned} \tag{52}$$

while the generic recursive problem at the macroscopic scale of order ε^m with $m \in \mathbb{Z}$, $m \geq 1$, is found as

$$\begin{aligned} & n_{ipq_1q_2}^{(2,0)} \frac{\partial^2 U_p^{(m)}}{\partial x_{q_1}\partial x_{q_2}} + \widetilde{n}_{iq_1q_2}^{(2,0)} \frac{\partial^2 \mathit{\Phi}^{(m)}}{\partial x_{q_1}\partial x_{q_2}} - n_{ip}^{(2,0)} \ddot{U}_p^{(m)} + s_i^{(m)}(\mathbf{x},t) = 0, \\ & \widetilde{w}_{pq_1q_2}^{(2,0)} \frac{\partial^2 U_p^{(m)}}{\partial x_{q_1}\partial x_{q_2}} - w_{q_1q_2}^{(2,0)} \frac{\partial^2 \mathit{\Phi}^{(m)}}{\partial x_{q_1}\partial x_{q_2}} - v^{(m)}(\mathbf{x},t) = 0, \end{aligned} \tag{53}$$

where $s_i^{(m)}$ and $v^{(m)}$ are known $\mathfrak{L}$-periodic fields, playing the role of source terms. Such fields depend both on higher order constant tensors, that appear in the terms at orders equal or higher than ε^m of the average field equation of infinite order (48), and on sensitivities $U_k^{(j)}$ and $\Phi^{(j)}$ descending from macroscopic hierarchical differential problems of order lower than ε^m.

Due to the $\mathfrak{L}$-periodicity of the source terms, the solution of equations (52) and (53) are in turn $\mathfrak{L}$-periodic. More specifically, the uniqueness of such solution is guaranteed by the fulfilment of the following normalization conditions $1/|\mathfrak{L}| \int_{\mathfrak{L}} U_p^{(m)} d\mathbf{x} = 0$ and $1/|\mathfrak{L}| \int_{\mathfrak{L}} \Phi^{(m)} d\mathbf{x} = 0$, where $|\mathfrak{L}| = \eta L^3$.

It is worth noting that the formal structure of equation (53) is the same as the one of (52), i.e. the governing equation of a first order piezoelectric continuum (Mindlin, 1974). Nevertheless, while the source terms in (52) are body forces and free charge densities acting on the heterogeneous medium, the terms in (53) are auxiliary source terms that take into account nonlocal effects occurring in equation (48), that asymptotically approximate the governing equations of the heterogeneous piezoelectric material, i.e. equation (1).